Computational dynamics of geometrically nonlinear structures coupled with acoustic fluids in presence of sloshing and capillarity : uncertainty quantification

Quentin Akkaoui

Université Paris-Est Marne-la-Vallée
École doctorale Sciences, Ingénierie et Environnement

THÈSE

présentée et soutenue publiquement le 4 octobre 2019

pour l'obtention du

Doctorat de l'Université Paris-Est Marne-la-Vallée

Discipline: mécanique

par

Quentin Akkaoui

Computational dynamics of geometrically nonlinear structures coupled with acoustic fluids in presence of sloshing and capillarity. Uncertainty quantification.

Composition du jury

Président :	Geert Degrande	Professor – KU Leuven University
Rapporteurs :	Maarten Arnst	Professor – Université de Liège
	Fabrice Thouverez	Professor – Ecole Centrale Lyon
Examinateur :	Yann Doutreleau	Direction Générale de l'Armement
Directeur de thèse :	Christian Soize	Professor – Université Paris-Est Marne-la-vallée
Encadrants :	Évangéline Capiez-Lernout	Assistant Professor – Université Paris-Est Marne-la-vallée
	Roger Ohayon	Professor – CNAM Paris

Laboratoire de Modélisation et Simulation Multi-Echelle — UMR 8208 CNRS

Mis en page avec la classe thesul.

Acknowledgements

Je souhaite tout d'abord remercier mon directeur de thèse, le professeur Christian Soize, pour son encadrement et son investissement pendant ces trois années de thèse. Sa rigueur et sa pédagogie ont été une source de motivation. Je remercie également mon encadrante Evangéline Capiez-Lernout, pour le temps qu'elle a consacré à m'aider dans mes travaux. Mes remerciements vont aussi au professeur Roger Ohayon pour ses conseils et le partage de son expérience. Je remercie ensuite la DGA (Direction Générale de l'Armement) pour sa participation au financement de mes travaux de thèse.

Je tiens ensuite à remercier les professeurs Fabrice Thouverez et Maarten Arnst pour avoir accepté de rapporter sur mon manuscrit de thèse. Merci également à monsieur Yann Doutreleau et au professeur Geert Degrande d'avoir accepté d'examiner mon travail.

Je remercie tout particulièrement mes amis et collègues du laboratoire MSME, pour ce temps passé dans le bureau 118. Nos discussions, nos partages et nos rigolades (et nos raclettes) ont permis de travailler dans une ambiance agréable et constructive. Merci à Antho, pour avoir refait le monde avec moi dans le calme comme dans la tempête. Merci à Picou, pour ses anecdotes et ses « ha..ha ». Merci à Justin « MPSA », pour son investissement dans YGO. Merci à Vincent, de ne « pas changer assiettes pour fromage ». Merci enfin à mon ket Brian, pour sa gentillesse, ses conseils, nos P30 (passés et à venir) et pour notre rêve de « cool company ».

Mes remerciements vont ensuite évidemment à ma famille, à mes frères et sœurs Paul, Julie, Léonard, à mes grands-parents Fernand, Colette, Nagi et Juliette, et enfin, tout particulièrement, à mes parents, pour leur soutien et leur présence. Merci également à Micha pour m'avoir communiqué l'envie de faire une thèse et m'avoir éveillé au monde de la recherche. Merci ensuite à tous ceux qui, de près ou de loin, m'ont apporté leur soutien durant ces trois ans, Emilie, Canny, Funny, et bien d'autres.

Je tiens d'abord à dédier ce travail à mes parents qui m'ont offert la possibilité de travailler dans les meilleures conditions.

Enfin, je dédie en particulier ce travail, le temps investi et tout ce que j'ai appris pendant ces dernières années à ma compagne Bonnie. Elle a cru en moi, m'a aidé, m'a fait rire et a façonné l'homme que je suis aujourd'hui. Merci à toi pour ta patience, pour ton soutien et pour ton amour.

Résumé

Dans cette thèse, on s'intéresse à la modélisation et à la simulation numérique de systèmes couplés fluide-structure, constitués d'une structure élastique partiellement remplie d'un liquide avec une surface libre, tenant compte des effets de ballottement et de capillarité. Le fluide interne est considéré comme linéaire, acoustique, dissipatif et la structure, à comportement élastique linéaire, est soumise à de grands déplacements induisant des non-linéarités géométriques. Le travail présenté dans ce manuscrit s'intéresse tout d'abord à l'étude théorique de ce type de système couplé fluide-structure et s'attache à la construction et à l'implémentation du modèle numérique en utilisant un modèle réduit non linéaire adapté. Ce modèle réduit permet d'effectuer les calculs dynamiques non linéaires et permet également de mieux comprendre les phénomènes liés à chaque partie du système couplé. Plusieurs applications numériques sont ensuite développées permettant l'analyse de divers phénomènes liés aux différents couplages et transferts d'énergie dans le système. Le premier axe de développement consiste en la quantification et en la réduction du temps de calcul nécessaire à la construction de la base de projection du modèle réduit pour des modèles numériques de systèmes couplés fluide-structure de très grande dimension. Une nouvelle méthodologie est présentée permettant de réduire les coûts numériques induits par la résolution de trois problèmes généralisés aux valeurs propres ne pouvant être résolus sur les ordinateurs de puissance intermédiaire. Un second axe de développement concerne la quantification de l'influence de l'opérateur de couplage entre la structure et la surface libre du liquide interne permettant de prendre en compte la condition d'angle de contact capillaire au niveau de la ligne triple tout en considérant une structure déformable. Le troisième axe est basé sur des travaux expérimentaux publiés en 1962, dans le cadre de développements de la NASA pour les lanceurs, qui ont mis en évidence un phénomène inattendu de ballottement de grande amplitude en basses-fréquences pour le liquide interne lors de l'excitation moyenne-fréquence du réservoir. On propose de revisiter et d'expliquer les causes de ce phénomène inattendu au travers d'une simulation numérique prenant en compte les non-linéarités géométriques de la structure. Enfin, un dernier axe de développement est consacré à la propagation des incertitudes non paramétriques de la structure dans le système par les différents mécanismes de couplages. La modélisation stochastique non paramétrique est celle de l'approche probabiliste non paramétrique qui utilise la théorie des matrices aléatoires. Une méthodologie permettant l'identification de l'hyperparamètre est présentée, basée sur un ensemble de données expérimentales et sur la résolution d'un problème statistique inverse. Une validation numérique de cette méthode sur un ensemble de données expérimentales simulées est présentée.

Abstract

In this thesis, we are interested in computationally modeling and simulating coupled fluid-structure systems constituted of an elastic structure partially filled with a fluid with a free surface, considering the effects of sloshing and capillarity. The internal fluid is linear, acoustic, dissipative, and the linear elastic structure is submitted to large displacements inducing geometrical nonlinearities. The work presented in this manuscript first details the theoretical study regarding such coupled fluid-structure systems and focuses on the construction and implementation of the computational model using an adapted nonlinear reduced-order model. This reduced-order model allows for performing the nonlinear dynamical simulations and for better understanding the phenomena related to each subset of the coupled system. Several numerical applications are then presented to analyze various phenomena related to the different coupling mechanisms and energy transfers in such fluid-structure system. The first development axis consists in quantifying and reducing the computational resources required for the construction of the projection basis of the reduced-order model when dealing with very-large dimension fluid-structure computational models. A new methodology is presented, which allows for reducing the computational costs required for solving three generalized eigenvalue problems that cannot be solved on medium-power computers. A second development axis is devoted to the quantification of the influence of the coupling operator between the structure and the free surface of the internal liquid allowing for taking into account the capillary contact angle condition on the triple line while considering a deformable structure. The third axis is based on experimental research published in 1962 in the framework of NASA researches for orbital launchers, which highlighted an unexpected phenomenon of large amplitude and low-frequency sloshing of an internal liquid for a medium-frequency excitation of the tank. We propose to revisit these experimental results and to explain the causes of such unexpected phenomenon through a numerical simulation taking into account the geometrical nonlinearities of the structure. Finally, the last development axis is devoted to the propagation of nonparametric uncertainties of the structure in the system by the different coupling mechanisms. The nonparametric stochastic model is the nonparametric probabilistic approach using the random matrix theory. A methodology for identifying the hyperparameter is presented, based on an experimental data set and on an inverse statistical problem. A numerical validation of this method on a simulated experimental data set is presented.

Contents

Chapter 1

Introduction

Contents

1.1 General introduction

From the analysis of microfluidic systems, through the study of a glass of water, to new space propulsion technologies, coupled fluid-structure systems have always been of great interest for all sectors of scientific research. The aeronautics, aerospace, naval, medical, and renewable energy industries are, for example, major actors of the scientific advances in fluid-structure interactions. Two main types of problems are generally studied: the first type focuses on the study of a fluid flow in contact with a structure (see Figure 1.2 left) and the second type focuses on the dynamics of a fluid and a structure around an initial static configuration without fluid flow (see Figure 1.2 right). The first type of problem can be encountered, for example, in the naval industry, considering the problems of hydroelasticity, as well as in the medical domain with the study of hemodynamic flow. The second type of problem can be encountered in many applications such as, for example, the vibration of kerosene tanks in military/civil aircrafts, the analysis of seismic vibrations of complex constructions such as dams or nuclear power plants, or the dynamics of liquids in oil tankers. In this work, we will focus on the second type of problem by analyzing the dynamics of structures partially filled with a liquid around a stable equilibrium configuration without fluid flow. In this type of problem, various phenomena can be encountered but the most frequent and most analyzed are mainly: sloshing, which describes the wave motion of the free surface of a liquid contained in a structure, directly related to the influence of gravity, and resulting from an energy transfer between the kinetic energy of the liquid and its potential gravity energy; capillarity, due to surface tension forces, which significantly influences the sloshing of the liquid free-surface with respect to the scale of the considered system and inversely proportional to the intensity of the gravity; hydroelasticity, which concerns the vibrations of a structure coupled to those of an incompressible internal/external fluid; vibroacoustic, which concerns the vibrations of a structure containing a compressible fluid and possibly immersed in an unbounded compressible fluid.

The complexity of coupled fluid-structure models that consider these types of phenomena is partly based on the significant difference between the frequency ranges at which these phenomena occur. The free surface sloshing of a liquid generally occurs at frequencies that are much lower that the frequencies of interest for the other phenomena (usually an order of magnitude 10 to 1 000 times higher). These sloshing frequencies can vary according to the intensity of the surface tension effects (capillarity). The elastic potential energy of the structure is therefore added to the gravity potential energy of the fluid. However, as the frequency increases, the free surface sloshing motion has smaller wavelength and smaller amplitude: the free surface deformation energy related to gravity becomes negligible compared to the other energies involved. Finally, vibroacoustic phenomena are due to the compressibility of the liquid and can appear in any part of the frequency band, depending on the cavity dimensions. It is thus essential to consider the different frequency domains when studying complex fluid-structure systems that take into account these various phenomena.

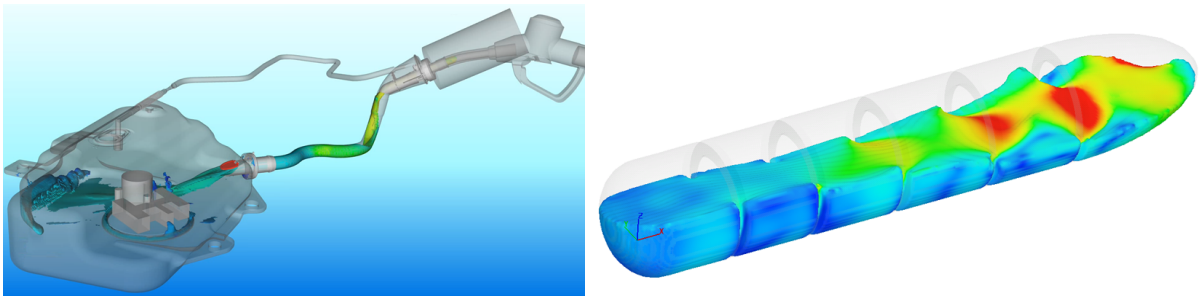

Figure 1.1 – **Left figure:** Nozzle filling simulation, *Courtesy Reutter Group*. **Right figure:** Simulation of fuel sloshing in an aircraft tank. (Simulation result courtesy of Flow Science, Inc., developer of the computational fluid dynamics (CFD) software, FLOW-3D[58]).

The motion of internal on-board liquids (generally fuel, but also cooling liquids, or simply a liquid cargo) can have a significant impact on the vibrational or vibroacoustic behavior, as well as on the dynamical stability of the vehicle (satellite, launcher, aircraft, tanker, *etc.*). This is why, since the end of the 1950s, the aerospace industry has been trying to quantify the influence of the sloshing phenomenon for liquids in on-board tanks. Especially in the context of orbital launchers and the development of Saturn V, for which NASA has launched a major research campaign for quantifying the effects of an internal liquid and of its free-surface sloshing on flight stability. Below, we present a brief history inspired from the one presented in [95].

In this domain, an early 1960s pioneer work was devoted to the analysis of the influence of an internal liquid on the vibration modes of a cylindrical tank [73, 3] and to the analysis of the influence of sloshing on the dynamical behavior of the system [2]. Later, in 1968, some research concerning the stability of partially filled structure were presented in [80, 90]. Numerous analytical or experimental studies for determining the natural frequencies of simple geometrical tanks were also conducted in [27, 76]. Among the precursors of the analysis of hydroelastic phenomena, we can mention, for example, the work published in 1968 [113], presenting one of the first introductions to the concept of added mass matrix, in 1975 [30] for elastic tanks partially filled with liquids, since 1977 [28, 29] for the applications in the nuclear field, and [31] for the research applied to the hydroelasticity of boats. Concerning the effects of surface tension, a particular interest was brought to the equations of capillarity and the conditions of contact

angle between the liquid free surface and the structure in [55, 56, 57]. A theoretical energetic approach for the study of elastic structures containing an incompressible liquid with capillarity effects has recently been introduced in [79]. From a numerical point of view, a first symmetrical variational formulation adapted to finite elements, based on certain approximations is proposed in 1966 [107]. After many studies on various formulations [30, 46, 74], a complete symmetrical variational formulation was finally proposed in [81], allowing for representing, without any simplifying hypothesis, the sloshing, the hydroelastic deformations, the capillarity effects and their possible couplings. In [83], the variational formulations and finite elements discretization for the analysis of complex structures coupled with internal and external acoustic fluids, are explained and detailed. Concerning the sloshing, the influence of gravity on the linear dynamics of a structure containing an incompressible fluid is presented in [95] and an extension to the effects of pressurization in an elastic container is proposed in [96]. In 2010, a study of the statics and dynamics of complex fluid-structure systems taking into account the effects of sloshing with capillarity for a rigid structure was detailed in [53, 54]. Recently, a computational model allowing for considering the effects of sloshing and capillarity in a system constituted by an acoustic fluid and an elastic structure has been presented in [85]. This new formulation allows for taking into account the contact angle condition when considering a deformable structure. These various phenomena are nowadays well understood for each of them, but the coupling effects and their influences on the stability of the concerned mechanical system is still subjects of interest. For example, in the space sector, a well-known and particularly critical example is the Pogo effect, which involves a coupling between hydroelastic deformations of a tank and compressible fluid flows in the fuel pipe admission [109, 108].

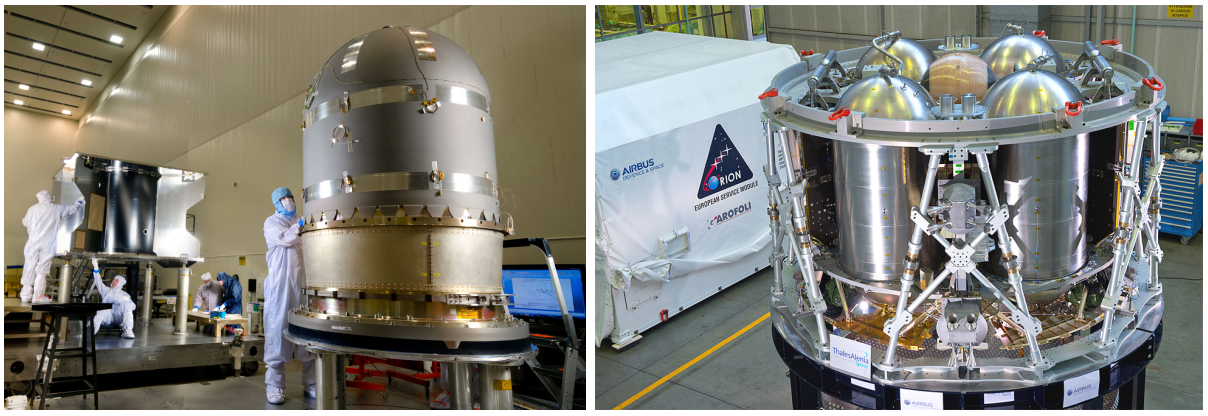

Figure 1.2 – **Left figure:** Hydrazine propellant tank built for NASA's MAVEN spacecraft.*(Credit: Lockheed Martin)*. **Right figure:** Bipropellant tanks integrated to the Structural Test Article of Orion's European Service Module before delivery to NASA Glenn (Image taken from [1]).

The variability of solicitations applied to such fluid-structure coupled systems results in a wide variety of dynamical behaviors and couplings between the different parts of the system. It is easy to dissociate, for example, a vibratory excitation of the free surface sloshing induced by a rigid motion of a kerosene tank in a military ship, from the vibratory excitation of the free surface sloshing caused by the takeoff of an orbital launcher. This latter type of excitation can then induce large amplitude vibrations of shells and panels inducing structural nonlinearities. These nonlinearities have interested many researchers in the past few decades. In some appli-

cations, the vibration response of the structure calculated by linear theory is inaccurate. When the vibration amplitude becomes comparable to the shell thickness, a geometrically nonlinear theory should be used. The effects of the geometrical nonlinearities of structures containing liquids without free surface have been studied in order to quantify the influence of a fluid on the large amplitude motion of the structure [51, 18, 20, 17, 16, 105]. Many experimental studies are available for large amplitude vibrations of thin shells [71, 40, 69] partially filled with liquids such as the ones proposed by [3, 41, 38]. A comprehensive review of studies on geometrically nonlinear vibrations in the context of fluid-structure interaction is proposed in [19]. Recently, a nonlinear model for computational vibration analysis of structures partially filled with acoustic liquid in presence of slohshing and capillarity has been presented in [86].

In the framework of the computational study of fluid-structure coupled systems, it is generally common to associate a significant computational cost. This computational cost is due to several factors related to the complexities of such systems. For the simulation of fluid-structure coupling phenomena, the computational models are generally very large in order to correctly represent the various phenomena. Indeed, in the case of a finite element computational model, the fineness of the numerical mesh of the fluid-structure system has to be sufficiently important for correctly representing the highly flexible motion of the free-surface sloshing and of the thin-walled tank. The dynamical simulation of these coupled systems involves a significant numerical cost given the large frequency range of the system. As explained above, the frequency ranges of each phenomenon are very diverse and extensive, resulting in complex calculations and long simulation times. These long simulation times are all the more important because sloshing is a very weakly damped motion of the free surface compared to vibroacoustic vibrations. It is therefore necessary to introduce reduced-order models for simulating the nonlinear dynamics of such complex coupled fluid-structure systems. The computational linear reduced-order models, adapted to linear fluid-structure interactions, have been studied for instance in [81, 84]. For nonlinear problems, the method of proper orthogonal decomposition (POD) has been used for constructing reduced-order models, for example in [20, 21, 24]. The construction of a modal reduced-order basis in the context of fluid-structure interactions taking into account sloshing and capillarity has been developed in [85] for the linear cases, and an extension to geometrically nonlinear structure is presented in [86].

Nowadays, for all industrial sectors, an important aspect is to take into account the uncertainties in such complex systems. When analyzing and predicting the behavior of coupled fluid-structure systems, it is essential to take into account the variabilities that exist within the systems. The uncertainties in the computational models of the real complex systems can come from several sources that are divided into categories [102] : First, the *aleatory uncertainties* are related to physical phenomena that are random by nature such as, for example, the pressure field in a fully developed turbulent boundary layer. These aleatory uncertainties are not considered in the present work. Second, *epistemic uncertainties* are related to *parameters* of the model, (for which there is a lack of knowledge), and to *modeling errors*, which cannot be described in terms of the parameters of the computational model. For instance, the lack of knowledge in the mechanical description of a boundary condition in a fluid-structure system; or the geometrical tolerances induced by manufacturing processes are epistemic uncertainties. These two types of epistemic uncertainties are respectively called *parameters uncertainties* and *model uncertainties*. Taking into account these uncertainties in the computational model is very important for carrying out robust updating and robust optimization such as robust design with respect to uncertainties. The probabilistic approach for modeling uncertainties on the system parameters is called the

parametric probabilistic approach which consists in constructing the stochastic model of the system parameters using the available information. Such an approach is very well adapted and very efficient to consider the uncertainties in the computational model parameters. Many works have published on parametric uncertainty quantification, for example in [59, 60, 75, 97, 47]. Concerning the model uncertainties induced by modeling errors, the *nonparametric probabilistic approach* has been proposed [99] in 2000, allowing for modeling errors to be taken into account, based on the random matrix theory [77, 102]. In this thesis we are interested in taking into account the model uncertainties induced by the modeling errors in the fluid-structure computational models.

This thesis is in the continuation of the work published in [86], in which we are interested in the dynamics of coupled fluid-structure systems taking into account the effects of sloshing and capillarity. The geometrically nonlinear structure is coupled with a linear acoustic internal liquid that has a free surface. The effects of sloshing and capillarity are taken into account through a new linearized formulation for the contact angle condition between the structure and the free surface of the liquid. This formulation therefore allows, through the linearity of the internal liquid, for quantifying the influence of the geometrical nonlinearities of the structure on the dynamical behavior of the system. The proposed approach for simulating the dynamics of large-scale coupled fluid-structure systems relies on the implementation of a nonlinear reduced-order model. This reduced-order model consists in projecting the equations of the model onto a basis constituted of the modal bases issued from each physical subset of the fluid–structure system, for the following reasons. (i) A better understanding of the couplings between each part of the fluid–structure system can be done. (ii) It allows for filtering the eigenfrequencies of the different physical subsets of the system; it is well known that the frequency gap between the (usually low-frequency) sloshing resonances and the (usually high-frequency) elastic and acoustic resonances is huge ; this means that if we were to build a global reduced-order basis, we would have to compute an untractable number of (weakly energetics) sloshing eigenmodes before reaching any acoustic or elastic eigenmodes. (iii) The computation of a global reduced-order projection basis would induce some difficulties related to the non-symmetric global formulation of the coupled problem. (iv) Such ROM allows for being predictive with a reasonable computational time [82, 84, 8]. This reduced-order model will thus allow for better identifying and describing the coupling mechanisms and energy transfers that occur in such coupled fluid-structure systems. The computational model presented in [86] also allows, through the use of the adapted reduced-order model, for implementing the random matrix theory for the nonparametric uncertainty quantification. Indeed, the nonparametric probabilistic approach of uncertainties [99, 103] has already been applied in the context of fluid-structure systems constituted of elastic structure coupled with an internal acoustic liquid in [52, 35, 103]. With respect to uncertainties, this thesis proposes an extension of the work published in [86].

1.2 Methodologies, novelties of the work, and manuscript organization

The novelties in this work are presented simultaneously with the organization of the manuscript.

- **Chapter 2** presents a summary of the theoretical formulation of the mean (nominal) computational model for the analysis of the dynamics of nonlinear coupled fluid-structure system with sloshing and capillarity effects. The hypotheses under consideration for both the structure and the internal liquid are described in details. The boundary value problem, the associated weak formulation, and the mean nonlinear computational model are then

expressed in terms of the nonlinear displacement of the elastic structure, of the pressure in the acoustic liquid, and of the normal elevation of the free surface. When the capillarity effects are taken into account, the triple line operator in the coupled problem requires the use of more regular displacement field than for the usual cases without the capillarity effects. This implies that quadratic (and not linear) interpolation functions have to be used for the computational model. Finally, the construction of the mean nonlinear reduced-order model (ROM) is presented, detailing the computation of the fluid-structure projection basis and the explicit construction of the geometrically nonlinear stiffness operators of the structure.

- The finite element discretization of the fluid-structure computational model is detailed in **Chapter 3**. This chapter presents the methodology for dicretizing the 3D, 2D, and 1D operators involved in the computational fluid-structure model using the finite element method with quadratic interpolation functions. In this chapter, we present a validation of the proposed methodology by comparing computational results to analytical results or to numerical-benchmarks results.

- **Chapter 4** presents novel results concerning the numerical analysis of the generalized eigenvalue problems devoted to the construction of the reduced-order projection basis (ROB). This novel methodology has been developed for circumventing the computational difficulties and for reducing the cost induced by the construction of the ROB. The construction of the projection basis requires to solve three generalized eigenvalue problems. The first one is related to the elastic structure taking into account the *added-mass* effects induced by the internal liquid and allows the added-mass elastic modes of the structure to be computed. The second one is related to the internal acoustic liquid and allows the acoustic modes to be computed. Finally, the last one is related to the free surface sloshing taking into account the acoustic pressure induced in the internal liquid by the motion of the free surface and allows the capillarity-sloshing modes to be computed. If standard algorithms were used, these three generalized eigenvalue problems would be very expensive when studying large-scale fluid-structure systems and could result in an infeasible calculation on mid-power computers. This is the reason why a novel computational strategy is proposed based on a *double projection* method and on an adapted *subspace iteration* method.

- **Chapter 5** presents new results concerning the role played by the triple line operator involved by the capillarity effects. At the knowledge of the author, these are the first results of this type obtained throughout the literature. These results have been obtained by constructing a dedicated coupled fluid-structure system that allows for exhibiting the contact angle influence when considering a deformable structure. This fluid-structure system has been designed in order to promote the energy transfers between the free surface and the structure through the triple line. The analysis of the influence of this new operator is then carried out on several versions of this fluid-structure system with repect to several values of contact angles. The dynamical responses of the fluid-structure system with and without this triple line operator are then presented in order to demonstrate the importance of this new coupling operator.

- **Chapter 6** revisits and explains an *unexpected* experimental high-amplitude sloshing phenomenon in a vibrating elastic tank, that has never been explained in the open literature. As explained in Section 1.1, an experimental campaign, first designed for analyzing the influence of an internal liquid on the breathing vibrations of a cylindrical tank partially

filled with a liquid, highlighted an *unexpected* low-frequency and high-amplitude motion of the free surface when the tank were submitted to high-frequency excitation. This chapter proposes a reasonable explanation of this *unexpected* phenomenon through a numerical simulation of the geometrically nonlinear fluid-structure system. The computational model is first updated using the available experimental data. Then, using the updated computational model, numerical simulations are performed, which allow for giving a comprehensive overview on the unexpected physical phenomenon that occured during this experiment.

- Finally, **Chapter 7** is devoted to the nonparametric uncertainty propagation in such highly coupled fluid-structure systems. The construction of the nonlinear stochastic reduced-order model (SROM) is carried out using the nonparametric probabilistic approach and is detailed. The application is the one presented in Chapter 6. The nonlinear structural stiffness is modeled using random matrices. Finally, for identifying the hyperparameter of the probabilistic model of the nonlinear structural stiffness giving target responses, we present a methodology based on a least-square optimization problem.

1.3 Notations

In the manuscript, the following notations are used. Let "a" be a mathematical quantity. Related to such a quantity, a deterministic scalar is denoted by a or A and its random counterpart by $\mathbb{a}$ or $\mathbb{A}$; a deterministic vector is denoted by $\mathbf{a}$ or $\mathbf{A}$ and its random counterpart by $\mathbb{a}$ or $\mathbb{A}$; a deterministic matrix is denoted by $[A]$ and its random counterpart by $[\mathbb{A}]$; a second-order tensor is denoted by $\underline{\underline{A}}$.

Some particular cases are defined hereinafter, $\mathbb{R}$ denotes the set of real numbers, $\mathbb{R}^p$ denotes the euclidian space of dimension p, $\mathbb{M}_{m,n}$ denotes the set of real $(m \times n)$ matrices, $\mathbb{M}_n$ denotes the set of real square matrices of size n, $\mathbb{M}_n^+$ denotes the set of positive-definite real square matrices of size n, and $\mathbb{B}$ denotes a frequency band.

The entries of a given vector $\mathbf{a}$ in $\mathbb{R}^n$ and of a given matrix $[A]$ in $\mathbb{M}_n$ are denoted respectively a_j and A_{ij} for i and j in $\{1, \ldots, n\}$. The summation over repeated greek and latin indices is used in the whole manuscript. If $\mathbf{a} \in \mathbb{R}^n$ and $\mathbf{b} \in \mathbb{R}^n$, the inner product (or scalar product) between $\mathbf{a}$ and $\mathbf{b}$ is defined by $< \mathbf{a}, \mathbf{b} >$ or $\mathbf{a} \cdot \mathbf{b}$ and is equal to $a_j\, b_j$. For a given function g sufficiently regular, the partial derivative $\partial g(\mathbf{x})/\partial x_j$ is denoted as $g_{,j}(\mathbf{x})$. The first- and second-time derivatives of g are defined by $\dot{g}(\mathbf{x}, t) = \partial g(\mathbf{x}, t)/\partial t$, and $\ddot{g}(\mathbf{x}, t) = \partial^2 g(\mathbf{x}, t)/\partial t^2$. The gradient $\nabla_{\mathbf{x}}\, \mathbf{g}(\mathbf{x}, t)$ of function $\mathbf{g}$ with respect to $\mathbf{x}$ is defined by $(\nabla_{\mathbf{x}}\, \mathbf{g}(\mathbf{x}, t))_{ij} = g_{i,j}$. The Fourier transform of the function $t \mapsto g(\mathbf{x}, t)$, with respect to time, is denoted by $\widehat{g}(\mathbf{x}, \omega)$ and is defined by

$$\widehat{g}(\mathbf{x}, \omega) = \int_{-\infty}^{+\infty} e^{-i\omega t}\, g(\mathbf{x}, t)\, dt \quad . \tag{1.1}$$

The Euclidian norm $\| \mathbf{A} \|$ of vector $\mathbf{A}$ in $\mathbb{R}^n$ is $\| \mathbf{A} \| = < \mathbf{A}, \mathbf{A} >^{\frac{1}{2}} = \sqrt{\sum_{i=1}^n A_i^2}$. The Frobenius norm $\| [A] \|_F$ of matrix $[A]$ in $\mathbb{M}_n$ is $\| [A] \|_F^2 = < [A], [A] >_F = Tr([A]^T\, [A])$. In order to simplify the notations, the time and space dependencies are omitted when no confusion is possible.

Chapter 2

Theoretical formulation of the mean fluid-structure computational model

Contents

2.1 Hypotheses for the fluid-structure system

The physical space is referred to a cartesian reference system $(\mathbf{O}, \mathbf{e}_1, \mathbf{e}_2, \mathbf{e}_3)$ and the generic point in this reference system is denoted by $\mathbf{x} = (x_1, x_2, x_3)$. The structure under consideration is assumed to be elastic and to undergo large displacements that are induced by geometrical nonlinearities. The considered constitutive equation for such material is a Saint-Venant Kirchhoff constitutive equation. At equilibrium, the structure occupies a bounded volume Ω_u and is taken in its natural state without prestresses. The unknown displacement field $\mathbf{u}$ of the structure is expressed in the reference coordinate system as $\mathbf{u}(\mathbf{x}, t) = (u_1(\mathbf{x}, t), u_2(\mathbf{x}, t), u_3(\mathbf{x}, t))$. This structure contains an internal dissipative acoustic liquid [86] occupying a bounded domain Ω_p, assumed to be at rest in the reference configuration. For additional details regarding the dissipation in acoustic fluids we refer the reader to [72, 89, 34]. The unknown pressure in the acoustic internal liquid is denoted by $p(\mathbf{x}, t)$. Gravitational and surface tension effects are taken into account but internal gravity waves are neglected. The free surface of the liquid is therefore subject to the effects of sloshing, which is considered to be linear, *i.e.* only the small vibrations around the reference configuration are considered. The normal elevation of the free-surface is denoted by $h(\mathbf{x}, t)$. The capillarity effects on the triple line between the structure, the fluid, and its free surface are taken into account through a novel formulation for the linearized contact angle. The

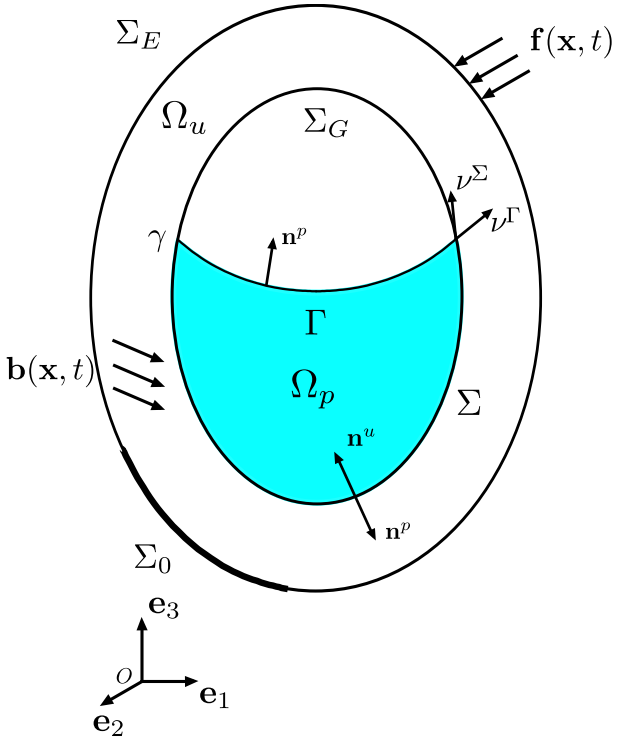

Figure 2.1 – Reference configuration of the coupled fluid-structure system

fluid-structure system is considered to be taken in its natural state without pre-stresses defined as the *reference configuration*, (see Figure 2.1).

The boundary of Ω_p, assumed to be smooth, is denoted by $\partial\Omega_p = \Sigma \cup \gamma \cup \Gamma$ (with Σ and Γ open sets such that $\Sigma \cap \gamma = \varnothing$, $\Gamma \cap \gamma = \varnothing$, and $\Sigma \cap \Gamma = \varnothing$), where Σ is the fluid-structure interface, Γ is the free surface of the liquid and γ is the triple contact line between the structure and the liquid (called *triple line*). The boundary of Ω_u, assumed to be smooth, is denoted as $\partial\Omega_u = \Sigma_0 \cup \Sigma_E \cup \Sigma \cup \gamma \cup \Sigma_G$ where Σ_0 is a part of the boundary in which there is the Dirichlet condition $\mathbf{u} = 0$, where Σ_E is the external surface of the structure and Σ_G is the structure internal wall without contact with the liquid. The structure is submitted to a given body force field $\mathbf{b}$ in Ω_u and to a given surface force field $\mathbf{f}$ on Σ_E. The external unitary normals to $\partial\Omega_u$ and $\partial\Omega_p$ are written $\mathbf{n}^u$ and $\mathbf{n}^p$. Let $\boldsymbol{\nu}^\Gamma$ and $\boldsymbol{\nu}^\Sigma$ be the external unit normals to γ belonging respectively to the tangent plane to Γ and to the tangent plane to Σ. The gravity vector is denoted $\mathbf{g} = -g\,\mathbf{e}_3$ with g the gravitational constant.

2.2 Boundary value problem for the nonlinear coupled fluid-structure system

The fluid-structure boundary value problem is expressed in terms of structural displacement field $\mathbf{u}(\mathbf{x},t)$, of internal pressure field $p(\mathbf{x},t)$, and of normal displacement field $h(\mathbf{x},t)$ of the free surface. The nonlinear boundary value problem in $(p,h,\mathbf{u})$ is written as,

$$\frac{1}{\rho_0 c_0^2}\,\ddot{p} - \frac{\tau}{\rho_0}\nabla^2\dot{p} - \frac{1}{\rho_0}\nabla^2 p = 0 \quad \text{in } \Omega_p\,, \tag{2.1}$$

$$\left(1 + \tau\frac{\partial}{\partial t}\right)\frac{\partial p}{\partial \mathbf{n}^p} = -\rho_0\,\ddot{\mathbf{u}}\cdot\mathbf{n}^p \quad \text{on } \Sigma\,, \tag{2.2}$$

$$\left(1+\tau\frac{\partial}{\partial t}\right)\frac{\partial p}{\partial \mathbf{n}^p}=-\rho_0\,\ddot{h}\quad \text{on } \Gamma\ , \tag{2.3}$$

$$p=\rho_0\,h\,g\,(\mathbf{e}_z\cdot\mathbf{n}^p)-\sigma_\Gamma\left\{\left(\frac{1}{R_1^2}+\frac{1}{R_2^2}\right)h+\nabla_\Gamma^2 h\right\}\quad \text{on } \Gamma\ , \tag{2.4}$$

$$\frac{\partial h}{\partial \boldsymbol{\nu}^\Gamma}=c_h\,h+\mathcal{J}\,\mathbf{u}\quad \text{on } \gamma\ , \tag{2.5}$$

$$\rho_S\,\ddot{\mathbf{u}}-\text{div}\,(\underline{\underline{F}}\cdot\underline{\underline{S}})=\mathbf{b}\quad \text{in } \Omega_u\ , \tag{2.6}$$

$$\mathbf{u}=\mathbf{0}\quad \text{on } \boldsymbol{\Sigma_0}\ , \tag{2.7}$$

$$(\underline{\underline{F}}\cdot\underline{\underline{S}})\cdot\mathbf{n}^u=\mathbf{f}\quad \text{on } \Sigma_E\ , \tag{2.8}$$

$$(\underline{\underline{F}}\cdot\underline{\underline{S}})\cdot\mathbf{n}^u=-\mathbb{1}_\Sigma\,p\,\mathbf{n}^u+\sigma_\Gamma\,(\mathcal{J}'h)\quad \text{on } \Sigma\cup\gamma\cup\Sigma_G\quad , \tag{2.9}$$

Eqs. (2.1) to (2.3) are related to the internal acoustic fluid and its boundary conditions. Eq. (2.1) is related to the internal inviscid compressible liquid, with an additional small damping term, which corresponds to the classical Helmholtz equation with a dissipative term. In Eq. (2.1), ρ_0 is the constant mass density of the homogeneous liquid, c_0 is the constant speed of sound, and τ is the constant coefficient that characterizes the dissipation in the internal liquid. Eq. (2.2) is the fluid-structure coupling condition of the internal inviscid compressible liquid (weakly dissipative) with the structure interface Σ. Eq. (2.3) represents the kinematic equation for the free surface Γ.

Eqs. (2.4) and (2.5) are related to the free-surface of the acoustic fluid and its boundary conditions. Eq. (2.4) corresponds to the free-surface constitutive equation of surface Γ, in which σ_Γ is the surface tension coefficient, R_1 and R_2 are the main curvature radii of the free-surface, and $\nabla_\Gamma^2 h$ denotes the surface Laplacian related to surface Γ. In Eq. (2.5), the first term of the right-hand side corresponds to the classical contact angle condition on γ in which c_h is the first the contact angle coefficient [81] defined by

$$c_h=\frac{<K_\Gamma>\cos(\theta)-<K_\Sigma>}{\sin(\theta)}\quad , \tag{2.10}$$

in which θ is the contact angle on the triple line γ, and where $<K_\Gamma>$ (respec. $<K_\Sigma>$) is the local curvature of the intersection of Γ (respec. Σ) with the normal plane to γ. The operator $\mathcal{J}$ is defined [85] by

$$\mathcal{J}\,\mathbf{u}=d_h\,\mathbf{u}\cdot\mathbf{n}^u-\frac{\partial(\mathbf{u}\cdot\mathbf{n}^u)}{\partial\boldsymbol{\nu}^\Sigma}\quad , \tag{2.11}$$

in which the second contact angle coefficient d_h [81] is defined by

$$d_h=\frac{<K_\Gamma>-<K_\Sigma>\cos(\theta)}{\sin(\theta)}\quad . \tag{2.12}$$

Eqs. (2.6) to (2.9) are related to the elastic structure with geometrical nonlinearities and its boundary conditions. Eq. (2.6) corresponds to the dynamic equation for the nonlinear structure in the time domain, in which ρ_S is the constant mass density of the structure. The second order tensor $\underline{\underline{F}}$ is the deformation gradient tensor defined in Ω_u by

$$F_{ij}=\delta_{ij}+u_{i,j}\quad , \tag{2.13}$$

where δ_{ij} denotes the Kronecker symbol such that $\delta_{ij} = 1$ if $i = j$ and $\delta_{ij} = 0$ otherwise. In Eq. (2.9), the tensor $\underline{\underline{S}}$ is the second Piola-Kirchhoff symmetric tensor in the reference configuration written as

$$S_{ij} = C_{ijk\ell}\, E_{k\ell} \quad , \tag{2.14}$$

where the tensor $C_{ijk\ell}$ is the fourth-order elasticity tensor, verifying the symmetry and positiveness properties and where the Green-Lagrange strain tensor is written as

$$E_{k\ell} = \varepsilon_{k\ell}(\mathbf{u}) + \eta_{k\ell}(\mathbf{u}) \quad , \tag{2.15}$$

in which

$$\varepsilon_{k\ell} = \frac{1}{2}(u_{k,\ell} + u_{\ell,k}) \quad \text{and} \quad \eta_{k\ell} = \frac{1}{2} u_{m,k}\, u_{m,\ell} \quad . \tag{2.16}$$

Note that the dissipative term in the structure will directly be added in the computational model. The boundary condition defined by Eq. (2.7) corresponds to a Dirichlet boundary condition on Σ_0. Eq. (2.8) corresponds to the boundary condition on Σ_E on which a given surface force field is applied. The second term in the right-hand side of Eq. (2.9), that has been introduced in [85], is a new term related to capillarity, which allows for taking into account the contact angle condition when considering an elastic structure with geometrical nonlinearities. A short summary of the construction of this boundary condition is presented in [85, 86]. The term $(\mathcal{J}'h)$ is a generalized function whose support is γ and is defined by duality of the term $\mathcal{J}\,\mathbf{u}$. We thus have

$$< \mathcal{J}\,\mathbf{u}, h >_{d\gamma} = \int_\gamma (\mathcal{J}\,\mathbf{u})\, h\, d\gamma \quad , \tag{2.17}$$

$$\ll \mathbf{u}, \mathcal{J}'\, h \gg_{d\mu_\gamma} = < \mathcal{J}\,\mathbf{u}, h >_{d\gamma} \quad . \tag{2.18}$$

2.3 Weak formulation for the coupled nonlinear fluid-structure system

Let $C_{\text{ad,p}}$, $C_{\text{ad,h}}$, and $C_{\text{ad,u}}$ be the admissible spaces defined by

$$C_{\text{ad,p}} = \{p \in \Omega_p,\ p \text{ sufficiently regular}\} \quad , \tag{2.19}$$

$$C_{\text{ad,h}} = \{h \in \Gamma,\ h \text{ sufficiently regular}\} \quad , \tag{2.20}$$

$$C_{\text{ad,u}} = \{\mathbf{u} \in \Omega_u,\ \mathbf{u} \text{ sufficiently regular}\} \quad , \tag{2.21}$$

and let $C^0_{\text{ad,u}}$ be the admissible space defined by

$$C^0_{\text{ad,u}} = \{\mathbf{u} \in \mathscr{C}_u,\ \mathbf{u} = \mathbf{0} \text{ on } \boldsymbol{\Sigma_0}\} \quad . \tag{2.22}$$

The weak formulation of the nonlinear boundary value problem described by Eq. (2.1) to (2.9) consists in finding the unknown fields $(p(\cdot,t), h(\cdot,t), \mathbf{u}(\cdot,t)) \in \{C_{\text{ad,p}} \times C_{\text{ad,h}} \times C^0_{\text{ad,u}}\}$ such that, for all $(\delta p, \delta h, \delta\mathbf{u}) \in \{C_{\text{ad,p}} \times C_{\text{ad,h}} \times C^0_{\text{ad,u}}\}$ we have

$$\mathscr{M}_p(\ddot{p}, \delta p) + \mathscr{D}_p(\dot{p}, \delta p) + \mathscr{K}_p(p, \delta p) - \mathscr{C}_{up}(\ddot{\mathbf{u}}, \delta p) - \mathscr{C}_{hp}(\ddot{h}, \delta p) = 0 \quad , \tag{2.23}$$

$$\mathscr{C}_{ph}(p, \delta h) + \mathscr{K}_g(h, \delta h) + \mathscr{K}^s_c(h, \delta h) + \mathscr{K}^l_c(h, \delta h) + \mathscr{C}_{hu}(\mathbf{u}, \delta h) = 0 \quad , \tag{2.24}$$

$$\mathscr{C}_{pu}(p, \delta\mathbf{u}) + \mathscr{C}_{uh}(h, \delta\mathbf{u}) + \mathscr{M}_u(\ddot{\mathbf{u}}, \delta\mathbf{u}) + \mathscr{D}_u(\dot{\mathbf{u}}, \delta\mathbf{u}) + \mathscr{K}_{\text{NL}}(\mathbf{u}, \delta\mathbf{u}) = \mathscr{F}(\delta\mathbf{u}) \quad . \tag{2.25}$$

The linear and bilinear forms expressed in Eqs. (2.23) to (2.25) are described hereinafter

- The bilinear forms $\mathscr{M}_p(p,\delta p)$ and $\mathscr{M}_u(\mathbf{u},\delta\mathbf{u})$ are defined by

$$\mathscr{M}_p(p,\delta p)=\frac{1}{\rho_0 c_0^2}\int_{\Omega_p} p\,\delta p\,d\mathbf{x} \quad \text{and} \quad \mathscr{M}_u(\mathbf{u},\delta\mathbf{u})=\rho_S\int_{\Omega_u}\mathbf{u}\cdot\delta\mathbf{u}\,d\mathbf{x} \quad , \tag{2.26}$$

and have the following positive-definiteness properties:

$$\mathscr{M}_p(p,\delta p)=\mathscr{M}_p(\delta p,p) \quad \text{with} \quad \mathscr{M}_p(p,p)>0 \quad , \tag{2.27}$$

$$\mathscr{M}_u(\mathbf{u},\delta\mathbf{u})=\mathscr{M}_u(\delta\mathbf{u},\mathbf{u}) \quad \text{with} \quad \mathscr{M}_u(\mathbf{u},\mathbf{u})>0 \quad , \tag{2.28}$$

- The bilinear form $\mathscr{D}_p(p,\delta p)$ is defined by

$$\mathscr{D}_p(p,\delta p)=\frac{\tau}{\rho_0}\int_{\Omega_p}(\nabla p)\cdot(\nabla\delta p)\,d\mathbf{x} \quad , \tag{2.29}$$

and have the following positive-semidefiniteness properties:

$$\mathscr{D}_p(p,\delta p)=\mathscr{D}_p(\delta p,p) \quad \text{with} \quad \mathscr{D}_p(p,p)\geq 0 \quad . \tag{2.30}$$

As explained in Section 2.2, the structural damping bilinear form is added in the equations of the problem and is defined by

$$\mathscr{D}_u(\mathbf{u},\delta\mathbf{u})=\tau_S\int_{\Omega_u}(\nabla\mathbf{u})\cdot(\nabla\delta\mathbf{u})\,d\mathbf{x} \quad , \tag{2.31}$$

and have the following positive-definiteness properties:

$$\mathscr{D}_u(\mathbf{u},\delta\mathbf{u})=\mathscr{D}_u(\delta\mathbf{u},\mathbf{u}) \quad \text{with} \quad \mathscr{D}_u(\mathbf{u},\mathbf{u})>0 \quad . \tag{2.32}$$

- The bilinear forms $\mathscr{K}_p(p,\delta p)$, $\mathscr{K}_c^s(h,\delta h)$, $\mathscr{K}_c^l(h,\delta h)$, and $\mathscr{K}_g(h,\delta h)$ are defined by

$$\mathscr{K}_p(p,\delta p)=\frac{1}{\rho_0}\int_{\Omega_p}(\nabla p)\cdot(\nabla\delta p)\,d\mathbf{x} \quad , \quad \mathscr{K}_g(h,\delta h)=\rho_0\int_\Gamma h\,(\mathbf{g}\cdot\mathbf{n}^p)\,\delta h\,ds \quad , \tag{2.33}$$

$$\mathscr{K}_c^s(h,\delta h)=-\sigma_\Gamma\int_\Gamma\left(\frac{1}{R_1^2}+\frac{1}{R_2^2}\right)h\,\delta h\,ds+\sigma_\Gamma\int_\Gamma(\nabla_\Gamma h)\cdot(\nabla_\Gamma\delta h)\,ds \quad , \tag{2.34}$$

$$\mathscr{K}_c^l(h,\delta h)=-\sigma_\Gamma\int_\gamma c_h\,h\,\delta h\,d\gamma \quad . \tag{2.35}$$

and have the following positive semi-definiteness and positive-definiteness properties:

$$\mathscr{K}_p(p,\delta p)=\mathscr{K}_p(\delta p,p) \quad \text{with} \quad \mathscr{K}_p(p,p)\geq 0 \quad , \tag{2.36}$$

$$\mathscr{K}_g(h,\delta h)=\mathscr{K}_g(\delta h,h) \quad \text{with} \quad \mathscr{K}_g(h,h)>0 \quad , \tag{2.37}$$

$$\mathscr{K}_c^s(h,\delta h)=\mathscr{K}_c^s(\delta h,h), \quad \mathscr{K}_c^l(h,\delta h)=\mathscr{K}_c^l(\delta h,h) \quad \text{with} \quad \mathscr{K}_c^s(h,h)+\mathscr{K}_c^l(h,h)>0, \tag{2.38}$$

- The coupling bilinear forms $\mathscr{C}_{pu}(p,\delta\mathbf{u})$, $\mathscr{C}_{ph}(p,\delta h)$, and $\mathscr{C}_{hu}(\mathbf{u},\delta h)$ are defined by

$$\mathscr{C}_{pu}(p,\delta\mathbf{u})=-\int_\Sigma p\,(\mathbf{n}^p\cdot\delta\mathbf{u})\,ds \quad , \quad \mathscr{C}_{ph}(p,\delta h)=-\int_\Gamma p\,\delta h\,ds \quad , \tag{2.39}$$

$$\mathscr{C}_{hu}(\mathbf{u},\delta h) = -\sigma_\Gamma \int_\gamma (\mathcal{J}\,\mathbf{u})\,\delta h\,d\gamma \quad . \tag{2.40}$$

and we introduce the following associated bilinear forms,

$$\mathscr{C}_{pu}(p,\mathbf{u}) = \mathscr{C}_{up}(\mathbf{u},p) \quad , \tag{2.41}$$

$$\mathscr{C}_{ph}(p,h) = \mathscr{C}_{hp}(h,p) \quad , \tag{2.42}$$

$$\mathscr{C}_{hu}(\mathbf{u},h) = \mathscr{C}_{uh}(h,\mathbf{u}) \quad , \tag{2.43}$$

- The linear form $\mathscr{F}(\delta\mathbf{u})$ is defined by

$$\mathscr{F}_u(\delta\mathbf{u}) = \int_{\Sigma_E} \mathbf{f}\cdot\delta\mathbf{u}\,ds + \int_{\Omega_u} \mathbf{b}\cdot\delta\mathbf{u}\,d\mathbf{x} \quad . \tag{2.44}$$

The geometrical nonlinearities of the structure induced by the Saint-Venant Kirchhoff constitutive equation Eq. (2.14) and expressed in $\mathscr{K}_{\rm NL}(\mathbf{u},\delta\mathbf{u})$, can be developped in order to show all the linear and nonlinear contributions to internal forces. Such formulation allows for introducing the decomposition into three multi-linear forms: a linear, a quadratic and a cubic one such that

$$\mathscr{K}_{\rm NL}(\mathbf{u},\delta\mathbf{u}) = \int_{\Omega_u} F_{ik}\,S_{kj}\,\delta u_{i,j}\,d\mathbf{x} \tag{2.45}$$

$$= \int_{\Omega_u} C_{ijpq}\,(u_{p,q}+u_{q,p})\,\delta u_{i,j}\,d\mathbf{x} + \int_{\Omega_u} C_{ijpq}\,u_{s,p}\,u_{s,q}\,\delta u_{i,j}\,d\mathbf{x} + \int_{\Omega_u} u_{i,k}\,C_{kjpq}\,(u_{p,q}+u_{q,p})\,\delta u_{i,j}\,d\mathbf{x} + \int_{\Omega_u} u_{i,k}\,C_{kjpq}\,u_{s,p}\,u_{s,q}\,\delta u_{i,j}\,d\mathbf{x} \tag{2.46}$$

By using the symmetry properties of C_{ijpq}, one can write

$$\mathscr{K}_{\rm NL}(\mathbf{u},\delta\mathbf{u}) = \int_{\Omega_u} \varepsilon_{ij}(\delta\mathbf{u})\,C_{ijpq}\,\varepsilon_{pq}(\mathbf{u})\,d\mathbf{x} + \int_{\Omega_u} \varepsilon_{ij}(\delta\mathbf{u})\,C_{ijpq}\,\eta_{pq}(\mathbf{u})\,d\mathbf{x} + \int_{\Omega_u} u_{i,k}\,C_{kjpq}\,\varepsilon_{pq}(\mathbf{u})\,\delta u_{i,j}\,d\mathbf{x} + \int_{\Omega_u} u_{i,k}\,C_{kjpq}\,\eta_{pq}(\mathbf{u})\,\delta u_{i,j}\,d\mathbf{x} \quad . \tag{2.47}$$

Finally, we then obtain

$$\mathscr{K}_{\rm NL}(\mathbf{u},\delta\mathbf{u}) = \mathscr{K}_u(\mathbf{u},\delta\mathbf{u}) + \mathscr{K}^{(2)}(\mathbf{u},\mathbf{u},\delta\mathbf{u}) + \mathscr{K}^{(3)}(\mathbf{u},\mathbf{u},\mathbf{u},\delta\mathbf{u}) \quad , \tag{2.48}$$

in which

$$\mathscr{K}_u(\mathbf{u},\delta\mathbf{u}) = \int_{\Omega_u} \varepsilon_{ij}(\delta\mathbf{u})\,C_{ijpq}\,\varepsilon_{pq}(\mathbf{u})\,d\mathbf{x} \quad , \tag{2.49}$$

is the bilinear form corresponding the elastic stiffness of the structure, and where

$$\mathscr{K}^{(2)}(\mathbf{u},\mathbf{u},\delta\mathbf{u}) = \int_{\Omega_u} \varepsilon_{ij}(\delta\mathbf{u})\,C_{ijpq}\,\eta_{pq}(\mathbf{u})\,d\mathbf{x} + \int_{\Omega_u} u_{i,k}\,C_{kjpq}\,\varepsilon_{pq}(\mathbf{u})\,\delta u_{i,j}\,d\mathbf{x} \quad ,$$

$$\mathscr{K}^{(3)}(\mathbf{u},\mathbf{u},\mathbf{u},\delta\mathbf{u}) = \int_{\Omega_u} u_{i,k}\,C_{kjpq}\,\eta_{pq}(\mathbf{u})\,\delta u_{i,j}\,d\mathbf{x} \quad , \tag{2.50}$$

are tri-linear and quadri-linear forms corresponding to the quadratic and cubic contributions.

2.4 Mean discretized computational model of the fluid-structure system

The computational model is constructed using the finite element method. With respect to space variable $\mathbf{x}$, the discretization of the test functions δp, δh, and $\delta \mathbf{u}$ belonging to the admissible sets $C_{\text{ad,p}}$, $C_{\text{ad,h}}$, and $C_{\text{ad,u}}$ consists in constructing the subspaces $C^{\epsilon}_{\text{ad,p}}$, $C^{\epsilon}_{\text{ad,h}}$, and $C^{\epsilon}_{\text{ad,u}}$ of finite dimensions n_p, n_h, and n_u. Let $(e^p_1, \ldots, e^p_{n_p})$, be a set of interpolation functions that generate subspace $C^{\epsilon}_{\text{ad,p}}$. Let $(e^h_1, \ldots, e^h_{n_h})$, be a set of interpolation functions that generate subspace $C^{\epsilon}_{\text{ad,h}}$. Let $(e^u_1, \ldots, e^u_{n_u})$, be a set of interpolation functions that generate subspace $C^{\epsilon}_{\text{ad,u}}$. The finite element discretization δp^{ϵ}, δh^{ϵ}, and $\delta \mathbf{u}^{\epsilon}$ of test function δp, δh, and $\delta \mathbf{u}$ is

$$\delta p^{\epsilon}(\mathbf{x}) = \sum_{j=1}^{n_p} \delta P_j \, e^p_j \quad , \quad \delta h^{\epsilon}(\mathbf{x}) = \sum_{j=1}^{n_h} \delta H_j \, e^h_j \quad , \quad \delta \mathbf{u}^{\epsilon}(\mathbf{x}) = \sum_{j=1}^{n_u} \delta U_j \, e^u_j \quad . \tag{2.51}$$

Let then denote by $\delta \mathbf{P} = (\delta P_1, \ldots, \delta P_{n_p})$, $\delta \mathbf{H} = (\delta H_1, \ldots, \delta H_{n_h})$, and $\delta \mathbf{U} = (\delta U_1, \ldots, \delta U_{n_u})$, the $\mathbb{R}^{n_p}$-vector, the $\mathbb{R}^{n_h}$-vector, and the $\mathbb{R}^{n_u}$-vector corresponding to the discretization of the unknowns $p(\mathbf{x}, t)$, $h(\mathbf{x}, t)$, and $\mathbf{u}(\mathbf{x}, t)$. The discretization of the linear and bilinear forms of the coupled fluid-structure problem described in Section 2.3 is detailed in the following.

- The bilinear forms defined in Eq.(2.26) are discretized such that

$$\mathscr{M}_p(p, \delta p) \Longrightarrow \delta \mathbf{P}^T \, [M_p] \, \mathbf{P} \quad \text{and} \quad \mathscr{M}_u(u, \delta \mathbf{u}) \Longrightarrow \delta \mathbf{U}^T \, [M_u] \, \mathbf{U} \quad , \tag{2.52}$$

  in which $[M_p]$ and $[M_u]$ are $(n_p \times n_p)$ and $(n_u \times n_u)$ matrices of the fluid-structure system with positive-definiteness properties.

- The bilinear forms defined in Eqs.(2.29) and (2.31) are discretized such that

$$\mathscr{D}_p(p, \delta p) \Longrightarrow \delta \mathbf{P}^T \, [D_p] \, \mathbf{P} \quad \text{and} \quad \mathscr{D}_u(\mathbf{u}, \delta \mathbf{u}) \Longrightarrow \delta \mathbf{U}^T \, [D_u] \, \mathbf{U} \quad , \tag{2.53}$$

  in which $[D_p]$ and $[D_u]$ are $(n_p \times n_p)$ and $(n_u \times n_u)$ matrices of the fluid-structure system with positive-semidefiniteness properties.

- The bilinear forms defined in Eqs.(2.33) to (2.35) and (2.49) are discretized such that

$$\mathscr{K}_p(p, \delta p) \Longrightarrow \delta \mathbf{P}^T \, [K_p] \, \mathbf{P} \quad , \quad \mathscr{K}_g(h, \delta h) \Longrightarrow \delta \mathbf{H}^T \, [K_g] \, \mathbf{H} \quad , \tag{2.54}$$

$$\mathscr{K}^s_c(h, \delta h) \Longrightarrow \delta \mathbf{H}^T \, [K^s_c] \, \mathbf{H} \quad , \quad \mathscr{K}^l_c(h, \delta h) \Longrightarrow \delta \mathbf{H}^T \, [K^l_c] \, \mathbf{H} \quad , \tag{2.55}$$

$$\mathscr{K}_u(\mathbf{u}, \delta \mathbf{u}) \Longrightarrow \delta \mathbf{U}^T \, [K_u] \, \mathbf{U} \quad , \tag{2.56}$$

  in which $[K_p]$, $[K_g]$, $[K^s_c]$, $[K^l_c]$, and $[K_u]$ are respectively $(n_p \times n_p)$, $(n_h \times n_h)$, $(n_h \times n_h)$, $(n_h \times n_h)$, and $(n_u \times n_u)$ matrices. In the following, we introduce the $(n_h \times n_h)$ matrix $[K_{gc}]$ such that

$$[K_{gc}] = [K_g] + [K^s_c] + [K^l_c] \quad . \tag{2.57}$$

  Remark 1: The discretization of the quadratic and cubic stiffness forms $\mathscr{K}^{(2)}(\mathbf{u}, \mathbf{u}, \delta \mathbf{u})$ and $\mathscr{K}^{(3)}(\mathbf{u}, \mathbf{u}, \mathbf{u}, \delta \mathbf{u})$ is written as an equivalent nonlinear restoring force denoted by $\mathbf{F}_{\text{NL}}(\mathbf{U})$ and expressed by

$$\mathscr{K}^{(2)}(\mathbf{u}, \mathbf{u}, \delta \mathbf{u}) + \mathscr{K}^{(3)}(\mathbf{u}, \mathbf{u}, \mathbf{u}, \delta \mathbf{u}) \Longrightarrow \delta \mathbf{U}^T \mathbf{F}_{\text{NL}}(\mathbf{U}) \quad . \tag{2.58}$$

- The discretization of the bilinear forms corresponding to the coupling terms defined by Eqs. (2.39) and (2.40) yields

$$\mathscr{C}_{pu}(p,\mathbf{u}) = \mathscr{C}_{up}(\mathbf{u},p) \Longrightarrow \mathbf{U}^T[C_{pu}]\mathbf{P} = \mathbf{P}^T[C_{up}]\mathbf{U} \quad , \tag{2.59}$$

  in which $[C_{pu}]$ and $[C_{up}]$ are the $(n_u \times n_p)$ and $(n_p \times n_u)$ real rectangular matrices representing the coupling between the structure and the liquid such that $[C_{pu}] = [C_{up}]^T$.

$$\mathscr{C}_{ph}(p,h) = \mathscr{C}_{hp}(h,p) \Longrightarrow \mathbf{H}^T[C_{ph}]\mathbf{P} = \mathbf{P}^T[C_{hp}]\mathbf{H} \quad , \tag{2.60}$$

  in which $[C_{ph}]$ and $[C_{hp}]$ are the $(n_h \times n_p)$ and $(n_p \times n_h)$ real rectangular matrices representing the coupling between the liquid and its free surface such that $[C_{ph}] = [C_{hp}]^T$.

$$\mathscr{C}_{hu}(\mathbf{u},h) = \mathscr{C}_{uh}(h,\mathbf{u}) \Longrightarrow \mathbf{H}^T[C_{hu}]\mathbf{U} = \mathbf{U}^T[C_{uh}]\mathbf{H} \quad , \tag{2.61}$$

  in which $[C_{hu}]$ and $[C_{uh}]$ are the $(n_h \times n_u)$ and $(n_u \times n_h)$ real rectangular matrices representing the coupling between the structure and the free surface of the liquid such that $[C_{hu}] = [C_{uh}]^T$.

- The external force linear form defined in Eq. (2.44) is discretized such that

$$\mathscr{F}_u(\delta\mathbf{u}) \Longrightarrow \delta\mathbf{U}^T\,\mathbf{F}_u \quad , \tag{2.62}$$

  in which $\mathbf{F}_u$ is the $\mathbb{R}^{n_u}$ vector of the external force applied to the struture.

The mean nonlinear computational finite element model of the coupled fluid-structure system is then written as

$$[M_p]\,\ddot{\mathbf{P}} + [D_p]\,\dot{\mathbf{P}} + [K_p]\,\mathbf{P} - [C_{ph}]^T\,\ddot{\mathbf{H}} - [C_{pu}]^T\,\ddot{\mathbf{U}} = 0 \quad , \tag{2.63}$$

$$[C_{ph}]\,\mathbf{P} + [K_{gc}]\,\mathbf{H} + [C_{hu}]\,\mathbf{U} = 0 \quad , \tag{2.64}$$

$$[C_{pu}]\,\mathbf{P} + [C_{hu}]^T\,\mathbf{H} + [M_u]\,\ddot{\mathbf{U}} + [D_u]\,\dot{\mathbf{U}} + [K_u]\,\mathbf{U} + \mathbf{F}_{\text{NL}}(\mathbf{U}) = \mathbf{F}_u \quad . \tag{2.65}$$

It should be noted that the computation of such nonlinear coupled differential equations remains difficult to achieve due to the large number of unknowns in a complex system. It is thus essential to introduce a strategy for constructing a reduced-order model in order de get a reasonable number of unknowns in the problem.

Remark 2: The presence of the generalized function $\mathcal{J}'\,h$, with support γ, in the boundary conditions defined by Eq. (2.9) requires the introduction of admissible sets that are more regular than in the usual weak formulation for which this term would not appear (when capillarity effects are not considered). This implies that the interpolation functions must be quadratic (at least) and cannot be linear (see [87] for the mathematical developments).

2.5 Construction of the mean nonlinear reduced-order model

The proposed mean nonlinear reduced-order model (mean ROM) requires to define a decomposition of the admissible space of the coupled fluid-structure problem taking into account the assumptions that have been introduced. The projection basis is constructed by "blocks" because of the subsequent scale effects between the structural, acoustical, and sloshing dynamical behaviors. The vector basis is then computed in three steps, each one corresponding to a generalized eigenvalue problem, related to the elastic structure, to the acoustic fluid, and to the free surface with appropriate boundary conditions.

2.5.1 Definition of the admissible spaces for the construction of the reduced-order bases

Let $\mathfrak{C}_{P,H,U}$ be the admissible space of the test functions $(\delta\mathbf{P}, \delta\mathbf{H}, \delta\mathbf{U})$ related to the finite element discretization of the fluid-structure interaction problem. The decomposition of this admissible space can be written as the following direct sum (see [81])

$$\mathfrak{C}_{P,H,U} = \mathfrak{C}_P \oplus \mathfrak{C}_H \oplus \mathfrak{C}_U \quad , \tag{2.66}$$

that are illustrated in Figure 2.2, and where the following admissible spaces are defined hereinafter.

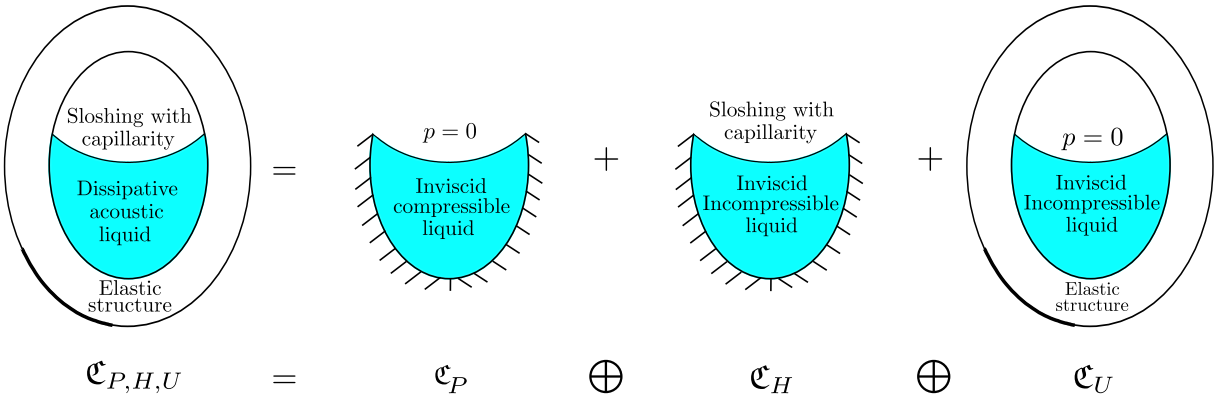

Figure 2.2 – Representation of the decomposition of the admissible space $\mathfrak{C}_{P,H,U}$. (scheme from [85])

- $\mathfrak{C}_P$ denotes the admissible space of test functions $\delta\mathbf{P}$ related to the conservative and homogeneous problem for acoustic pressure $\mathbf{P}$, for which the inviscid compressible liquid occupies domain Ω_p. The associated boundary conditions are $\frac{\partial p}{\partial \mathbf{n}} = 0$ on Σ, corresponding to a fixed-wall condition (*i.e.* $\mathbf{u} = \mathbf{0}$) and a zero pressure condition $p = 0$ on Γ.

- $\mathfrak{C}_H$ denotes the admissible space of test functions denoted by $\delta(\mathbf{H}, \mathbf{P})$ whose notations is described hereinafter. We consider the conservative and homogeneous liquid with acoustic pressure $\mathbf{P}$ associated with a free-surface elevation $\mathbf{H}$, considering sloshing and capillarity effects, with the boundary condition $\frac{\partial p}{\partial \mathbf{n}} = 0$ on Σ (*i.e.* $\mathbf{u} = \mathbf{0}$). the corresponding generalized eigenvalue problem is then formulated as a function of $\mathbf{H}$ and $\mathbf{P}$, which means that for a given $\delta\mathbf{H}$ there is an associated $\delta\mathbf{P}$.

- $\mathfrak{C}_u$ denotes the admissible space of test functions $\delta\mathbf{U}$, that are zero on Σ_0, related to the problem for structural displacement $\mathbf{U}$, taking into account the added-mass effects induced by the coupling of the structure with the liquid that is assumed inviscid and incompressible, and for which the associated boundary condition is a zero pressure $p = 0$ on Γ.

2.5.2 Construction of the mean nonlinear reduced-order computational model

The construction of the global projection basis $[\Psi]$ is divided in three steps, each one being issued from the decomposition of $\mathfrak{C}_{P,H,U}$. Therefore, three vector bases have to be calculated each one being related to a generalized eigenvalue problem.

- A vector basis of $\mathfrak{C}_P$ is constituted of the *acoustic modes* of the internal liquid, which are the eigenvectors of the generalized eigenvalue problem,

$$[K_p]\,[\Phi_p] = [M_p]\,[\Phi_p]\,[\Lambda_p]\,, \tag{2.67}$$

in which the appropriate boundary conditions have to be added. In Eq. (2.67), $[\Phi_p] = [\boldsymbol{\varphi}_p^1, \ldots, \boldsymbol{\varphi}_p^{N_p}]$ is the $(n_p \times N_p)$ real matrix whose N_p columns are constituted of the eigenvectors associated with the N_p first smallest positive eigenvalues sorted by increasing order such that $\lambda_p^1 \leq \ldots \leq \lambda_p^{N_p}$ contained in the diagonal matrix $[\Lambda_p]$. Matrix $[\Phi_p]$ satisfies the following orthogonality properties

$$[\Phi_p]^T\,[M_p]\,[\Phi_p] = [I_{N_p}] \quad \text{and} \quad [\Phi_p]^T\,[K_p]\,[\Phi_p] = [\Lambda_p] \quad , \tag{2.68}$$

in which $[I_{N_p}]$ is the $(N_p \times N_p)$ identity matrix.

- Using the definition of $\mathfrak{C}_H$, a vector basis of $\mathfrak{C}_H$ is constituted of the *sloshing modes* of the liquid in presence of capillarity and of the associated acoustic presure in the liquid, which are the eigenvectors of the generalized eigenvalue problem

$$[K_p]\,[\Phi_{ph}] + [C_{ph}]^T\,[\Phi_h]\,[\Lambda_h] = 0\,, \tag{2.69}$$

$$[C_{ph}]\,[\Phi_{ph}] + [K_{gc}]\,[\Phi_h] = 0\,. \tag{2.70}$$

In Eqs.(2.69) and (2.70), $[\Phi_h] = [\boldsymbol{\varphi}_h^1, \ldots, \boldsymbol{\varphi}_h^{N_h}]$ and $[\Phi_{ph}] = [\boldsymbol{\varphi}_{ph}^1, \ldots, \boldsymbol{\varphi}_{ph}^{N_h}]$ are the $(n_h \times N_h)$ and the $(n_p \times N_h)$ real matrices whose N_h columns are constituted of the eigenvectors associated with the N_h first smallest positive eigenvalues sorted by increasing order such that $\lambda_h^1 \leq \ldots \leq \lambda_h^{N_h}$ contained in the diagonal matrix $[\Lambda_h]$.

- A vector basis of $\mathfrak{C}_U$ is constituted of the *elastic modes* with the added-mass effects of the underlying linear equations for the nonlinear structure, which are the eigenvectors of the generalized eigenvalue problem

$$[K_u]\,[\Phi_u] = (\,[M_u] + [M_a]\,)\,[\Phi_u]\,[\Lambda_u]\,, \tag{2.71}$$

in which the $(n_u \times n_u)$ symmetric positive-definite added-mass matrix $[M_a]$ is defined by

$$[M_a] = [C_{pu}]\,[K_p]^{-1}\,[C_{pu}]^T\,. \tag{2.72}$$

It should be noted that $[K_p]^{-1}$ is a formal notation for denoting the inverse of matrix $[K_p]$ in the subspace $\mathfrak{C}_U$ ensuring the corresponding boundary condition $p = 0$ on the free surface. In Eq. (2.71), $[\Phi_u] = [\boldsymbol{\varphi}_u^1, \ldots, \boldsymbol{\varphi}_u^{N_u}]$ is the $(n_u \times N_u)$ real matrix whose N_u columns are constituted of the eigenvectors associated with the N_u first smallest positive eigenvalues sorted by increasing order such that $\lambda_u^1 \leq \ldots \leq \lambda_u^{N_u}$ contained in the diagonal matrix $[\Lambda_u]$. Matrix $[\Phi_u]$ satisfies the following orthogonatlity properties matrix $[\Phi_u]$ is the matrix of the corresponding eigenvectors that satisfy the following orthogonality properties,

$$[\Phi_u]^T\,([M_u] + [M_a])\,[\Phi_u] = [I_{N_u}] \quad , \tag{2.73}$$

$$[\Phi_u]^T\,[K_u]\,[\Phi_u] = [\Lambda_u] \quad , \tag{2.74}$$

in which $[I_{N_u}]$ is the $(N_u \times N_u)$ identity matrix.

Remark: The matrix $[M_u] + [M_a]$ can be viewed as the Schur complement [61] of the block matrix $[S]$ defined by

$$[S] = \begin{bmatrix} [M_u] & [C_{pu}] \\ -[C_{pu}]^T & [K_p] \end{bmatrix} \quad .$$

The construction of this reduced-order model involves three projection bases, each issued from one of the subsystems of the coupled fluid-structure system. This method not only facilitates the calculation of the projection basis in terms of calculation cost, but also separates the frequency scales of the system. It is well known that the resonance phenomena of each subpart of such a coupled fluid-structure system belong to different frequency ranges. This is why such modeling allows, by avoiding calculating the low-energy modes located in the frequency gaps between each subpart of the system, for choosing the contributions of each part of the system and for correctly involving the most energetic modes in the system dynamics.

The nonlinear reduced-order computational model is constructed by projecting the equations of the fluid-structure system (defined by Eqs. (2.63) to (2.65)) on the reduced-order basis $[\Psi]$ constituted of the vector bases constructed above. The solutions $\mathbf{P}$, $\mathbf{H}$, and $\mathbf{U}$ are then written as

$$\begin{bmatrix} \mathbf{P} \\ \mathbf{H} \\ \mathbf{U} \end{bmatrix} = \begin{bmatrix} [\Phi_p] & [\Phi_{ph}] & 0 \\ 0 & [\Phi_h] & 0 \\ 0 & 0 & [\Phi_u] \end{bmatrix} \begin{bmatrix} \mathbf{Q}^p \\ \mathbf{Q}^h \\ \mathbf{Q}^u \end{bmatrix} = [\Psi]\, \mathbf{Q}\,, \tag{2.75}$$

in which $\mathbf{Q} = (\mathbf{Q}^p, \mathbf{Q}^h, \mathbf{Q}^u)$ is the $\mathbb{R}^{N_{phu}}$-vector of the generalized coordinates, with $N_{phu} = N_p + N_h + N_u$, solution of the coupled nonlinear differential equation

$$[\mathcal{M}_{\rm FSI}]\, \ddot{\mathbf{Q}} + [\mathcal{D}_{\rm FSI}]\, \dot{\mathbf{Q}} + [\mathcal{K}_{\rm FSI}]\, \mathbf{Q} + \boldsymbol{\mathcal{F}}_{\rm NL}(\mathbf{Q}) = \boldsymbol{\mathcal{F}}\,, \tag{2.76}$$

in which the $(N_{phu} \times N_{phu})$ matrices $[\mathcal{M}_{\rm FSI}]$, $[\mathcal{D}_{\rm FSI}]$, $[\mathcal{K}_{\rm FSI}]$, and the $\mathbb{R}^{N_{phu}}$ vector $\boldsymbol{\mathcal{F}}$ are defined by

$$[\mathcal{M}_{\rm FSI}] = [\Psi]^T \begin{bmatrix} [M_p] & -[C_{ph}]^T & -[C_{pu}]^T \\ 0 & 0 & 0 \\ 0 & 0 & [M_u] \end{bmatrix} [\Psi]\,, \tag{2.77}$$

$$[\mathcal{D}_{\rm FSI}] = [\Psi]^T \begin{bmatrix} [D_p] & 0 & 0 \\ 0 & 0 & 0 \\ 0 & 0 & [D_u] \end{bmatrix} [\Psi]\,, \tag{2.78}$$

$$[\mathcal{K}_{\rm FSI}] = [\Psi]^T \begin{bmatrix} [K_p] & 0 & 0 \\ [C_{ph}] & [K_{gc}] & [C_{hu}] \\ [C_{pu}] & [C_{hu}]^T & [K_u] \end{bmatrix} [\Psi]\,, \tag{2.79}$$

$$\boldsymbol{\mathcal{F}} = [\Psi]^T \begin{bmatrix} 0 \\ 0 \\ \mathbf{F}_u \end{bmatrix}\,. \tag{2.80}$$

All the detailed expressions of the reduced-order mass, damping, and stiffness fluid-structure interaction matrices are given in Appendix A. In Eq. (2.76), $\boldsymbol{\mathcal{F}}_{\rm NL}(\mathbf{Q})$ denotes the generalized nonlinear internal forces that are related to the structure. These generalized conservative internal nonlinear forces are written [78] as

$$\{\boldsymbol{\mathcal{F}}_{\rm NL}(\mathbf{Q})\}_\alpha = \mathcal{K}^{(2)}_{\alpha\beta\gamma}\, Q^u_\beta\, Q^u_\gamma + \mathcal{K}^{(3)}_{\alpha\beta\gamma\delta}\, Q^u_\beta\, Q^u_\gamma\, Q^u_\delta \quad , \tag{2.81}$$

where the quadratic and cubic stiffness $\mathcal{K}^{(2)}_{\alpha\beta\gamma}$ and $\mathcal{K}^{(3)}_{\alpha\beta\gamma\delta}$ are such that

$$\mathcal{K}^{(2)}_{\alpha\beta\gamma} = \frac{1}{2}\left(\widehat{\mathcal{K}}^{(2)}_{\alpha\beta\gamma} + \widehat{\mathcal{K}}^{(2)}_{\gamma\alpha\beta} + \widehat{\mathcal{K}}^{(2)}_{\beta\gamma\alpha}\right) \quad , \tag{2.82}$$

$$\widehat{\mathcal{K}}^{(2)}_{\alpha\beta\gamma} = \int_{\Omega_u} C_{ijk\ell}\, \varphi^{\alpha}_{i,j}\, \varphi^{\beta}_{m,k}\, \varphi^{\gamma}_{m,\ell}\, d\mathbf{x} \quad , \tag{2.83}$$

$$\mathcal{K}^{(3)}_{\alpha\beta\gamma\delta} = \frac{1}{2} \int_{\Omega_u} C_{ijk\ell}\, \varphi^{\alpha}_{s,i}\, \varphi^{\beta}_{s,j}\, \varphi^{\gamma}_{m,k}\, \varphi^{\delta}_{m,\ell}\, d\mathbf{x} \quad . \tag{2.84}$$

The details regarding the construction of these nonlinear contributions can be found in [37].

Chapter 3

Numerical implementation of the finite element discretization and validations

Contents

3.1 Numerical implementation of the finite element model

The explicit construction of the matrices introduced in Chapter 2, which are involved in the computational model defined by Eqs. (2.63) to (2.65) is detailed in Appendix B. It should be noted that the 3D finite elements are tetrahedra with 10 nodes, the 2D finite elements are triangles with 6 nodes, and the 1D finite elements are lines with 3 nodes. The number of dofs of the structural displacements is n_u, the number of dofs of the acoustic pressure is n_p, and the number of dofs of the free-surface elevation is n_h. The finite element discretization of matrices introduced in Chapter 2 requires a particular attention and implementation for the construction of coupling matrix $[C_{hu}]$, which is detailed in Section B.3

3.2 Numerical validation of the computational modelling

The developments presented in Appendix B for the finite element discretization of the fluid-structure problem, described by Eqs. (2.23) to (2.25), has to be validated in order to ensure the correct implementation of the fluid-structure matrices. This validation can be performed by comparing the numerical results calculated using the computational model issued from Appendix B (called N-FSI-SC) to reference computations and analytical results. The comparison between the hydroelastic frequencies of a cylinder tank computed with industrial softwares and calculated with N-FSI-SC is performed in order to validate the construction of the matrix $[C_{pu}]$. Analytical calculations allow for validating the construction of matrices $[K_g]$ and $[C_{ph}]$. A manufactured solution method is then implemented in order to validate the implementation of the nonlinear stiffness matrices defined in Section B.4 of the mean nonlinear reduced-order model.

3.2.1 Numerical validation of the hydroelastic coupling

The validation of the hydroelastic coupling in the fluid-structure system is performed through a comparison between N-FSI-SC results and numerical results proposed in [95] which were calculated using 3 softwares: Astral, Nastran, and FSI3D. The coupled fluid-structure system is a fixed-flat base cylindrical tank of internal radius $R = 2\,m$, internal height $h = 2\,m$, and thickness of the shell $e = 0.01\,m$. Its isotropic material properties are: Young modulus $E = 200\,GPa$, mass density $\rho_s = 8000\,Kg.m^{-3}$, and Poisson ratio $\nu = 0.25$. The internal liquid is water with mass density $\rho_f = 1000\,Kg.m^{-3}$. The coupled system is meshed using quadratic interpolation

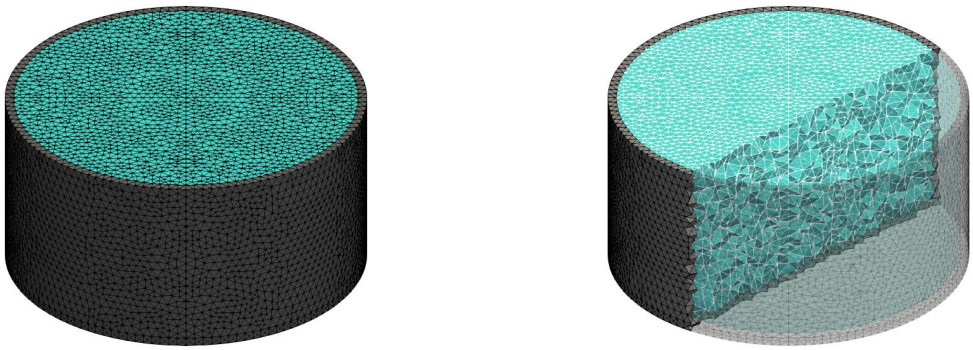

Figure 3.1 – Global (left figure) and detailed (right figure) views of the meshes of the fluid-structure system for the validation of the hydroelastic matrices.

functions for the elements 3D-solid tetrahedral elements of the structure and of the liquid, for the 2D triangles of the free surface of the liquid, and for the 1D elements of the triple line. The characteristics of the tank mesh are given in Table 3.1. The comparison between the analytical

	Nodes	Dof	Elements
Structure	64 424	193 272	32 895
Fluid	149 669	149 669	103 108
Free surface	6 785	6 785	3 328

Table 3.1 – Table of the mesh characteristics for the cylindrical tank.

and the numerical eigenfrequencies of the system is displayed in Table 3.2 for the 12 first hydroelastic eigenfrequencies of the system. Figure 3.2 displays three hydroelastic eigenmodes of the structure and the associated longitudinal and circumferential wave numbers m and n.

The results shown in this comparison propose a good agreement between the eigenfrequencies from N-FSI-SC and the eigenfrequencies from Astral, Nastran, and FSI3D. One can see that the relative deviation increases with the circumferential wave number n (*e.g.* for $n = 6$ and for $n = 7$). This is mostly due to the fact that linear interpolation is used in [95] whereas quadratic interpolation is used in this work, and in addition, the finite element mesh of the system is finer than the one used in [95]. These results validate the implementation of the coupling hydroelastic operator $[C_{pu}]$.

Mode	Astral (Hz)	Nastran (Hz)	FSI3D (Hz)	N-FSI-SC (Hz)	Relative deviation (in %) Astral	Nastran	FSI3D
$m=1$, $n=3$	95.03	94.00	96.19	94.66	0.4	0.7	1.6
$m=1$, $n=4$	103.19	102.43	104.10	100.32	2.8	2.1	3.6
$m=1$, $n=2$	122.80	121.41	124.35	123.02	0.2	1.3	1.1
$m=1$, $n=5$	140.15	140.65	142.20	133.85	4.5	4.8	5.8
$m=1$, $n=1$	184.99	183.08	186.34	184.04	0.5	0.5	1.2
$m=1$, $n=6$	195.22	198.79	198.95	184.80	5.3	7.0	7.1
$m=1$, $n=0$	240.60	238.43	241.35	235.38	2.2	1.3	2.5
$m=2$, $n=4$	266.07	254.06	263.82	258.87	2.7	1.9	1.9
$m=2$, $n=3$	274.32	262.75	275.30	268.00	2.3	1.9	2.7
$m=2$, $n=5$	284.56	269.58	280.29	274.75	3.4	1.9	1.9
$m=1$, $n=7$	264.08	272.92	270.70	248.43	5.9	8.9	8.2
$m=2$, $n=2$	303.26	287.98	306.98	295.56	2.5	2.6	3.7

Table 3.2 – Table of the comparison between the hydroelastic eigenfrequencies computed by Astral, Nastran, FSI3D (from [95]), and N-FSI-SC.

$m=1$, $n=3$ $m=1$, $n=5$ $m=2$, $n=2$

Figure 3.2 – Example of three hydroelastic eigenmodes.

3.2.2 Analytical validation of the sloshing eigenmodes without capillarity

The validation of the sloshing operators $[C_{ph}]$ and $[K_g]$ is performed through a comparison of the sloshing eigenfrequencies (without capillarity). The modal shapes of the sloshing eigenmodes without capillarity and their associated eigenfrequencies can be obtained by numerous software (Astral, Nastran, ...). In our case, in order to validate the implementation of the sloshing matrices $[K_g]$ and $[C_{ph}]$, a comparison is performed between the sloshing frequencies obtained with N-FSI-SC and analytical sloshing eigenfrequencies (proposed in [95]) within the framework of a simple coupled system. This system is a parallelepipedic tank constituted of 5 plates (see Fig. 3.3), fully filled with water, for which the internal dimensions are: height $d = 5\,m$, width $\ell = 7\,m$, length $L = 10\,m$, and thickness of plates $e = 0.25\,m$. The coupled system is meshed with 3D solid tetrahedral elements for the structure and the liquid, 2D triangles for the free surface of the liquid, and 1D elements for the triple line, and using quadratic interpolation functions. Since the sloshing is a surface phenomenon and since the acoustic pressure induced by sloshing eigenmodes satisfies the Airy infinitesimal wave theory (*i.e.* the pressure exponentially decreases with respect to the depth of the liquid), the mesh is refined in the neighboorhood of the free surface. For such a geometry, the analytical sloshing eigenfrequencies are expressed as function of two integers m

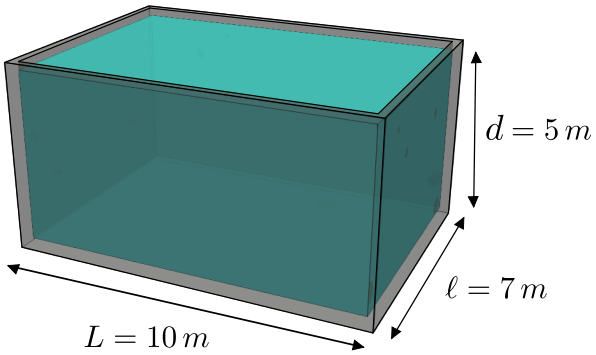

Figure 3.3 – Dimensions of the parallelepipedic tank used for the comparison of sloshing eigenfrequencies computed with N-FSI-SC to analytical sloshing eigenfrequencies.

and n

$$\nu_{m,n} = \frac{\sqrt{g\,k\tanh(k\,d)}}{2\pi} \quad \text{with} \quad k^2 = \pi^2\left(\frac{m^2}{L^2} + \frac{n^2}{\ell^2}\right) \tag{3.1}$$

The characteristics of the parallelepipedic tank mesh are given in Table 3.3. The comparison

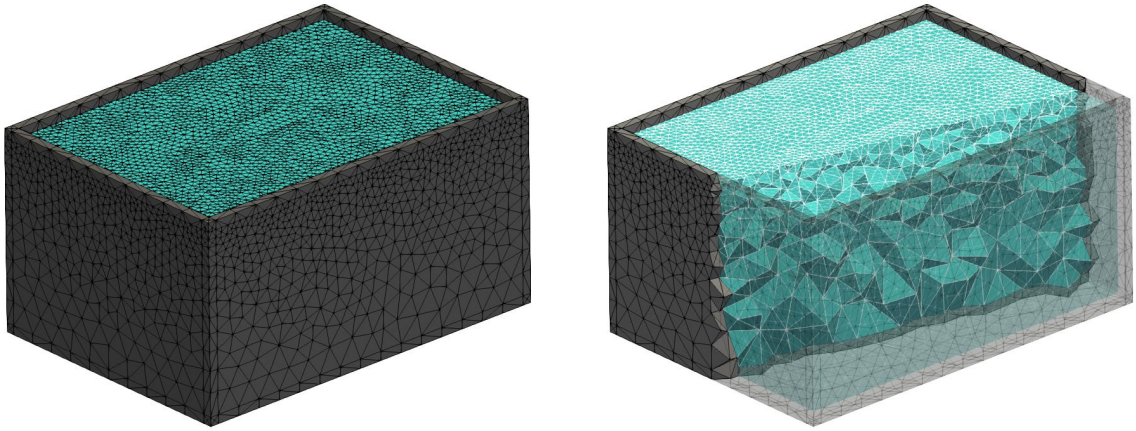

Figure 3.4 – Global (left figure) and detailed (right figure) views of the meshes of the fluid-structure system for the validation of the sloshing matrices.

	Nodes	Dof	Elements
Structure	26 612	79 836	13 694
Fluid	53 551	53 551	34 231
Free surface	9 031	9 031	4 430

Table 3.3 – Table of the mesh characteristics for the parallelepipedic tank.

between the analytical and the numerical eigenfrequencies of the system is shown in Table 3.4

for the 12 first eigenfrequencies of the system. Figure 3.5 displays three sloshing eigenmodes of the free surface and the associated modal pressure in the liquid. One can see that the

Mode	Analytical freq. (Hz)	N-FSI-SC freq. (Hz)	Relative error(%)
$m=1$, $n=0$	0.2676	0.2676	0
$m=0$, $n=1$	0.3302	0.3302	0
$m=1$, $n=1$	0.3674	0.3674	0
$m=2$, $n=0$	0.3944	0.3938	0.15
$m=2$, $n=1$	0.4378	0.4378	0
$m=0$, $n=2$	0.4722	0.4714	0.17
$m=3$, $n=0$	0.4839	0.4839	0
$m=1$, $n=2$	0.4861	0.4861	0
$m=3$, $n=1$	0.5093	0.5093	0
$m=2$, $n=2$	0.5218	0.5218	0
$m=4$, $n=0$	0.5588	0.5587	0.02

Table 3.4 – Table of the comparison between the analytical sloshing eigenfrequencies and N-FSI-SC eigenfrequencies.

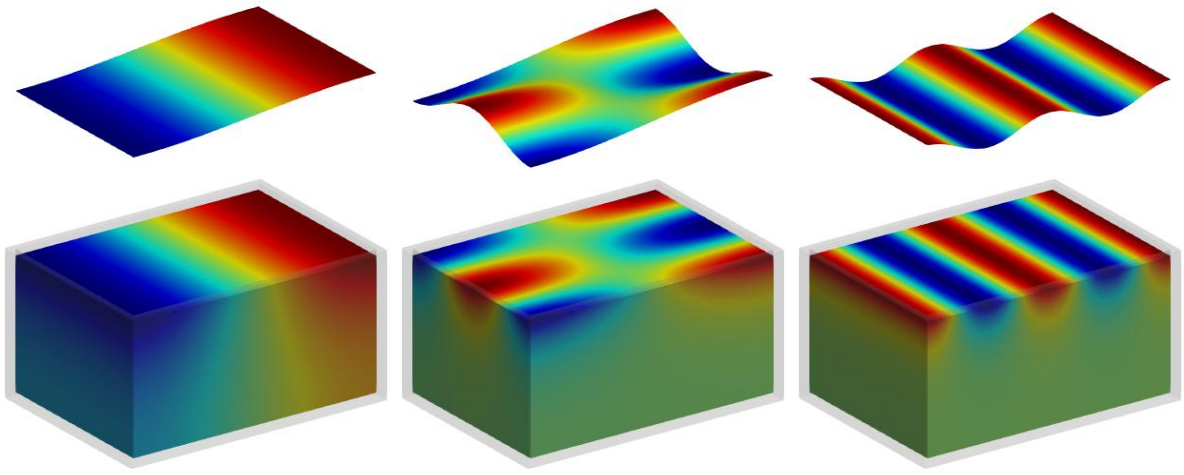

$m=1$, $n=0$ $m=1$, $n=2$ $m=4$, $n=0$

Figure 3.5 – Example of three sloshing eigenmodes with their associated acoustic pressure in the liquid.

computational results are in excellent agreement with the analytical ones since the maximum relative error on the first 12 eigenfrequencies is 0.17%. Such results allows for validating the numerical implementation of the sloshing matrices $[C_{ph}]$ and $[K_g]$.

3.2.3 Validation of the numerical implementation of the nonlinear restoring forces

Concerning the validation of the finite element discretization of the nonlinear restoring forces, induced by the geometrical nonlinearities of the structure, presented in Section B.4, the code verification method proposed in [91] is used. Let us consider a nonlinear static problem of

a structure for which a given compatible displacement field is proposed. The Neumann and Dirichlet boundary conditions can be analytically determined from the continuous equations of the problem. These boundary conditions are then used in a nonlinear static computation and the computed nonlinear static response is then compared to the prescribed displacement.

3.2.3.1 Reference computational model for validating the implementation of the reduced nonlinear restoring forces

A reference full nonlinear problem is designed to validate the implementation of the reduced nonlinear restoring forces. This is why, in this section, we consider a given elastic structure, without any internal liquid, which undergoes large displacements inducing geometrical nonlinearities. In the following, we consider a static problem which can be written as

$$-\operatorname{div}(\underline{\underline{F}}\cdot\underline{\underline{S}}) = \mathbf{b} \quad \text{in } \Omega_u \quad , \tag{3.2}$$

$$\mathbf{u} = \mathbf{0} \quad \text{on } \mathbf{\Sigma_0} \quad , \tag{3.3}$$

$$(\underline{\underline{F}}\cdot\underline{\underline{S}})\cdot\mathbf{n}^u = \mathbf{f} \quad \text{on } \Sigma_E \quad . \tag{3.4}$$

The weak form issued of this boundary value problem consists in finding $\mathbf{u} \in C^0_{\text{ad,u}}$ such that, for all $\delta\mathbf{u} \in C^0_{\text{ad,u}}$ we have

$$\mathbf{f}^{\text{int}}(\mathbf{u},\delta\mathbf{u}) - \mathbf{f}^{\text{ext}}(\delta\mathbf{u}) = \mathbf{0} \quad , \tag{3.5}$$

in which $\mathbf{f}^{\text{int}}(\mathbf{u},\delta\mathbf{u})$ and $\mathbf{f}^{\text{ext}}(\delta\mathbf{u})$ and their finite element discretization are such that

$$\mathbf{f}^{\text{int}}(\mathbf{u},\delta\mathbf{u}) = \int_{\Omega_u} (\underline{\underline{F}}\cdot\underline{\underline{S}}) : \nabla\delta\mathbf{u}\, d\mathbf{x} \Longrightarrow \delta\mathbf{U}^T\,\mathbf{F}^{\text{int}}(\mathbf{U}) \quad , \tag{3.6}$$

$$\mathbf{f}^{\text{ext}}(\delta\mathbf{u}) = \int_{\Omega_u} \mathbf{b}\cdot\delta\mathbf{u}\, d\mathbf{x} + \int_{\Sigma_E} \mathbf{f}\cdot\delta\mathbf{u}\, ds \Longrightarrow \delta\mathbf{U}^T\,\mathbf{F}^{\text{ext}} \quad , \tag{3.7}$$

Let introduce the residue $\mathbf{r}(\mathbf{u},\delta\mathbf{u})$ defined in $C^0_{\text{ad,u}} \times C^0_{\text{ad,u}}$ such that

$$\mathbf{r}(\mathbf{u},\delta\mathbf{u}) = \mathbf{f}^{\text{int}}(\mathbf{u},\delta\mathbf{u}) - \mathbf{f}^{\text{ext}}(\delta\mathbf{u}) \quad . \tag{3.8}$$

The finite element discretization yields

$$\mathbf{r}(\mathbf{u},\delta\mathbf{u}) \Longrightarrow \delta\mathbf{U}^T\,\mathbf{R}(\mathbf{U})\,, \text{ in which } \mathbf{R}(\mathbf{U}) = \mathbf{F}^{\text{int}}(\mathbf{U}) - \mathbf{F}^{\text{ext}} \quad . \tag{3.9}$$

The nonlinear differential equation

$$\mathbf{R}(\mathbf{U}) = \mathbf{0} \quad , \tag{3.10}$$

is solved using a classical iterative Newton-Raphson [45] algorithm, which is assumed to be convergent, such that

$$\mathbf{R}(\mathbf{U}^k + \Delta\mathbf{U}^{k+1}) = \mathbf{R}(\mathbf{U}^k) + [K_T^{(k)}]\Delta\mathbf{U}^{k+1} \quad , \tag{3.11}$$

in which k denotes the current iteration,

$$\mathbf{U}^{k+1} = \mathbf{U}^k + \Delta\mathbf{U}^{k+1} \quad , \tag{3.12}$$

denotes the displacement correction for the current iteration, and

$$[K_T^{(k)}]_{ij} = \left.\frac{\partial R_i(\mathbf{U})}{\partial U_j}\right|_{\mathbf{U}=\mathbf{U}^k} \tag{3.13}$$

is the tangent stiffness matrix evaluated at equilibrium point $\mathbf{U}^k$. The correction $\Delta\mathbf{U}^{k+1}$ is then calculated by solving the linear matrix equation

$$\mathbf{R}(\mathbf{U}^k) + [K_T^{(k)}]\,\Delta\mathbf{U}^{k+1} = \mathbf{0} \quad . \tag{3.14}$$

This implementation of the Newton-Raphson method for the nonlinear static problem has to be validated. The manufactured solution method [91], which is a popular method for validating the numerical implementation of such simple nonlinear boundary value problem, consists in

(i) Proposing a *manufactured* solution $\tilde{\mathbf{u}}$, which verifies the boundary value problem defined by Eqs. (3.2) to (3.4).

(ii) Determining the associated Neumann and Dirichlet boundary conditions by analytically solving the continuous equations of the problem.

(iii) Implementing the analytically obtained Neumann and Dirichlet boundary conditions in the computational model and solve the numerical problem defined by Eq. (3.10) for obtaining the reference solution $\mathbf{u}^{\text{ref}}$.

(iv) Comparing the reference solution $\mathbf{u}^{\text{ref}}$ to the manufactured solution $\tilde{\mathbf{u}}$ by evaluating the L^2-error er^{man},

$$er^{\text{man}} = \sqrt{\frac{\displaystyle\int_{\Omega_u} \left\|\tilde{\mathbf{u}} - \mathbf{u}^{\text{ref}}\right\|^2 d\mathbf{x}}{\displaystyle\int_{\Omega_u} \left\|\tilde{\mathbf{u}}\right\|^2 d\mathbf{x}}} \quad , \tag{3.15}$$

with respect to the mesh size.

The considered structure for the manufactured solution method is presented in Figure 3.6 for which the following dimension are taken into account: $\ell = 15\,m$, $L = 15\,m$, and $d = 20\,m$. The isotropic material properties used for these computations are: Young modulus $E = 8 \times 10^{10}\,Pa$, mass density $\rho_S = 2\,700\,Kg.m^{-3}$, and Poisson coefficient $\nu = 0.3$. The finite element mesh of the structure is constituted of 3D solid tetrahedron with quadratic interpolation functions and the caracteristics of the finite element mesh are presented in Table 3.5.

	Nodes	Dof	Elements
Structure	4 938	14 814	2 785

Table 3.5 – Table of the mesh characteristics for the structure used in the manufactured solution method.

The following manufactured solution $\tilde{\mathbf{u}}$ is considered

$$\tilde{\mathbf{u}}(\mathbf{x}) = \begin{bmatrix} \alpha \tanh(\beta\, x_3) \\ \sinh(\dfrac{\beta}{2}\, x_3) \\ \dfrac{\beta}{10}(x_3^2 - \gamma\, x_3) \end{bmatrix} \quad . \tag{3.16}$$

in which $\alpha = 3$, $\beta = 0.1$, and $\gamma = 20$. Introducing the manufactured solution $\tilde{\mathbf{u}}(\mathbf{x})$ in Eqs. (3.2) to (3.4) yields the corresponding Neumann and Dirichlet boundary conditions (*i.e.* the analytical

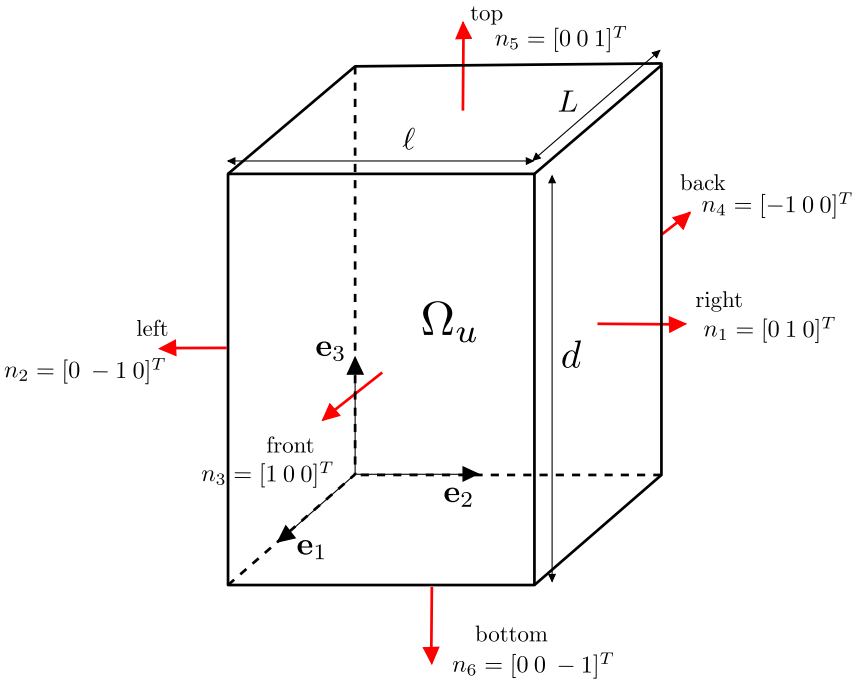

Figure 3.6 – Sketch of the structure considered for the manufactured solution method

expressions of $\mathbf{f}$ and $\mathbf{b}$) that have to be applied to the system. The finite element solution is then computed by solving the computational problem defined by Eq. (3.10) considering the boundary conditions issued from the manufactured solution. It should be noted that such manufactured solution allows for validating the numerical implementation of the geometrical nonlinearities since it involves all ordered derivatives in the error expansion and all terms, *e.g.*, cross-derivatives terms. The convergence analysis of the L^2-error, defined by Eq. (3.15) with respect to the finite element mesh size is presented in Figure 3.7. The results show that the L^2-error between the finite

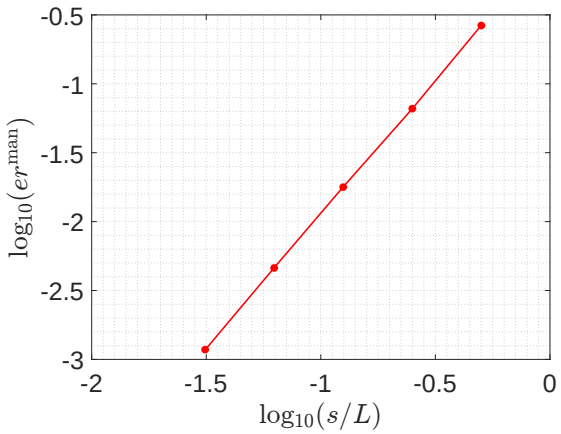

Figure 3.7 – Graph of $\log_{10}(s/L) \mapsto \log_{10}(er^{man})$ displaying the L^2-error evaluated between the manufactured solution and the finite element solution with respect to the mesh fineness s/L.

element solution and the manufactured solution decreases with respect to the mesh fineness. Such results validate the implementation. This manufactured solution method allowed for validating

the implementation of the geometrical nonlinearities for the full model (*i.e.* without using a ROM). This reference calculation is now used in order to validate the implementation of the reduced nonlinear restoring forces proposed in Section B.4.

3.2.3.2 Validating the implementation of the reduced-order geometrical nonlinearities

The static nonlinear elasticity problem for the structure presented in Section 3.2.3.1 is reused in the following. The numerical discretization of the reduced nonlinear restoring forces presented in Section B.4 is validated in this section by comparing the solution $\mathbf{u}^{\text{rom}}(\mathbf{x})$ computed using the reduced-order static nonlinear problem (called ROM$^{\text{stat}}$), to the reference solution $\mathbf{u}^{\text{ref}}(\mathbf{x})$ computed following the methodology described in Section 3.2.3.1. It should be noted that, in this section, since we consider a static equilibrium problem (Eqs. (3.2) to (3.4)), the associated projection basis for the construction of the adapted nonlinear ROM$^{\text{stat}}$ is a static projection basis $[\Phi_u^{\text{stat}}]$, of dimension N_u^{stat}, computed by solving the generalized eigenvalue problem

$$[K_u]\,[\Phi_u^{\text{stat}}] = [\Lambda_u^{\text{stat}}]\,[\Phi_u^{\text{stat}}] \quad , \tag{3.17}$$

The analysis on the L^2-error

$$er^{\text{rom}} = \sqrt{\frac{\displaystyle\int_{\Omega_u} \left\|\mathbf{u}^{\text{ref}} - \mathbf{u}^{\text{rom}}\right\|^2 d\mathbf{x}}{\displaystyle\int_{\Omega_u} \left\|\mathbf{u}^{\text{ref}}\right\|^2 d\mathbf{x}}} \quad , \tag{3.18}$$

is performed with respect to the order of truncation N_u^{stat} of the ROM$^{\text{stat}}$. The structure displayed in Figure 3.6 is tested for two external loads, a traction load and a shear load. The convergence analysis of the error er^{rom} for the two load cases are presented in Figure 3.8. One can see that the reduced-order solution converges to the reference solution with respect to N_u^{stat}. These results allow for validating the implementation of the reduced nonlinear restoring forces proposed in Section B.4.

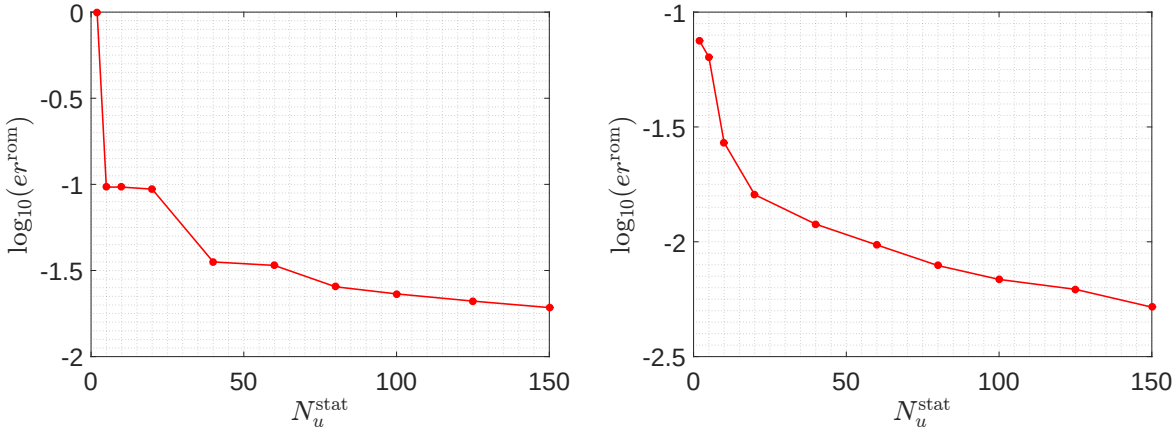

Figure 3.8 – Graph of $N_u^{\text{stat}} \mapsto \log_{10}(er^{\text{rom}})$ displaying the L^2-error between the reference solution and the reduced-order solution with respect to the size of the reduced-order basis N_u^{stat}, for the traction external load case (left figure), and for the shear external load case (right figure).

Chapter 4

Computational strategy for large-scale fluid-structure numerical models

Contents

4.1 Introduction

The algorithms for solving eigenvalue problems (including generalized eigenvalue problems for which one matrix is positive definite) have received a very great attention this last 40 years from a mathematical point of view (see for instance, [104, 70, 88, 25, 94, 61, 39, 26, 66]), for algorithms adapted to parallel computation (see for instance, [33, 65, 49, 62, 50, 106, 112, 15, 48]), and also for massively parallel computers (see for instance, [110, 67, 63, 92, 64]). The majority of the efficient algorithms have been implemented in a mathematical library for computers, parallel computers, and massively parallel computers (see for instance, [42, 22, 23]).

This chapter is devoted to the computation of the generalized eigenvalue problems, presented in Sec. 2.5, which involve very populated sparse matrices in the case of large-scale fluid-structure models. Concerning the algorithms for solving these generalized eigenvalue problems for which one of the two matrices is a positive-definite matrix, the mathematical libraries cited before could, *a priori*, be used (these algorithms are really efficient and are adapted to large scale models using parallel and massively parallel computers). Although these algorithms are efficient on *mid-power computers* that we define as workstations with, for instance, 264 GB to 1 TB for the RAM and 12 to 72 cores for the processors, we have encountered huge difficulties due to the limitation of RAM and also to CPU-time consumption.

The difficulties encountered in the computation depend on the type of modes that have to be computed. Concerning the computation of the elastic structural modes, the mass matrix of the generalized eigenvalue problem is made up of the sparse mass matrix of the structure in which is added the added-mass matrix of the internal liquid (the added-mass matrix is a full matrix with respect to the fluid-structure coupling dofs). Due to a RAM consumption problem, the computation of the added-mass matrix cannot be done as soon as the acoustic-stiffness matrix of the internal liquid is very populated. In addition, assuming that the added-mass matrix has been computed, if the stiffness matrix of the structure is also very populated, another difficulty arises for solving the generalized eigenvalue problem inducing the same type of RAM consumption. The difficulties are exactly of the same nature for the computation of the sloshing/capillarity modes. Concerning the computation of the acoustic modes of the internal liquid, the difficulties are due to the generalized eigenvalue problem that involves two very populated sparse matrices, the acoustic mass and the acoustic stiffness matrices. Confronted with this situation, we have thus revisited the formulations in order to be able to solve the three generalized eigenvalue problems on a mid-power computer. It should be noted that the formulations/algorithms proposed allow for computing a large scale fluid-structure computational model on mid-power computers but certainly, would allow for computing very large scale fluid-structure computational models on high-power computers.

The finite element meshes of the fluid-structure system that will be considered in Section 4.5 have a large number of dofs and a high connectivity, inducing very populated sparse matrices and consequently, leading us to an impossibility to construct the matrices and to compute the generalized eigenvalue problems on mid-power computers using the most adapted algorithms available in the mathematical libraries such as those proposed in Matlab. Concerning the choice of the formulation, two possibilities can be envisaged. For computing the structural elastic modes with the added-mass effects or for computing the sloshing modes with capillarity effects, a first formulation could be based on the use of iterative algorithm for solving linear matrix equation (relative to all the physical dofs) for a very populated matrix and for a large number of right-hand

side members. A second formulation would avoid to solve such a linear systems of equations in high dimension by using a double projection method, also known as the Rayleigh-Ritz method in the framework of eigenvalue problems. An analysis of the advantages/disadvantages of these two formulations has been performed in order to choose the most efficient one. This analysis is summarized in Section 4.3.3 and allows for concluding that the double projection method is more efficient and consequently, will be retained in this paper. This approach allows for decreasing the CPU time and for reducing the RAM avoiding the out of memory and consequently, allowing the computation to be effectively performed. For solving the acoustic generalized eigenvalue problem, the main difficulty is induced by the RAM problem for which an out of memory is obtained. For circumventing this difficulty, we have implemented the subspace iteration method, first introduced in [25, 26], and which is particularly efficient for the problem that has to be solved. Such an approach increases the CPU time but it is the only solution that we have found for avoiding the out of memory. This chapter largely reuses the developments presented in [8, 5] for which the notations have been adapted.

4.2 Summary of the classical formulation of the generalized eigenvalue problems

The algorithms used for solving the generalized eigenvalue problems presented in Section 2.5 are presented in the following. In order to assure the readability of the proposed methodology, this approach, and the consequent numerical algorithms used to solve them, will be defined as the *classical* formulation. The projection vector bases calculated using this classical formulation will be denoted in this chapter by superscript "ref" in order to be able to compare them with the calculations issued from the proposed new methodology.

4.2.1 Generalized eigenvalue problem for the structure

In the framework of the considered fluid-structure computational model, the $N_u \ll n_u$ elastic modes of the structure with added-mass effect of the fluid, which have to be calculated, require to solve the following generalized eigenvalue problem,

$$[K_u]\,[\Phi_u^{\text{ref}}] = (\,[M_u] + [M_a]\,)\,[\Phi_u^{\text{ref}}]\,[\Lambda_u^{\text{ref}}]\,, \tag{4.1}$$

in which we recall that the fluid added-mass matrix $[M_a]$, that characterizes the quasi-static effect of the acoustic fluid on the structure [81, 85], is an $(n_u \times n_u)$ positive-definite symmetric matrix that is formally written as,

$$[M_a] = [C_{pu}]\,[K_p]^{-1}\,[C_{pu}]^T \quad , \tag{4.2}$$

in which we recall that $[K_p]^{-1}$ is a formal notation for denoting the inverse of matrix $[K_p]$ ensuring the boundary condition $p = 0$ for the dofs related to the free surface. The numerical algorithm used for computing matrix $[M_a]$ is a classical backsubstitution for calculating the $(n_p \times n_u)$ matrix $[X]$ as

$$[K_p]\,[X] = [C_{pu}]^T \quad , \tag{4.3}$$

with the corresponding boundary conditions, and for which the minimum degree algorithm (for minimizing the non-zeros elements in the sparse Cholesky factorization of $[K_p]$) is used. The computation of matrix $[X]$ can be very expensive for large-scale fluid-structure model (*i.e.* when the sparsity of matrix $[K_p]$ is weak) even with the use of minimum degree algorithm. The method

proposed in Section 4.4 will allow for avoiding the computational difficulties related to the RAM consumption induced by the use of the classical algorithms for computing a Schur complement. It should also be noted that such method would be very efficient for a hydroelastic problem related to an incompressible liquid in presence of a free surface on which there is a zero pressure condition.

4.2.2 Generalized eigenvalue problem for the acoustic fluid

The $N_p \ll n_p$ acoustic modes of the acoustic fluid, which have to be computed, are obtained by solving the following generalized eigenvalue problem by ensuring the corresponding boundary conditions in $\mathfrak{C}_p$ (that is to say with $p = 0$ for the degrees of freedom related to Γ),

$$[K_p]\,[\Phi_p^{\text{ref}}] = [M_p]\,[\Phi_p^{\text{ref}}]\,[\Lambda_p^{\text{ref}}] \quad . \tag{4.4}$$

The computation of the acoustic vector basis $[\Phi_p^{\text{ref}}]$ can be very expensive for a high number of degrees of freedom in the internal liquid mesh due to the classical algorithm used for solving the generalized eigenvalue problems presented in Section 4.3.

4.2.3 Generalized eigenvalue problem for the sloshing with capillarity

The computation of the $N_h \ll n_h$ sloshing/capillarity modes consists in finding the eigenvalues represented by the $(N_h \times N_h)$ diagonal matrix $[\Lambda_h^{\text{ref}}]$ and the associated eigenvectors represented by the $((n_h + n_p) \times N_h)$ matrix $[\Psi_h^{\text{ref}}]$ that is written by blocks as

$$[\Psi_h^{\text{ref}}] = \begin{bmatrix} [\Phi_h^{\text{ref}}] \\ [\Phi_{ph}^{\text{ref}}] \end{bmatrix} , \tag{4.5}$$

in which $[\Phi_h^{\text{ref}}]$ is a $(n_h \times N_h)$ matrix and $[\Phi_{ph}^{\text{ref}}]$ is a $(n_p \times N_h)$ matrix, such that

$$[K_p]\,[\Phi_{ph}^{\text{ref}}] + [C_{ph}]^T\,[\Phi_h^{\text{ref}}]\,[\Lambda_h^{\text{ref}}] = 0\,, \tag{4.6}$$

$$[C_{ph}]\,[\Phi_{ph}^{\text{ref}}] + [K_{gc}]\,[\Phi_h^{\text{ref}}] = 0\,, \tag{4.7}$$

that has to be solved with a constant pressure condition on the free surface of the acoustic fluid. Eliminating $[\Phi_{ph}^{\text{ref}}]$ in Eqs. (4.6) and (4.7) by ensuring the constant pressure condition on the free surface, is equivalent to solving the following generalized eigenvalue problem,

$$[K_{gc}]\,[\Phi_h^{\text{ref}}] = [M_{gc}]\,[\Phi_h^{\text{ref}}]\,[\Lambda_h^{\text{ref}}]\,, \tag{4.8}$$

in which $[M_{gc}]$ is a positive-definite $(n_h \times n_h)$ matrix that is formally written as $[M_{gc}] = [C_{ph}]\,[K_p]^{-1}\,[C_{ph}]^T$ because $[K_p]$ is not invertible, and which is rewritten as $[M_{gc}] = [C_{ph}]\,[S]$ where the $(n_p \times n_h)$ matrix $[S]$ is computed by solving the linear matrix equation

$$\begin{bmatrix} [K_p] & \boldsymbol{\zeta}^T \\ \boldsymbol{\zeta} & 0 \end{bmatrix} \begin{bmatrix} [S] \\ [L] \end{bmatrix} = \begin{bmatrix} [C_{ph}]^T \\ 0 \end{bmatrix} , \tag{4.9}$$

in which $[L]$ is the $(1 \times n_h)$ matrix of the Lagrange multipliers. In Eq. 4.9, $\boldsymbol{\zeta}$ is a $(1 \times n_h)$ vector with all the entries equal to 1. The orthogonality properties related to the generalized eigenvalue problem defined by Eq. (4.8) are written as

$$[\Phi_h^{\text{ref}}]^T\,[M_{gc}]\,[\Phi_h^{\text{ref}}] = [I_{N_h}]\,, \tag{4.10}$$

$$[\Phi_h^{\text{ref}}]^T\,[K_{gc}]\,[\Phi_h^{\text{ref}}] = [\Lambda_h^{\text{ref}}]\,. \tag{4.11}$$

Once Eq. (4.8) is solved and therefore, matrix $[\Phi_h^{\text{ref}}]$ is known, matrix $[\Phi_{ph}^{\text{ref}}]$ is computed by

$$[\Phi_{ph}^{\text{ref}}] = -[S]\,[\Phi_h^{\text{ref}}]\,[\Lambda_h^{\text{ref}}] \quad . \tag{4.12}$$

4.3 Computational limitations induced by the classical formulation

This section presents the different computational limitations encountered when trying to compute the different vector bases $[\Phi_u^{\text{ref}}]$, $[\Phi_p^{\text{ref}}]$, and $[\Psi_h^{\text{ref}}]$ using the classical formulation.

4.3.1 Brief description of the algorithms required for solving the generalized eigenvalue problems of the introduced formulation

The formulation that has been presented in Section 4.2 requires to use an algorithm for solving a given linear matrix equation for a positive-definite matrix and an algorithm for solving a generalized eigenvalue problem for two real symmetric matrices for which one is positive definite.

- The first classical algorithm (ALG1) is used for solving a linear matrix equation of the type $[A]\,[X] = [B]$ in which $[A]$ is a symmetric positive-definite matrix (see, for instance, Eq. (4.3)). Such a classical algorithm consists in computing the Cholesky factorization $[C]\,[C]^T$ of $[A]$ using a minimum degree algorithm for optimizing the sparsity of $[C]$. Then the solution of the linear matrix equation is obtained using the standard successive back-substitutions that is formally written as $[X] = [C^{-T}](\,[C]^{-1}\,[B])$.

- The second classical algorithm (ALG2) is used for computing the N first smallest eigenvalues and their associated eigenvectors of the generalized eigenvalue problem of the type $[A]\,[X] = [B]\,[X]\,[\Lambda]$ in which $[A]$ and $[B]$ are two symmetric positive-definite matrices (see, for instance, Eq. (4.4)). The classical algorithm for solving such a generalized eigenvalue problem consists in transforming it into a classical eigenvalue problem $[P]\,[Y] = [Y]\,[\Lambda]$. For that, algorithm ALG1 is used for computing $[P]$. This type of algorithm is used by Matlab that calls the standard library LAPACK [22, 61].

It should be noted that the computational difficulties related to the RAM consumption are generally not due to the eigenvalue problem $[P]\,[Y] = [Y]\,[\Lambda]$ but are due to the use of ALG1 by ALG2.

4.3.2 Limitations related to RAM consumption for large-scale numerical models on mid-power computers

As explained in Section 4.2.1, the difficulties occur with ALG1 when sparse matrices $[M_p]$ and $[K_p]$ are very populated. This is the case, for instance, for a medium-scaled fluid-structure computational model for which 20-node 3D solid hexahedral finite elements are used for the structure and the internal liquid. These difficulties are induced by the use of ALG1 in the following numerical steps.

Remark: Note that the 20-nodes 3D solid hexahedral finite elements are also constructed using quadratic interpolation functions. Historically, in this work, the calculations have beenn started using this type of finite elements but it appeared, after, that 10-nodes 3D solid tetrahedral finite elements were more appropriate for meshing the domains.

- The elastic eigenvalue problem defined in Section 4.2.1 requires to compute matrix $[M_a]$ (see Eq. (4.2)) solving the matrix equation defined by Eq. (4.3) using ALG1 involving matrix $[K_p]$. The memory overconsumption is mainly due to the number of columns in matrix $[C_{pu}]^T$.

- The acoustic eigenvalue problem defined in Section 4.2.2 requires to solve the generalized eigenvalue problem defined by Eq. (4.4) using ALG2 that uses ALG1 involving matrix $[M_p]$. The memory overconsumption is mainly due to the computation of the Cholesky factorization of matrix $[M_p]$.
- Finally, the sloshing/capillarity eigenvalue problem is obtained by solving the linear matrix equation defined by Eq. (4.9) using ALG1 and then solving the generalized eigenvalue problem defined by Eq. (4.8) with ALG2 involving matrix $[K_p]$. The memory overconsumption is mainly due to the number of columns in matrix $[C_{ph}]^T$.

4.3.3 Remark concerning the choice of a formulation

In this section, we analyze the CPU time induced by an iterative algorithm with respect to ALG1. For solving Eq. (4.3) in which $[K_p]$ is a very populated sparse matrix and where the number of active columns in the right-hand side member is large, an iterative solver could be used (the problem is similar for Eq. (4.9)). As $[K_p]$ is positive, the preconditioned conjugate gradient iterative algorithm, denoted as "PCG", is used for computing matrix $[X]$. This iterative algorithm is known for being very efficient when solving $[A]\,\mathbf{X} = \mathbf{B}$ in which $[A]$ is a symmetric positive-definite matrix. Such an algorithm requires that the right-hand side member $\mathbf{B}$ be a vector (and not a matrix), which is not the case for the problem that we have to solve. This is why, the use of such an iterative algorithm is not, *a priori*, the best choice for the computation of matrix $[X]$, because the PCG algorithm should be used for each column of matrix $[C_{pu}]^T$. The PCG algorithm requires the use of a preconditioner to speed up the convergence, which is chosen as the incomplete Cholesky factorization of matrix $[K_p]$. This incomplete Cholesky factorization requires a filling parameter named as "drop tolerance" that has to be optimized for the PCG algorithm. This drop tolerance optimization must take into account the time required to compute the incomplete Cholesky factorization of $[K_p]$ and also the time required to solve the linear system with this preconditioner. The analysis of the CPU-time consumption

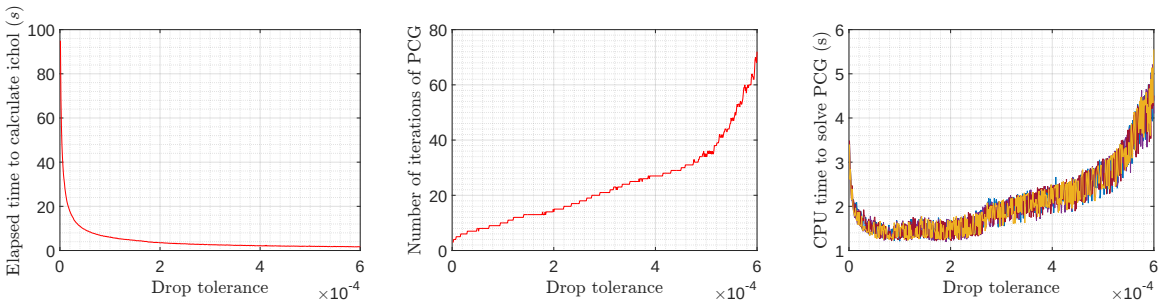

Figure 4.1 – Analysis of the PCG algorithm for solving the linear matrix equation defined by Eq. (4.3) with respect to the Drop tolerance of the Cholesky factorization of matrix $[K_p]$: Elapsed time required for computing the incomplete Cholesky factorization of matrix $[K_p]$ (left figure); Number of iteration required for solving Eq. (4.3) (middle figure) for only one right hand-side member (*i.e.* for one column of matrix $[C_{pu}]^T$); CPU time required for solving Eq. (4.3) using PCG algorithm for 10 right-hand side members (*i.e.* for the 10 first columns of matrix $[C_{pu}]^T$) (right figure).

for such iterative solver has been performed on the smallest mesh of the application presented in Section 4.5. The detailed results of this analysis are shown in Figure 4.1. Figure 4.1 (left) displays the graph of the elapsed time required for computing the PCG preconditionner using

the incomplete Cholesky factorization of $[K_p]$ with respect to the drop tolerance. It is shown that the time required for computing this preconditionner is negligeable in front of the total elapsed time required in the use of the PCG. Figure 4.1 (middle) displays the graph of the number of iterations required to solve the linear matrix equation $[K_p]\,\mathbf{X}_1 = [C_{pu}]_1^T$ (in which $[C_{pu}]_1^T$ denotes the first column of matrix $[C_{pu}]^T$) with respect to the drop tolerance. Finally, figure 4.1 (right) displays the graph of the CPU time required for solving the 10 firsts linear matrix equations defined by $[K_p]\,\mathbf{X}_i = [C_{pu}]_i^T$ $(i = 1, \ldots, 10)$ with respect to the drop tolerance. One can see that the same trend is visible for the 10 computations and that the value of the optimal drop tolerance is 1.8×10^{-4}. Table 4.1 synthesizes both the CPU time and the elapsed time required to compute Eq. (4.2) using either ALG1 or PCG algorithms. One can see that the time required by the PCG alogrithm is almost two times greater than the time for ALG1. The results show that

Algorithm	CPU time	Elapsed time
ALG1	8 h 54 min	57 min
PCG	57 h 09 min	30 h 06 min

Table 4.1 – Table of the CPU time and the corresponding elapsed time required for solving Eq. (4.3) using ALG1 and PCG algorithm.

the PCG algorithm is a lot slower than ALG1 in this case. This difference between ALG1 and PCG can be explained by the loop required to solve the linear system for each column of matrix $[C_{pu}]^T$, which is heavily time consuming on a software such as Matlab. For solving the linear matrix equation, Eq. (4.3), with the PCG algorithm, the loop could be parallelized to speed up the computation but would highly increase the RAM consumption. Finally, it is concluded that PCG will not be retained.

4.4 Adapted computational strategy for solving the generalized eigenvalue problems

Taking into account the limitations highlighted in Section 4.3, an alternative numerical strategy is proposed, allowing the elastic, acoustic, and sloshing/capillarity eigenvalue problems, to be solved for large scale fluid-structure computational models on mid-power computers with a moderate RAM.

4.4.1 Double projection algorithm for solving the elastic eigenvalue problem

The proposed double projection method allows for circumventing the difficulties induced by the computation of matrix $[M_a]$. It consists in introducing a second projection for solving the generalized eigenvalue problem defined by Eq. (4.1). The modal matrix $[\Phi_u]$ is then rewritten as,

$$[\Phi_u] = [\Phi_u^{\mathrm{I}}]\,[\Phi_u^{\mathrm{II}}] \quad , \tag{4.13}$$

in which $[\Phi_u^{\mathrm{I}}]$ is the full $(n_u \times \mathcal{N}_u)$ matrix that corresponds to the first projection basis on a subspace of dimension $\mathcal{N}_u > N_u$, and where $[\Phi_u^{\mathrm{II}}]$ is the full $(\mathcal{N}_u \times N_u)$ matrix that corresponds to the second projection basis on a subspace of dimension N_u. In the present case, the first projection basis is constructed by solving the following eigenvalue problem for the structure in vacuo (without the acoustic fluid),

$$[K_u]\,[\Phi_u^{\mathrm{I}}] = [M_u]\,[\Phi_u^{\mathrm{I}}]\,[\Lambda_u^{\mathrm{I}}]\,. \tag{4.14}$$

If $\mathcal{N}_u$ is sufficiently large, the N_u eigenvectors computed using Eq. (4.1) belong to the subspace spanned by $[\Phi_u^{\mathrm{I}}]$. Note that for $\mathcal{N}_u = n_u$, $[\Phi_u^{\mathrm{I}}]$ is a vector basis of the admissible set and consequently, $\mathcal{N}_u$ can always be found for obtaining the convergence. Therefore the double projection method requires a convergence analysis with respect to $\mathcal{N}_u$. Matrix $[\Phi_u^{\mathrm{I}}]$ satisfies the following orthogonality properties,

$$[\Phi_u^{\mathrm{I}}]^T\,[M_u]\,[\Phi_u^{\mathrm{I}}] = [I_{\mathcal{N}_u}] \quad , \tag{4.15}$$

$$[\Phi_u^{\mathrm{I}}]^T\,[K_u]\,[\Phi_u^{\mathrm{I}}] = [\Lambda_u^{\mathrm{I}}] \quad . \tag{4.16}$$

Left multiplying Eq. (4.1) by $[\Phi_u^{\mathrm{I}}]^T$ and using Eq. (4.13) yield the following generalized eigenvalue problem with a very small dimension $\mathcal{N}_u$ (computationally solved without any problem),

$$[\Lambda_u^{\mathrm{I}}]\,[\Phi_u^{\mathrm{II}}] = \big([I_{\mathcal{N}_u}] + [\mathcal{M}_a]\big)\,[\Phi_u^{\mathrm{II}}]\,[\Lambda_u] \quad , \tag{4.17}$$

for which the following orthogonality conditions are satisfied,

$$[\Phi_u^{\mathrm{II}}]^T([I_{\mathcal{N}_u}] + [\mathcal{M}_a])\,[\Phi_u^{\mathrm{II}}] = [I_{N_u}] \quad , \tag{4.18}$$

$$[\Phi_u^{\mathrm{II}}]^T\,[\Lambda_u^{\mathrm{I}}]\,[\Phi_u^{\mathrm{II}}] = [\Lambda_u] \quad . \tag{4.19}$$

In Eq. (4.17), the $(\mathcal{N}_u \times \mathcal{N}_u)$ positive-definite matrix $[\mathcal{M}_a]$ is written as $[\mathcal{M}_a] = [\Phi_u^{\mathrm{I}}]^T\,[M_a][\Phi_u^{\mathrm{I}}]$. Using Eq. (4.2), this matrix can be rewritten as

$$[\mathcal{M}_a] = [\mathcal{C}_{pu}]\,[K_p]^{-1}\,[\mathcal{C}_{pu}]^T\,, \tag{4.20}$$

in which $[\mathcal{C}_{pu}] = [\Phi_u^{\mathrm{I}}]^T\,[C_{pu}]$ is a $(\mathcal{N}_u \times n_p)$ sparse rectangular matrix. In practice, matrix $[\mathcal{M}_a]$ is computed by $[\mathcal{M}_a] = [\mathcal{C}_{pu}]\,[\mathcal{X}]$ in which the $(n_p \times \mathcal{N}_u)$ matrix $[\mathcal{X}]$ is the solution of the linear matrix equation $[K_p]\,[\mathcal{X}] = [\mathcal{C}_{pu}]^T$ that is solved with ALG1. Such calculations can now be done with a reasonable computational time and RAM consumption.

4.4.2 Subspace iterations for the acoustic eigenvalue problem

For solving the acoustic eigenvalue problem, a method for circumventing the difficulties appearing in ALG2 when using ALG1 that involves matrix $[M_p]$ consists in using the subspace iteration method [25, 26], which is briefly summarized and adapted to our context.

First, an initial projection basis, represented by the $(n_p \times \mathcal{N}_p)$ matrix $[\Phi_p]_1$ with $N_p < \mathcal{N}_p \ll n_p$, is computed using the initialization procedure described in [26]. Then the projection basis is updated using the following iterative algorithm in which the subscript $k \in \{1, 2, \ldots\}$ denotes the current iteration,

$$[K_p]\,[\Phi_p^{\mathrm{I}}]_{k+1} = [M_p]\,[\Phi_p]_k\,, \tag{4.21}$$

$$[K_p]^{k+1} = [\Phi_p^{\mathrm{I}}]_{k+1}^T\,[K_p]\,[\Phi_p^{\mathrm{I}}]_{k+1}\,, \tag{4.22}$$

$$[M_p]^{k+1} = [\Phi_p^{\mathrm{I}}]_{k+1}^T\,[M_p]\,[\Phi_p^{\mathrm{I}}]_{k+1}\,, \tag{4.23}$$

$$[K_p]^{k+1}\,[\Phi_p^{\mathrm{II}}]_{k+1} = [M_p]^{k+1}\,[\Phi_p^{\mathrm{II}}]_{k+1}\,[\Lambda_p]^{k+1}\,, \tag{4.24}$$

$$[\Phi_p]_{k+1} = [\Phi_p^{\mathrm{I}}]_{k+1}\,[\Phi_p^{\mathrm{II}}]_{k+1}\,. \tag{4.25}$$

This iterative procedure is stopped when the following convergence criterion is reached,

$$\left\{1 - \frac{(\lambda_i^{(k+1)})^2}{(\boldsymbol{\varphi}_p^{\mathrm{II},\alpha})_{k+1}^T\,(\boldsymbol{\varphi}_p^{\mathrm{II},\alpha})_{k+1}}\right\}^{\frac{1}{2}} \leq \mathrm{tol} \quad , \quad \mathrm{i} = 1, \ldots, \mathcal{N}_{\mathrm{p}} \quad , \tag{4.26}$$

where $(\boldsymbol{\varphi}_p^{\mathrm{II},\alpha})_{k+1}$ is the α-th vector in matrix $[\Phi_p^{\mathrm{II}}]_{k+1}$ corresponding to $\lambda_i^{(k+1)}$, and tol $= 10^{-2s}$ with accuracy of $2s$ digits in the required eigenvalues. Finally, a Sturm sequence checking is performed to ensure that the correct eigenvalues and their associated eigenvectors have been calculated. This classical iterative procedure could certainly be sped up using the method recently proposed in [68]. It would be an additional improvement of the method proposed for limiting the RAM consumption.

4.4.3 Double projection algorithm for the sloshing/capillarity eigenvalue problem

Again, for avoiding the difficulties induced solving Eq. (4.9), a double projection method similar to the one described in Section 4.4.1 is used for computing the sloshing/capillarity eigenvalue problem defined in Section 4.2.3. However, the first approximation of the projection basis used for the double projection of the elastic eigenmodes of the structure, which consisted in using the dry eigenmodes of the structure, cannot be used for the sloshing eigenmodes. This is why a first approximation of the sloshing projection basis has to be defined in order to apply the double projection method.

4.4.3.1 Comments about the construction of an approximation of matrix $[K_p]$

In order to circumvent the difficulties due to the RAM overconsumption, several possibilities have been explored for constructing a very sparsely populated matrix $[K_p^a]$ that approximates the very populated matrix $[K_p]$.

(i) - A first approximation would consist in using for $[K_p^a]$ the restriction of $[K_p]$ to the pressure dofs related to the free surface of the acoustic liquid (this means that the corresponding rows and columns of $[K_p]$ and the corresponding columns of $[C_{ph}]$ are removed). This approximation leads a very slow convergence of the double projection method.

(ii) - A second one would consist in taking for $[K_p^a]$ a few diagonals of $[K_p]$ in order to take into account that $[K_p]$ corresponds to the finite element approximation of the Laplace operator. This approach is difficult because $[K_p^a]$ must stay nonnegative and in practice, such a property cannot easily be ensured except if an incomplete factorization of $[K_p]$ is performed (see below).

(iii) - A more natural construction of $[K_p^a]$ would consist in computing an incomplete factorization of $[K_p]$. Since this matrix is positive semi-definite (and not positive definite), the incomplete Cholesky factorization of $[K_p]$ cannot be used with the standard libraries such as LAPACK. Therefore, an incomplete LU factorization must be used that avoids the RAM overconsumption but which induces a very high CPU-time consumption.

(iv) - The Airy infinitesimal wave theory shows that the pressure field exponentially decreases as a function of the distance (depth) to the free surface. This means that an approximation $[K_p^a]$ can be constructed by keeping the pressure dofs related to a small layer (with height h_K) of the acoustic liquid under the free surface. Such an approximation is in general, very efficient, and is the one that we propose to use.

4.4.3.2 Double projection algorithm

Let $n_h^a \ll n_p$ be the number of dofs related to the small layer of the acoustic fluid of height h_K under the free surface. Note that we have $n_h < n_h^a$. We then have $[K_p^a]$ and $[C_{ph}^a]$ as the $(n_h^a \times n_{h_K})$ and the $(n_h^a \times n_h^a)$ matrices corresponding to the restriction of matrices $[K_p]$ and $[C_{ph}]$ to the pressure dofs related to this small layer of the acoustic fluid. Consequently, matrix $[K_p]^a$ is positive definite. Let $[\Phi_h^{\rm I}]$ be the $(n_h \times \mathcal{N}_h)$ matrix in which $N_h < \mathcal{N}_h \ll n_h$ and let $[\Lambda_H^{\rm I}]$ be the $(\mathcal{N}_h \times \mathcal{N}_h)$ diagonal positive-definite matrix satisfying the following equation that corresponds to the restriction of Eqs. (4.6) and (4.7) to the n_h^a pressure dofs,

$$[K_p^a]\,[\Phi_{ph}^a] + [C_{ph}^a]^T\,[\Phi_h^{\rm I}]\,[\Lambda_H^{\rm I}] = 0\,, \tag{4.27}$$

$$[C_{ph}^a]\,[\Phi_{ph}^a] + [K_{gc}]\,[\Phi_h^{\rm I}] = 0\,, \tag{4.28}$$

in which $[\Phi_{ph}^a]$ is a $(n_h^a \times \mathcal{N}_h)$ matrix that is the restriction of matrix $[\Phi_{ph}]$ to the n_h^a pressure dofs related to the small layer of acoustic fluid. The elimination of $[\Phi_{ph}^a]$ between Eqs. (4.27) and (4.28) yields the generalized eigenvalue problem,

$$[K_{gc}]\,[\Phi_h^{\rm I}] = [M_{gc}^a]\,[\Phi_h^{\rm I}]\,[\Lambda_H^{\rm I}]\,, \tag{4.29}$$

in which the positive-definite $(n_h \times n_h)$ matrix $[M_{gc}^a]$ is written as,

$$[M_{gc}^a] = [C_{ph}^a]\,[K_p^a]^{-1}\,[C_{ph}^a]^T\,. \tag{4.30}$$

In practice, matrix $[M_{gc}^a]$ is computed by $[M_{gc}^a] = [C_{ph}^a]\,[X]$ in which the $(n_h^a \times n_h)$ matrix $[X]$ is solution of the linear matrix equation $[K_p^a]\,[X] = [C_{ph}^a]^T$ that is solved with ALG1. If $\mathcal{N}_h$ is sufficiently large, the N_h sloshing/capillarity modes defined in Section 4.2.3 belong to the subspace spanned by $[\Phi_h^{\rm I}]$. Note that, for all n_h^a such that $n_h \le n_h^a \le n_p$, if $\mathcal{N}_h = n_h$ then $[\Phi_h^{\rm I}]$ is a vector basis of the admissible set of $\mathbf{H}$ and consequently, $\mathcal{N}_h$ can always be found for obtaining the convergence. Therefore the double projection method requires a convergence analysis with respect to $\mathcal{N}_h$. Matrix $[\Phi_h^{\rm I}]$ verifies the following orthogonality properties,

$$[\Phi_h^{\rm I}]^T\,[M_{gc}^a]\,[\Phi_h^{\rm I}] = [I_{\mathcal{N}_h}]\,, \tag{4.31}$$

$$[\Phi_h^{\rm I}]^T\,[K_{gc}]\,[\Phi_h^{\rm I}] = [\Lambda_h^{\rm I}]\,. \tag{4.32}$$

The solution of Eq. (4.29) provides a reasonable approximation of the sloshing/capillarity modes compared to those computed in Section 4.2.3. The double projection method then consists in writing the block matrix Φ_h appearing in Eq. (4.5) as,

$$[\Phi_h] = [\Phi_h^{\rm I}]\,[\Phi_h^{\rm II}]\,, \tag{4.33}$$

in which the full $(\mathcal{N}_h \times N_h)$ matrix $[\Phi_h^{\rm II}]$ corresponds to the second projection basis on a subspace of dimension $N_h < \mathcal{N}_h$. Substituting Eq. (4.33) in Eq. (4.8) and left multiplying by $[\Phi_h^{\rm I}]^T$ yield the following eigenvalue problem in the subspace with a very small dimension $\mathcal{N}_h$ (computationally solved without any problem),

$$[\Lambda_h^{\rm I}]\,[\Phi_h^{\rm II}] = [\mathcal{M}_{gc}]\,[\Phi_h^{\rm II}]\,[\Lambda_h]\,, \tag{4.34}$$

in which $[\mathcal{M}_{gc}]$ is a positive-definite $(\mathcal{N}_h \times \mathcal{N}_h)$ matrix that is written as $[\mathcal{M}_{gc}] = [\mathcal{C}_{ph}]\,[\mathcal{S}]$, where the $(\mathcal{N}_h \times n_p)$ matrix $[\mathcal{C}_{ph}]$ is defined by $[\mathcal{C}_{ph}] = [\Phi_h^{\rm I}]^T\,[C_{ph}]$, and where matrix $[\mathcal{S}] = [S]\,[\Phi_h^{\rm I}]$ is computed as in Section 4.2.3 by solving the linear matrix equation,

$$\begin{bmatrix} [K_p] & (\boldsymbol{\zeta})^T \\ \boldsymbol{\zeta} & 0 \end{bmatrix} \begin{bmatrix} [\mathcal{S}] \\ [\mathcal{L}] \end{bmatrix} = \begin{bmatrix} [\mathcal{C}_{ph}]^T \\ 0 \end{bmatrix}\,, \tag{4.35}$$

in which $[\mathcal{L}]$ is the $(1 \times \mathcal{N}_h)$ matrix of Lagrange multipliers and where ζ is the matrix introduced in Section 4.2.3. Matrix $[\Phi_h^{\mathrm{II}}]$ satisfies the following orthogonal properties,

$$[\Phi_h^{\mathrm{II}}]^T [\mathcal{M}_{gc}] [\Phi_h^{\mathrm{II}}] = [I_{N_h}] , \tag{4.36}$$

$$[\Phi_h^{\mathrm{II}}]^T [\Lambda_h^{\mathrm{I}}] [\Phi_h^{\mathrm{II}}] = [\Lambda_h] . \tag{4.37}$$

In practice, matrix $[\mathcal{S}]$ is computed by solving the linear matrix equation Eq. (4.35) using ALG1; then the solutions of the sloshing/capillarity eigenvalue problem defined in Eq. (4.34) are computed using ALG2 involving ALG1. Such computation is done with a reasonable time and RAM consumption. We then obtain the block matrix $[\Phi_{ph}]$ of the sloshing/capillarity modes by,

$$[\Phi_{ph}] = -[\mathcal{S}] [\Phi_h^{\mathrm{II}}] [\Lambda_h] . \tag{4.38}$$

4.5 Quantification of the computer resources used for computing the projection bases

In the present numerical study, all the computations are made on a workstation with 264 GB RAM and 12 Intel(R) Xeon(R) CPU E5-2620 0 with a frequency of $2\,GHz$.

4.5.1 Finite element model of the fluid-structure system

The fluid-structure system is the one described in [73, 3] for which the retained dimensions are those of [73] (note that these two references are only used for defining the fluid-structure system for which capillarity effects are not analyzed). The structure is a steel tank constituted of a thin circular cylinder closed at both ends by circular plates (see Figure 4.2). The external radius is $R_e = 3.78 \times 10^{-2}\,m$, the thickness is $e = 2 \times 10^{-4}\,m$, and the height is $h = 0.23\,m$. This tank is partially filled with an acoustic liquid with height $h_f = 0.12\,m$. The origin O of the Cartesian coordinates system $(\mathbf{e}_1, \mathbf{e}_2, \mathbf{e}_3)$ is located at the center of the bottom of the cylindrical tank. Axis $\mathbf{e}_3$ coincides with the axis of revolution of the system. The boundary conditions are those defined in [73, 3]. The finite element model of the fluid-structure system is constructed using 20-node 3D hexahedral finite elements for the structure and for the acoustic fluid. The free surface of the liquid is meshed using 8-node 2D finite elements and the triple line is meshed using 3-node 1D finite elements. All the meshes of the computational model are compatible. On this basis, several finite element meshes with different sizes have been constructed in order to quantify and to identify the limitations of the computer resources used for the computation. Table 4.2 summarizes the finite element models built in order to study the efficiency of the algorithms. Figure 4.2 displays three finite element meshes of the considered fluid-structure system for which the number of dofs are 74 000, 196 000, and 578 000. Let n_{dof}^{system} and n_{nz}^{K} be the total number of dofs of the computational model and the number of nonzero entries in matrix $[K_p]$. For the three generalized eigenvalue problems, we are interested in computing the first $N_u = 100$ eigenvectors of the elastic eigenvalue problem, the first $N_p = 100$ eigenvectors of the acoustic eigenvalue problem, and the first $N_h = 70$ eigenvectors of the sloshing/capillarity eigenvalue problem.

4.5.2 Elastic eigenvalue problem

The double projection method requires to find the optimum size of the initial projection basis $[\Phi_u^{\mathrm{I}}]$ in order to accurately calculate the eigenvalues and to ensure a low computational and memory usage. Let $0 < \lambda_1^u(\mathcal{N}_u) \leq \ldots \leq \lambda_{N_u}^u(\mathcal{N}_u)$ be the eigenvalues computed as explained

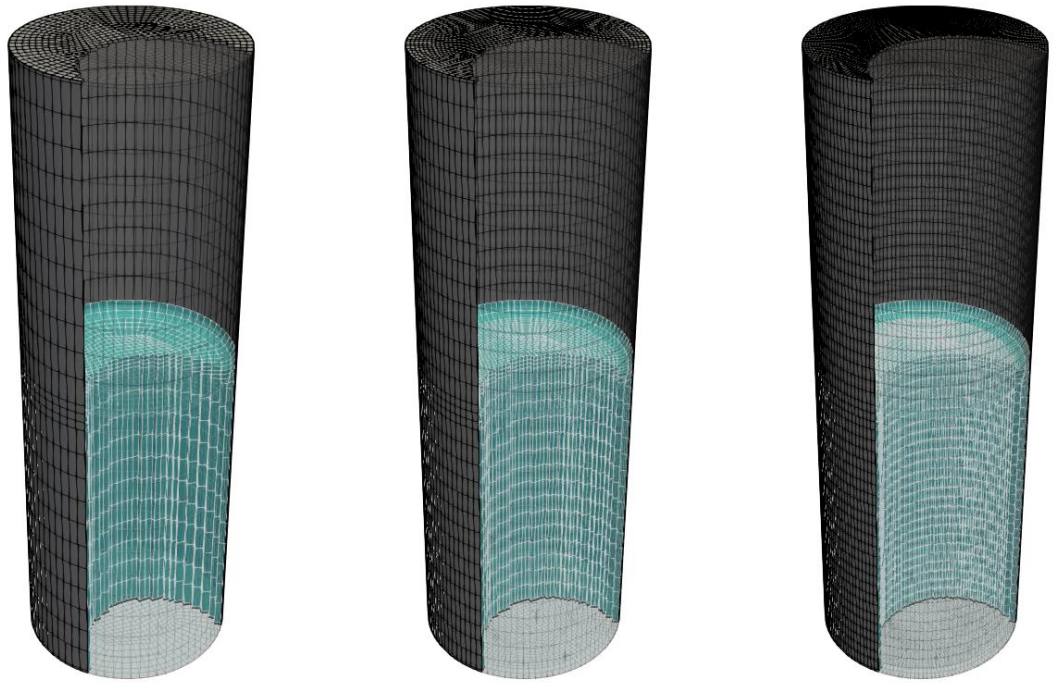

$n_{dof}^{system} = 74\,000$ $n_{dof}^{system} = 196\,000$ $n_{dof}^{system} = 578\,000$

Figure 4.2 – Example of three finite element meshes of the fluid-structure system corresponding to three different mesh fineness.

$n_{dof}^{system}\ /10^3$	$n_p\ /10^3$	$n_{nz}^K\ /10^5$
74	44	24
127	83	46
196	134	75
362	262	147
578	441	249
850	679	387
1 142	945	541
1 664	1 411	811
2 298	1 990	1 147

Table 4.2 – Numerical data of the mesh and sparsity of matrix $[K_p]$.

in Section 4.4.1. A convergence analysis of the largest eigenvalue, $\lambda^u_{N_u}$, with respect to $\mathcal{N}_u$ is performed for mesh with $n_{dof}^{system} = 196\,000$. Figure 4.3 displays the graph of the largest eigenfrequency

$$\mathrm{Conv}_{N_u}(\mathcal{N}_u) = \sqrt{\frac{\lambda^u_{N_u}(\mathcal{N}_u)}{\lambda^{u,\mathrm{ref}}_{N_u}}} \quad ,$$

as a function of $\mathcal{N}_u$, in which $\lambda^{u,\mathrm{ref}}_{N_u}$ is the eigenvalue of rank N_u corresponding to the reference solution (see Section 4.2.1). It can be seen that a good approximation is obtained with $\mathcal{N}_u = 500$. From now on, in this chapter, we use $\mathcal{N}_u = 500$. An analysis of the computer resources required

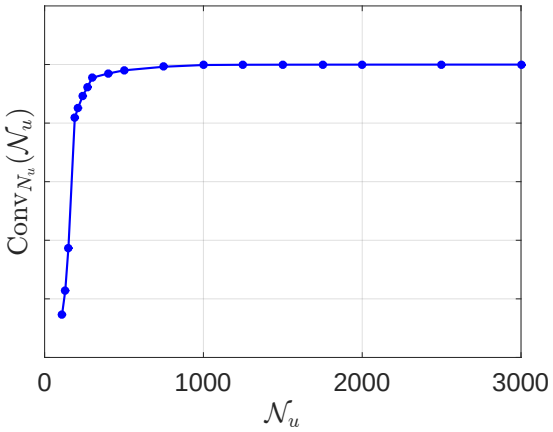

Figure 4.3 – Graph of function $\mathcal{N}_u \mapsto \mathrm{Conv}_{N_u}(\mathcal{N}_u)$ showing the convergence of the highest normalized eigenfrequency that is considered with respect to $\mathcal{N}_u$ using the double projection algorithm.

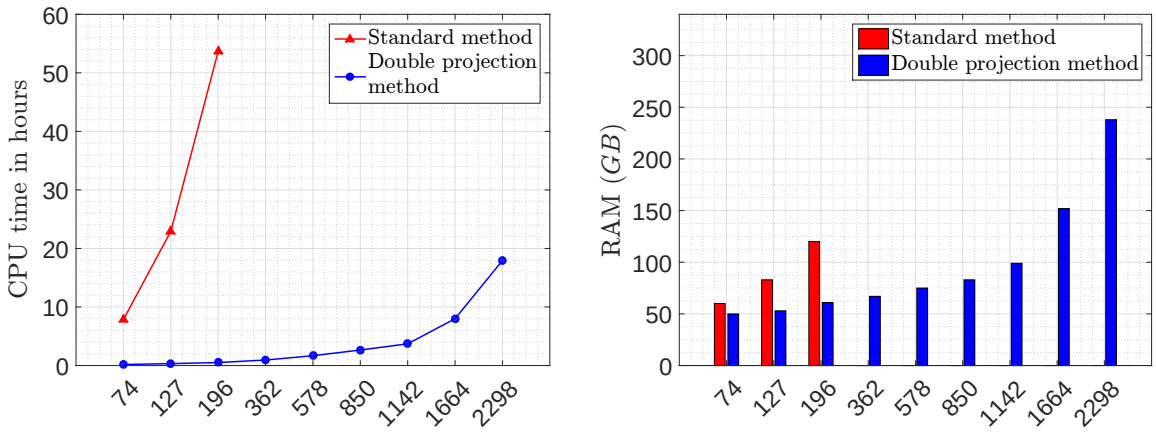

Figure 4.4 – CPU time (left figure) and RAM (right figure) required for solving the elastic eigenvalue problem using standard method and double projection method as a function of the dofs number defined in Table 4.2.

for solving the elastic eigenvalue problem has been performed with respect to the size of the finite element mesh, for both standard and double projection methods. Figure 4.4 displays the graphs of the CPU time (left) and the graph of the maximum RAM (right) required for the computation with respect to the values of n_{dof}^{system} given in Table 4.2. It can be seen that the RAM required for the computation with $n_{dof}^{system} = 362\,000$ exceeds 264 GB when the standard method is used, implying an out of memory and a stop of computation. Consequently, the computation cannot be carried out for $n_{dof}^{system} > 196\,000$. The double projection method proposed allows for solving the elastic eigenvalue problem for all the values of n_{dof}^{system} considered in Table 4.2. In addition, Figure 4.4 shows that the double projection yields a considerable gain for the CPU time with respect to the standard method.

4.5.3 Acoustic eigenvalue problem

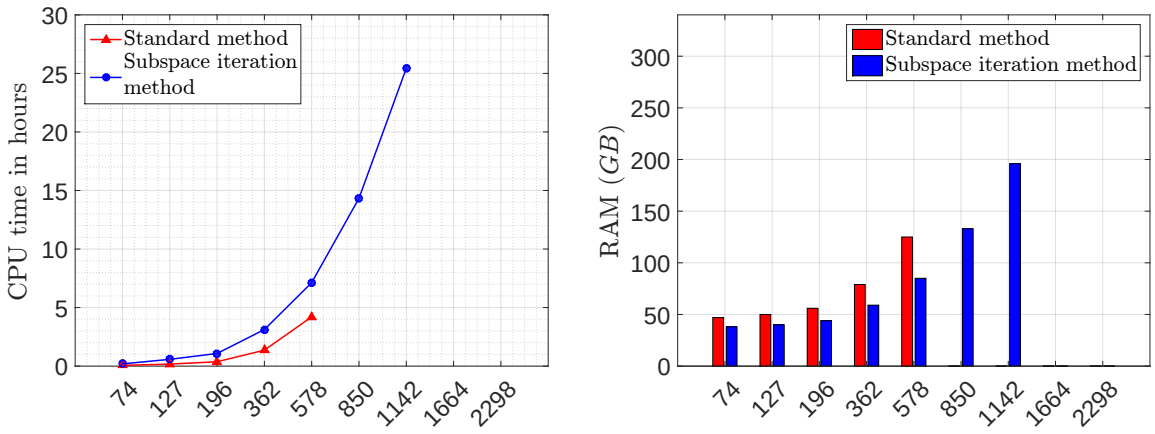

Figure 4.5 – CPU time (left figure) and RAM (right figure) required for solving the acoustic eigenvalue problem using standard method and subspace iteration method as a function of the dofs number defined in Table 4.2.

Figure 4.5 displays the graph of the computational CPU time (left) and the graph of the maximum RAM (right) used for solving the acoustic eigenvalue problem for all the values of n_{dof}^{system} considered in Table 4.2 using both standard and subspace iteration methods. It can be seen that, for the standard method, the RAM required for $n_{dof}^{system} = 850\,000$ exceeds 264 GB, and consequently, could not be carried out. In comparison, the subspace iteration method allows for solving the acoustic eigenvalue problem for larger values of n_{dof}^{system} until $n_{dof}^{system} = 1\,142\,000$ but in counterpart generates a higher CPU-time consumption, which is compensated by the fact that the computation can effectively be done. Note that the CPU time with subspace iteration is correlated to the choice of the tolerance for the convergence and can be decreased if a less demanding tolerance is used.

4.5.4 Sloshing/capillarity eigenvalue problem

The double projection method requires to find the optimum size of the initial projection basis $[\Phi_h^{\mathrm{I}}]$ in order to accurately solve the sloshing/capillarity eigenvalue problem and to ensure a low-computation time and RAM usage. Let $0 < \lambda_1^h(\mathcal{N}_h, h_K) \leq \ldots \leq \lambda_{N_h}^h(\mathcal{N}_h, h_K)$ be the sloshing/capillarity eigenvalues computed as explained in Section 4.4.3. A convergence analysis of the largest eigenvalue, $\lambda_{N_h}^h(\mathcal{N}_h, h_K)$, is performed with respect to the size $\mathcal{N}_h$ of the initial subspace and to the height h_K of the small acoustic-fluid layer used for constructing the approximation $[K_p^a]$ of $[K_p]$. Figure 4.6 displays the graph of

$$\mathrm{Conv}_{N_h}(\mathcal{N}_h, h_K) = \sqrt{\frac{\lambda_{N_h}^h(\mathcal{N}_h, h_K)}{\lambda_{N_h}^{h,\mathrm{ref}}}},$$

in which $\lambda_{N_h}^{h,\mathrm{ref}}$ is the eigenvalue of rank N_h corresponding to the reference solution (see Section 4.2.3). It can be seen that a good approximation is obtained for $\mathcal{N}_h = 500$ and h_K corresponding to 7% of acoustic-fluid depth that is retained in the following. The sloshing/capillarity

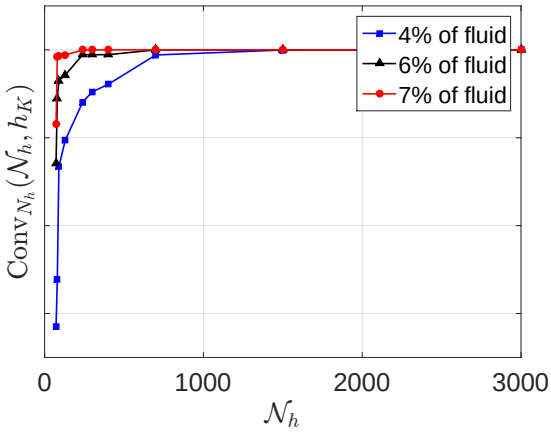

Figure 4.6 – For given h_K corresponding to 4%, 6%, and 7% of acoustic-fluid depth, graph of function $\mathcal{N}_h \mapsto \mathrm{Conv}_{N_h}(\mathcal{N}_h, h_K)$ showing the convergence of the highest normalized eigenfrequency that is considered with respect to $\mathcal{N}_h$ using the double projection algorithm.

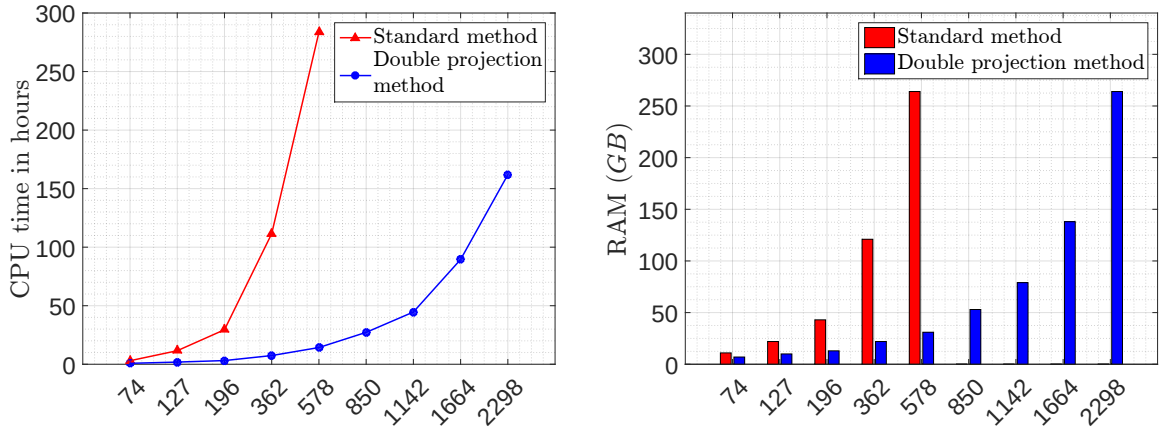

Figure 4.7 – CPU time (left figure) and RAM (right figure) required for solving the sloshing/capillarity eigenvalue problem using standard method and double projection method as a function of the dofs number defined in Table 4.2.

eigenvalue problem is analyzed with respect to the number of dofs n_{dof}^{system} of the finite element mesh described in Table 4.2 for both standard and double projection methods. Figure 4.7 displays the graph of the CPU time and the graph of the maximum RAM required for the computation. It can be seen that the RAM required for the computation with $n_{dof}^{system} = 850\,000$ exceeds 264 GB when the standard method is used, implying an out of memory and a stop of computation. Consequently, the computation cannot be carried out for $n_{dof}^{system} > 578\,000$. In comparison, the double projection method allows for solving the sloshing/capillarity eigenvalue problem for all the values of n_{dof}^{system} considered in Table 4.2. In addition Figure 4.7 (left) shows that the double projection yields a considerable gain for the CPU time with respect to the standard method.

4.5.5 Conclusion on the efficiency of the proposed computational strategy

Non-standard algorithms have been proposed for solving generalized eigenvalue problems related to large-scale fluid-structure computational models that are simulated with mid-power computers. In this framework, the limitations of the computer resources are principally due to the RAM limitations. The double projection method and the subspace iteration method that are proposed allow for solving problems that cannot be treated with standard algorithms. In addition, the use of the double projection method not only allows for circumventing the RAM limitation but also allows for considerably decreasing the CPU time with respect to the standard algorithms. The algorithms proposed allow for computing a large scale fluid-structure computational model on mid-power computers but certainly, would allow for computing very large scale fluid-structure computational models on high-power computers.

Chapter 5

Quantifying the influence of the triple line coupling operator

Contents

5.1 Introduction and hypotheses

The new formulation proposed in [86] allows for taking into account the capillary effects occurring at the triple line under the assumption of a deformable structure. The matrix $[C_{hu}]^T$ introduced in the equation Eq. (2.65) due to the second term in the right-hand side of Eq. (2.9), and constructed by algebraic duality [85, 86], allows for better taking into account the dynamical effects of the triple line on the elastic structure. We recall that both operators $[C_{hu}]$ and $[C_{hu}]^T$ depend on the capillary contact angle, but also depend on the local curvatures $< K_\Gamma >$ and $< K_\Sigma >$ of the structure and of the free surface around the triple line. This influence is seen through the term $\mathcal{J}$ defined (see Eq. (2.11)) by

$$\mathcal{J}\,\mathbf{u} = d_h\,\mathbf{u}\cdot\mathbf{n}^u - \frac{\partial \mathbf{u}\cdot\mathbf{n}^u}{\partial \boldsymbol{\nu}^\Sigma} \quad . \tag{5.1}$$

Indeed, d_h is directly related to the contact angle θ and to the local curvatures of both the structure $< K_\Sigma >= 1/R_\Sigma$ and the free surface $< K_\Gamma >= 1/R_\Gamma$ (see Figure 5.1) by

$$d_h = \frac{< K_\Gamma > - < K_\Sigma > \cos(\theta)}{\sin(\theta)} \quad . \tag{5.2}$$

We also recall that another influence of the triple line in the dynamical equation of the coupled system appears through the free-surface stiffness matrix $[K_c^l]$, defined by Eqs. (2.35) and (2.56),

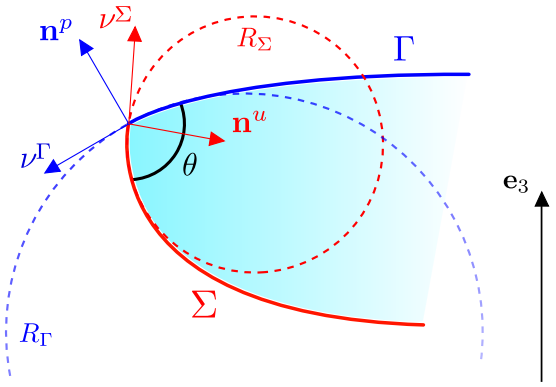

Figure 5.1 – Sketch of the contact angle between the structure and the free surface, and of the corresponding unit normals to each surface.

in which c_h is written as

$$c_h = \frac{< K_\Gamma > \cos(\theta) - < K_\Sigma >}{\sin(\theta)} \quad . \tag{5.3}$$

It is therefore essential to quantify the importance of the matrices related to the triple line in relation to each other, in particular, to highlight the importance of the new term $[C_{hu}]^T$ regarding the dynamical behavior of the coupled fluid-structure system. This chapter is therefore devoted to the analysis of a numerical application especially designed to quantify the influence of the coupling matrix $[C_{hu}]^T$ on the fluid-structure system dynamical responses. For that, we consider the fluid-structure system for which the liquid is coupled to the elastic structure only by the triple line. Consequently, the liquid is not excited by the structure if $[C_{hu}]$ and $[C_{hu}]^T$ are removed. It is important to note that the purpose of this section is to see if matrix $[C_{hu}]^T$ contributes to the system dynamics and to find one or more cases, for which the influence of $[C_{hu}]^T$ is significant. The quantification of the influence of coupling matrix $[C_{hu}]^T$ is done within the framework of linear dynamics, which is why the simulations presented in this chapter are performed with the reduced-order model presented in Section 2.5 under the assumption of a linear elastic structure (*i.e.* considering $\boldsymbol{\mathcal{F}}_{\text{NL}} = \mathbf{0}$).

5.2 Description of the fluid-structure system

In this section, we are interested in describing the coupled fluid-structure system that will be used to quantify the influence of matrix $[C_{hu}]^T$ in comparison to the other coupling terms of the fluid-structure model.

5.2.1 Finite element models and boundary conditions

The considered system is a small elastic cup (cylindrical elastic wall with a bottom elastic plate), whose dimensions are given in the Figure 5.2, containing a liquid for which the contact angle with the vertical elastic wall (cylindrical wall) is greater than 90° (non-wetting liquid). The liquid is in contact with the structure, only on the bottom of the cup and on the triple line, which is common to the vertical wall. Several contact angles between the free surface of the liquid and the elastic wall of the structure are considered, $\theta \in \{143°, 152°, 161°, 169°, 177°\}$, which leads to a modification of the curvature of the free surface especially at the triple line location.

The finite element model of the fluid-structure system is constructed using 3D-solid tetrahedral finite elements with 10 nodes for the structure and for the acoustic liquid (see Figure 5.4).

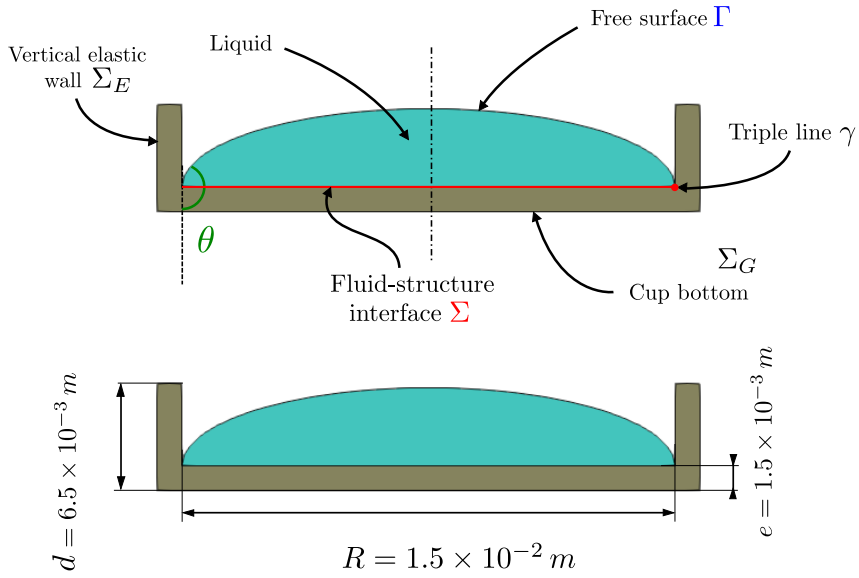

Figure 5.2 – Geometrical identification of the fluid-structure system constituents: liquid, vertical wall, bottom, free surface, triple line, and contact (top figure). Dimensions of the cup (bottom figure).

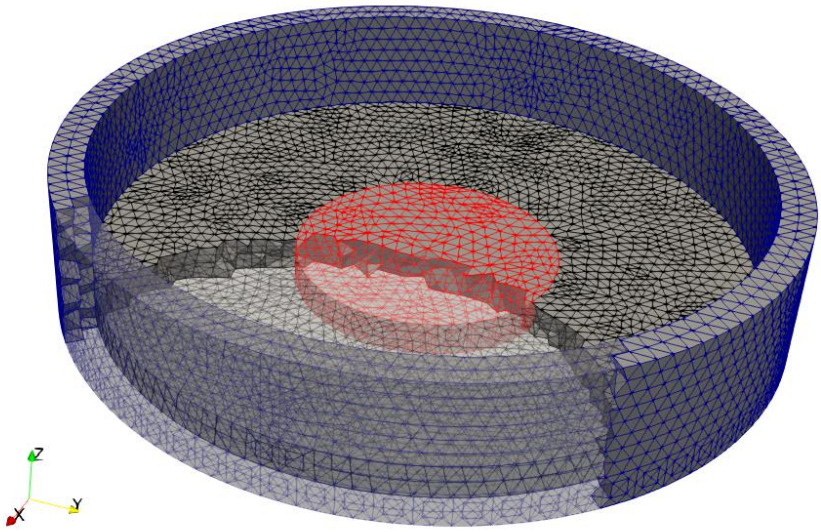

Figure 5.3 – Mesh of the cup.

The free surface of the liquid is meshed using 2D finite elements with 6 nodes and the triple line is meshed using 1D finite elements with 3 nodes, with quadratic interpolation functions. Figure 5.4 shows the 5 meshes of the fluid-structure system with their respective contact angles. It can be seen that the smaller the contact angle, the greater the local curvature of the surface at the triple line. Figure 5.5 displays a cross-section view of the different free surfaces of the considered fluid-structure system, on which we can see the local curvature of the free surface around the triple line. Table 5.1 reports the local curvature $< K_\Gamma >$ of the free surface at the triple line as a function of the contact angle.

The boundary conditions applied to the structure are defined in order to avoid the energy

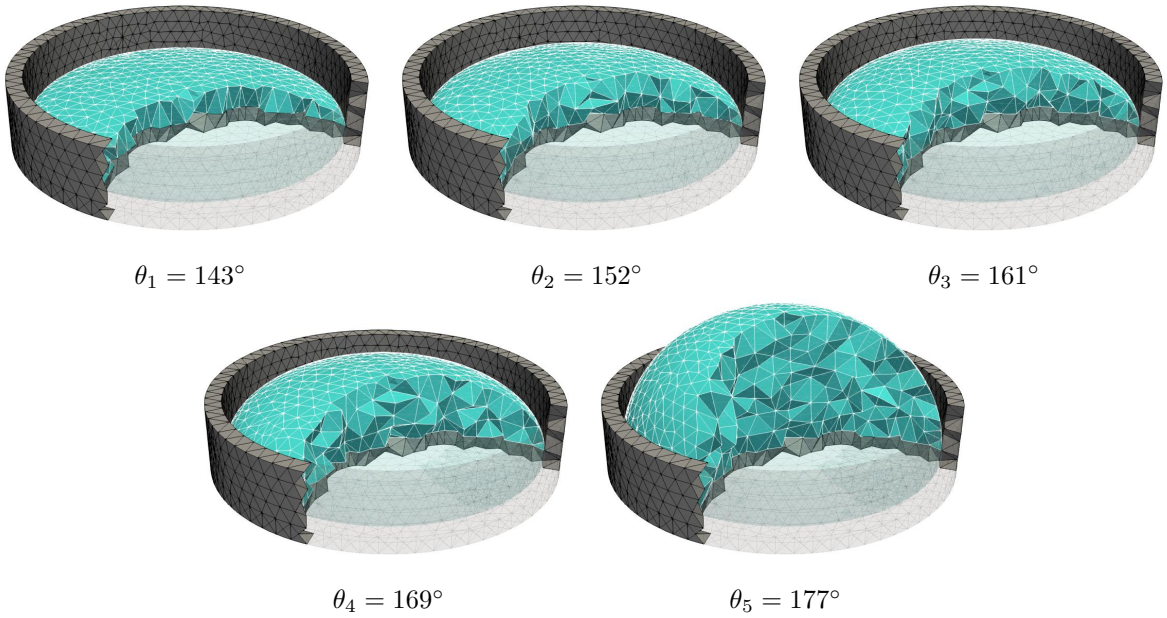

Figure 5.4 – Computational finite element meshes of the fluid-structure system for 5 contact angles $\theta \in \{143°, 152°, 161°, 169°, 177°\}$.

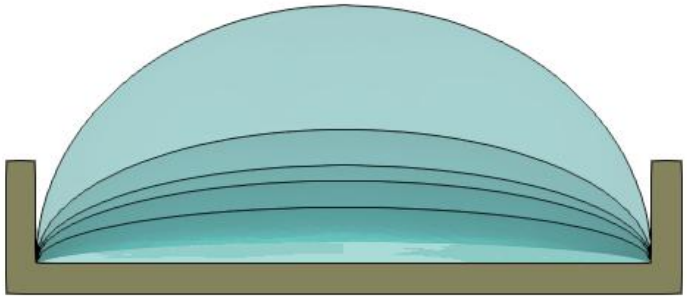

Figure 5.5 – Cross-section of the fluid-structure systems presented in Figure 5.4 for the different contact angles θ.

	θ_1	θ_2	θ_3	θ_4	θ_5
$< K_\Gamma >$	408	332	315	252	93

Table 5.1 – Curvature $< K_\Gamma >$ of the free surface at the triple line with respect to the considered contact angles θ_i, $i = 1, \ldots, 5$.

transmission from the structural excitation (which are radial forces applied to the vertical elastic cylindrical wall) to the internal liquid by the contact surface Σ but to have only an energy transmission by the triple line coupling.

A portion of the bottom of the cup, located on a centered disk with a radius of $6 \times 10^{-3}\, m$ (part of the mesh colored red in Figure 5.3) is fixed in all three directions to prevent rigid body motions of the elastic structure. The nodes located in the rest of the cup bottom (black-color nodes in Figure 5.3) are locked along the vertical direction $\mathbf{e}_3$. This boundary condition prevents

vertical displacements of the elastic structure on Σ, which means that $\mathbf{n}^p \cdot \mathbf{u} = 0$ on Σ (that implies $[C_{pu}] = [0]$). The nodes located in the rest of the structure (blue-color nodes in Figure 5.2 right) are left free. These boundary conditions ensure that the transmission of the excitation energy from the structure to the internal liquid is only by the coupling with the triple line.

5.2.2 Parameters of the model and eigenfrequency characterization

The material parameters of the structure are: Young modulus $E = 50\, N.m^{-2}$, Poisson coefficient $\nu = 0.25$, mass density $\rho_S = 7900\, Kg.m^{-3}$, and damping rate $\tau_S = 5 \times 10^{-5}$. The parameters of the acoustic fluid are: sound velocity $c_0 = 0.08\, m.s^{-1}$ and mass density $\rho_0 = 1000\, Kg.m^{-3}$. The parameters of the free surface are: surface tension coefficient $\sigma_\Gamma = 0.0728$, and gravity intensity $g = 9.81\, m.s^{-2}$.

Table 5.2 presents the eigenfrequency characterization of each part of the coupled fluid-structure system corresponding to the three generalized eingevalue problems defined in Section 2.5. The eigenfrequencies of the structure, of the liquid, and of the free surface are interlaced, which strongly promotes resonance coupling in the dynamical responses of the system.

Contact angle	Sloshing eigenfrequencies (in Hz)								
θ_1	2.82	4.61	6.51	6.61	8.52	9.93	10.89	13.31	13.42
θ_2	3.29	5.33	7.42	7.47	9.72	10.89	12.28	14.29	14.95
θ_3	3.56	5.75	7.82	8.01	10.35	11.24	13.05	14.58	14.71
θ_4	3.79	6.05	8.01	8.35	10.71	11.14	12.70	13.47	14.22
θ_5	3.58	5.58	6.61	7.67	8.37	8.82	9.97	11.15	12.01
Contact angle	Acoustic eigenfrequencies (in Hz)								
θ_1	8.35	9.26	10.7	10.26	11.09	11.26	12.00	12.25	12.35
θ_2	5.94	6.88	7.81	7.94	8.75	8.99	9.68	10.02	10.14
θ_3	5.18	6.14	7.08	7.24	8.04	8.31	8.97	9.36	9.49
θ_4	4.11	5.11	6.10	6.28	7.07	7.41	8.04	8.51	8.65
θ_5	2.84	3.97	5.03	5.22	5.87	6.07	6.35	6.96	7.08
Contact angle	Elastic eigenfrequencies (in Hz)								
$\{\theta_1, \theta_2, \theta_3, \theta_4, \theta_5\}$	2.97	4.08	5.84	6.56	6.63	7.37	7.79	8.92	9.08

Table 5.2 – Table of the first 9 sloshing eigenfrequencies of the free surface, acoustic eigenfrequencies of the liquid, and elastic eigenfrequencies of the structure (in Hz).

5.2.3 Quantities of interest

The results of the numerical simulations are observed by different quantities of interest defined on certain observation points. These interest quantities are chosen in order to visualize a global behavior of the fluid-structure system towards matrix $[C_{hu}]^T$. It should be recalled that simulations are made considering a linear elastic structure. The interest quantities are therefore defined for each part of the system as follows.

- For the structural displacement, the quantity of interest, dB^U, is defined as the spatial averaging of all the nodes. Let $\mathbf{U}_{\mathbf{x}_i^u}(t)$ be the vector in $\mathbb{R}^3$ of the 3 displacement dofs of node $\mathbf{x}_i^u$, which is constructed from $\mathbf{U}(t)$ (with values in $\mathbb{R}^{n_u}$). Let $\omega \mapsto \widehat{\mathbf{U}}_{\mathbf{x}_i^u}(2\pi\nu)$ be the

Fourier transform of $t \mapsto \mathbf{U}_{\mathbf{x}_i^u}(t)$, the quantity of interest $dB^U(2\pi\nu)$ is defined by,

$$dB^U(2\pi\nu) = \frac{1}{n_u/3} \sum_{i=1}^{n_u/3} 20 \log_{10}(\| \widehat{\mathbf{U}}_{\mathbf{x}_i^u}(2\pi\nu) \|_{\mathbb{C}^3}) \quad , \tag{5.4}$$

- For the pressure in the acoustic liquid, the quantity of interest dB^P is defined by

$$dB^P(2\pi\nu) = \frac{1}{n_p} \sum_{i=1}^{n_p} 20 \log_{10}(|\widehat{P}_i(2\pi\nu)|) \quad . \tag{5.5}$$

- For the free-surface elevation, the quantity of interest dB^H is defined by

$$dB^H(2\pi\nu) = \frac{1}{n_h} \sum_{i=1}^{n_h} 20 \log_{10}(|\widehat{H}_i(2\pi\nu)|) \quad . \tag{5.6}$$

5.2.4 Definition of the external excitation of the system

The external forces applied to the elastic structure are radial forces defined hereinafter. We consider the sector of the cylindrical elastic wall defined by the polar angle $[-\pi/16\,,\,\pi/16]$. Let n_{exci} be the number of nodes belonging to this sector and located on the external surface of the cylindrical wall. A radial force is applied to each one of these nodes with an intensity equal to $1/n_{\text{exci}}$. These radial forces are represented by the time depending vector $\mathbf{F}_u(t)$

$$\mathbf{F}_u(t) = \alpha\, g(t)\, \mathbf{F} \quad , \tag{5.7}$$

in which the vector $\mathbf{F}$ is time independent and is such that $\|\mathbf{F}\| = 1$. In Eq. (5.7), α is the intensity coefficient taken as $\alpha = 5 \times 10^{-8}$ and $g(t)$ is the time function of the dynamical excitation, whose Fourier transform is constant in the frequency band of excitation, $\mathbb{B}_e = [\nu_{min}\,,\,\nu_{max}]\,Hz$, with $\nu_{min} = 1\,Hz$ and $\nu_{max} = 10\,Hz$, which writes

$$g(t) = 2\,\frac{\sin(\pi\Delta\nu\,t)}{\pi\,t}\,\cos(2\pi\,s\,\Delta\nu\,t) \qquad , \qquad \widehat{g}(2\pi\nu) = \mathbb{1}_{\mathbb{B}_e \cup \mathbb{B}_e}(\nu) \quad , \tag{5.8}$$

in which $\underline{\mathbb{B}}_e = [-\nu_{\max}\,,\,-\nu_{\min}]$, $\Delta\nu = \nu_{max} - \nu_{min}$ and $s = (\nu_{max}+\nu_{min})/(2\Delta\nu)$. In Eq. (5.8), one can see that $\widehat{g}(2\pi\nu) = 1$ if $\nu \in \mathbb{B}_e$ and 0 if $\nu \in \mathbb{R}^+ \backslash \mathbb{B}_e$. The dynamical responses of the system are computed in the time domain. The Fourier transform of the time responses allows for obtaining the responses in the frequency domain over chosen frequency band of analysis $\mathbb{B}_a = [0\,,\,40]\,Hz$. The computation is carried out on a truncated time domain $[t_{ini},\, t_{ini}+T]$ with T $t_{ini} = -66.67\,s$ and $T = 1\,469.32\,s$ because sloshing resonances are very weakly damped phenomena and require a long simulation time before returning to equilibrium position. The sampling frequency and the number of time steps are chosen as $\nu_e = 80\,Hz$ and $N_t = 122\,880$.

5.2.5 Convergence analysis

The linear reduced-order model used for the simulations requires a convergence analysis with respect to the size N_{phu} of the projection basis $[\Psi]$ (see Section 2.5. Since the dynamical reference solution cannot be computed for such large-scale and long-time computational model, it is assumed that the convergence is reached when the response is no longer sensitive to parameters N_p, N_h or N_u. Let X be representing whether P, H or U. The quantity of interest

$dB^X(2\pi\nu)$ is rewritten as $dB^X(2\pi\nu; N_p, N_h, N_u)$ for indicating its dependency with respect to the modal truncation order N_p, N_h, and N_u. We choose to normalize the convergence function with respect to the values $\overline{N}_p = 200$, $\overline{N}_h = 250$, and $\overline{N}_u = 100$. The convergence function $(N_p, N_h, N_u) \mapsto \mathrm{Conv}_X(N_p, N_h, N_u)$ is defined by,

$$\mathrm{Conv}_X(N_p, N_h, N_u) = \left\{ \frac{\displaystyle\int_{\mathbb{B}_a} dB^X(2\pi\nu; N_p, N_h, N_u)^2 \, d\nu}{\displaystyle\int_{\mathbb{B}_a} dB^X(2\pi\nu; \overline{N}_p, \overline{N}_h, \overline{N}_u)^2 \, d\nu} \right\}^{1/2} . \tag{5.9}$$

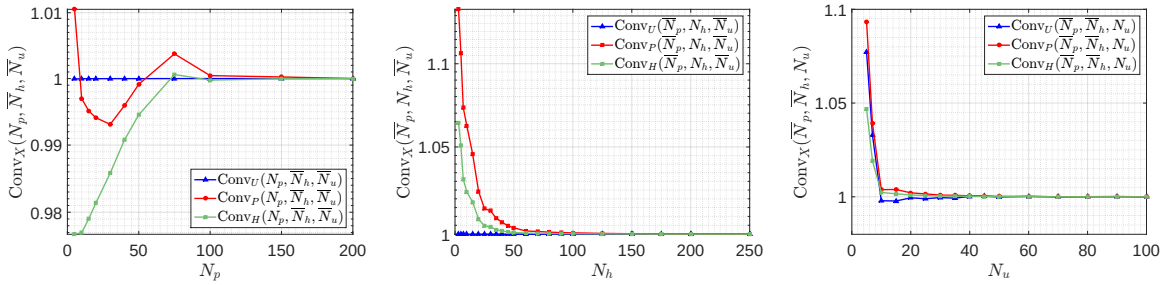

Figure 5.6 – Graphs of the convergence of the solutions obtained in terms of **P**, **H**, and **U** at the observation points with respect to N_p (left figure), to N_h (middle figure), and to N_u (right figure).The vertical axis is in log scale.

Three convergence analyses are then performed with respect to N_p, to N_h, and to N_u. Figure 5.6 displays the graphs of

$$N_p \mapsto \mathrm{Conv}_X(N_p, \overline{N}_h, \overline{N}_u) \quad \text{for} \quad X = \{P, H, U\} \tag{5.10}$$

$$N_h \mapsto \mathrm{Conv}_X(\overline{N}_p, N_h, \overline{N}_u) \quad \text{for} \quad X = \{P, H, U\} \tag{5.11}$$

$$N_u \mapsto \mathrm{Conv}_X(\overline{N}_p, \overline{N}_h, N_u) \quad \text{for} \quad X = \{P, H, U\} \tag{5.12}$$

It is shown that the convergence analyses yield the optimal order of the ROM: $N_p = 100$, $N_h = 80$, and $N_u = 50$. This optimal order of the ROM is used in the following computations.

5.3 Quantification of the influence of $[C_{hu}]^T$ with respect to θ

In order to quantify the influence of the coupling matrix $[C_{hu}]^T$, two computations are performed. The first one considers all coupling matrices and the results of this computation is presented in blue-dashed line in Figures 5.8 to 5.10. In the second calculation, the coupling matrix $[C_{hu}]^T$ is removed and the results of this computation are displayed in red-solid line in Figures 5.8 to 5.10. Figure 5.8, 5.9, and 5.10 respectively display the graphs of $\nu \mapsto dB^U(2\pi\nu)$, $\nu \mapsto dB^P(2\pi\nu)$, and $\nu \mapsto dB^H(2\pi\nu)$, for the five contact angles θ_i, $i = 1, \ldots, 5$. The results show that the coupling matrix $[C_{hu}]^T$ has a major influence on the dynamical response of the fluid-structure system. This influence can be seen on the graphs of dB^U (in Figure 5.8) for which some resonances appear on the frequency response, which do not occur when $[C_{hu}]^T$ is removed. In fact, one can see that the resonances in the frequency response dB^U without $[C_{hu}]^T$ correspond to structural eigenfrequencies (see Table 5.2). However, the resonances that occur in the frequency response

dB^U with $[C_{hu}]^T$ are highly shifted, due to the coupling matrix $[C_{hu}]^T$. This phenomenon is clearly seen for contact angle θ_1, for which two resonances appear in the neighborhood of the structural resonance located at $4.08\,Hz$. A resonance also appears in the graph of dB^U, for all the contact angles, located between $1.17\,Hz$ and $1.58\,Hz$. This resonance is the first sloshing resonance that is shifted due to the coupling with a resonance of the elastic structure. The results show that the influence of $[C_{hu}]^T$ tends to decrease as the contact angle increases. In addition, the influence of $[C_{hu}]^T$ increases as the local curvature of the free surface increases. A possible explanation for this increasing influence of $[C_{hu}]^T$, which is inversely proportional to θ, is the increasing of the gap between c_h and d_h as θ increases, as shown in Figure 5.7. In this figure, one can notice that the difference between c_h and d_h is greater when the contact angle is small. In addition, we see that the term d_h becomes more important than the term c_h when moving towards small angles. This means that the importance of the linear stiffness term $[K_c^l]$ (proportional to c_h) becomes small compared to the importance of the coupling term $[C_{hu}]^T$ (proportional to d_h). It can therefore be suggested that the influence of the term $[C_{hu}]^T$ becomes significant when two criteria are satisfied: (i)- a negligible contribution of the linear stiffness $[K_c^l]$; (ii)- a strong local curvature of the free surface at the triple line γ.

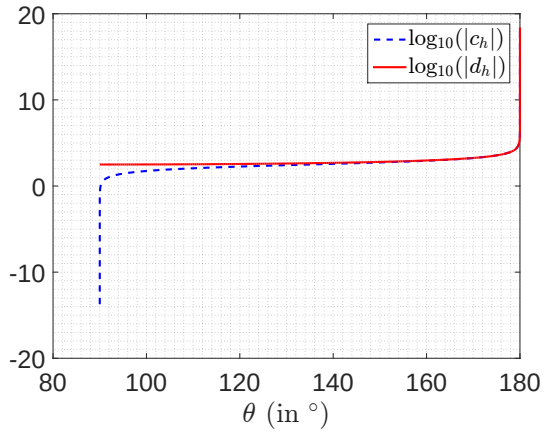

Figure 5.7 – Graphs of $\theta \mapsto \log_{10}(|c_h|)$ (in blue dashed line) and $\theta \mapsto \log_{10}(|d_h|)$ (in red solid line) which display the values of c_h and d_h for the curvature $< K_\Gamma >= 315$.

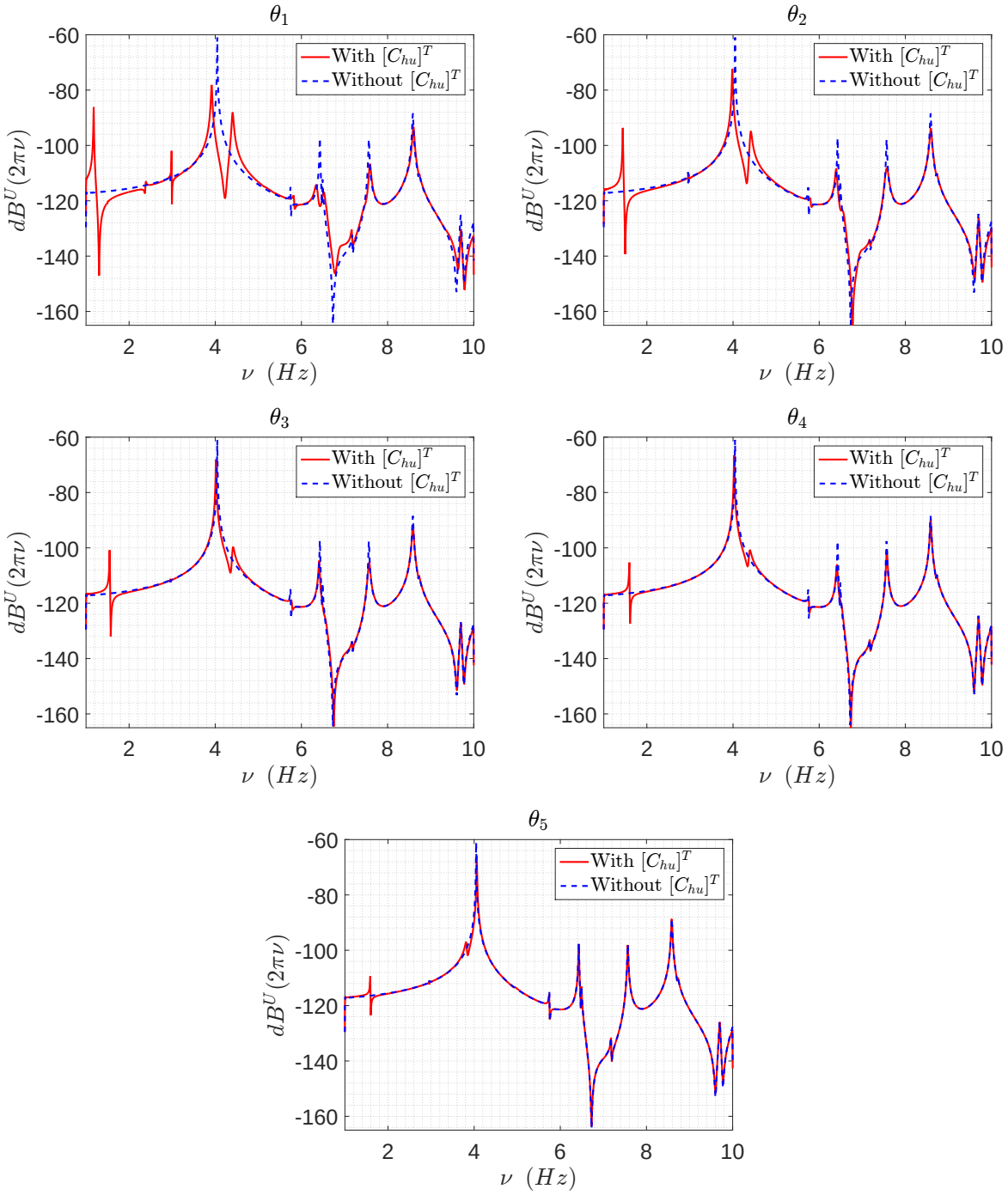

Figure 5.8 – Graphs of $\nu \mapsto dB^U(2\pi\nu)$ for the contact angle $\theta_1 = 143°$ (top left), for the contact angle $\theta_2 = 152°$ (top right), for the contact angle $\theta_3 = 161°$ (middle left), for the contact angle $\theta_4 = 169°$ (middle right), and for the contact angle $\theta_5 = 177°$ (bottom).

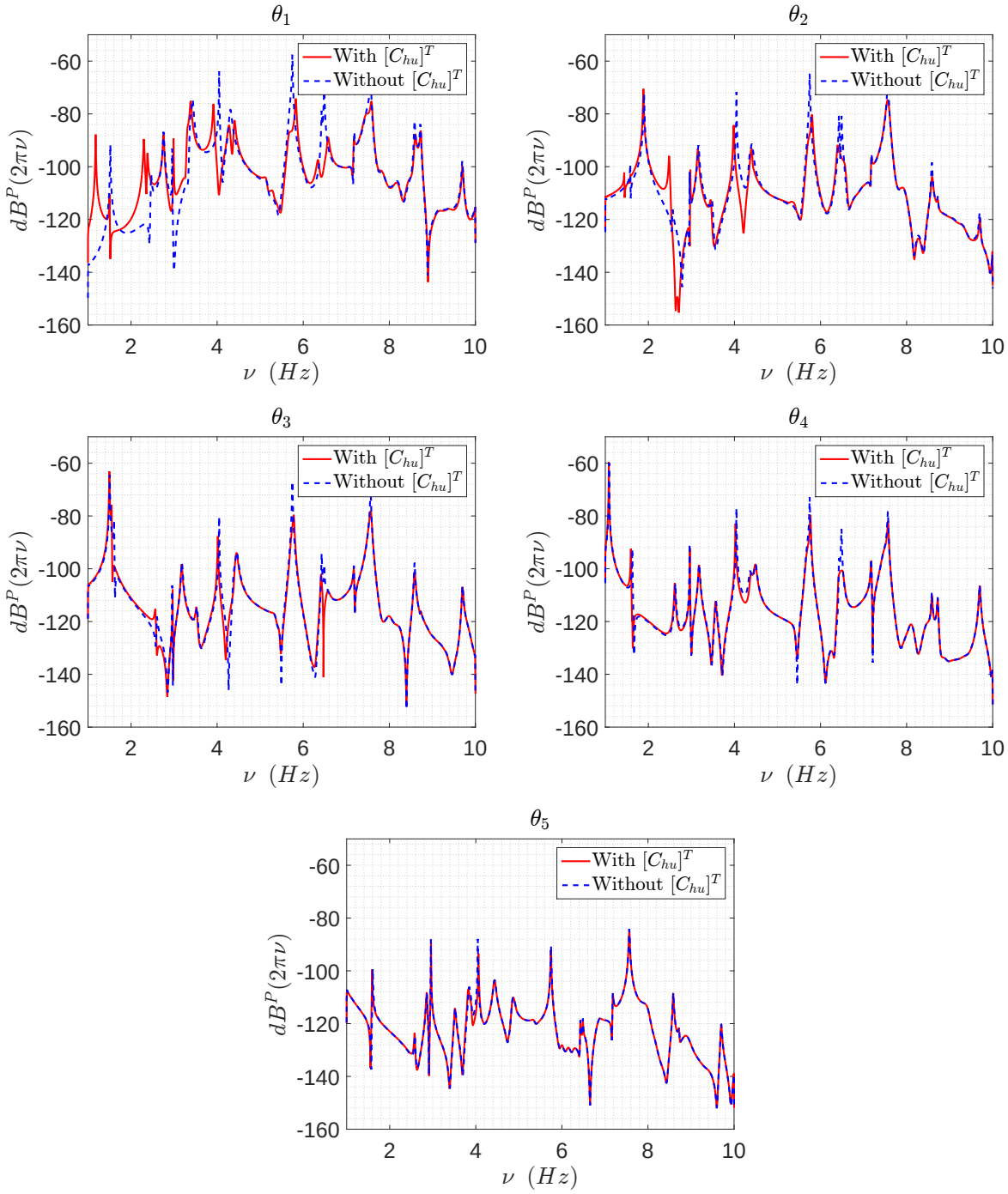

Figure 5.9 – Graphs of $\nu \mapsto dB^P(2\pi\nu)$ for the contact angle $\theta_1 = 143°$ (top left), for the contact angle $\theta_2 = 152°$ (top right), for the contact angle $\theta_3 = 161°$ (middle left), for the contact angle $\theta_4 = 169°$ (middle right), and for the contact angle $\theta_5 = 177°$ (bottom).

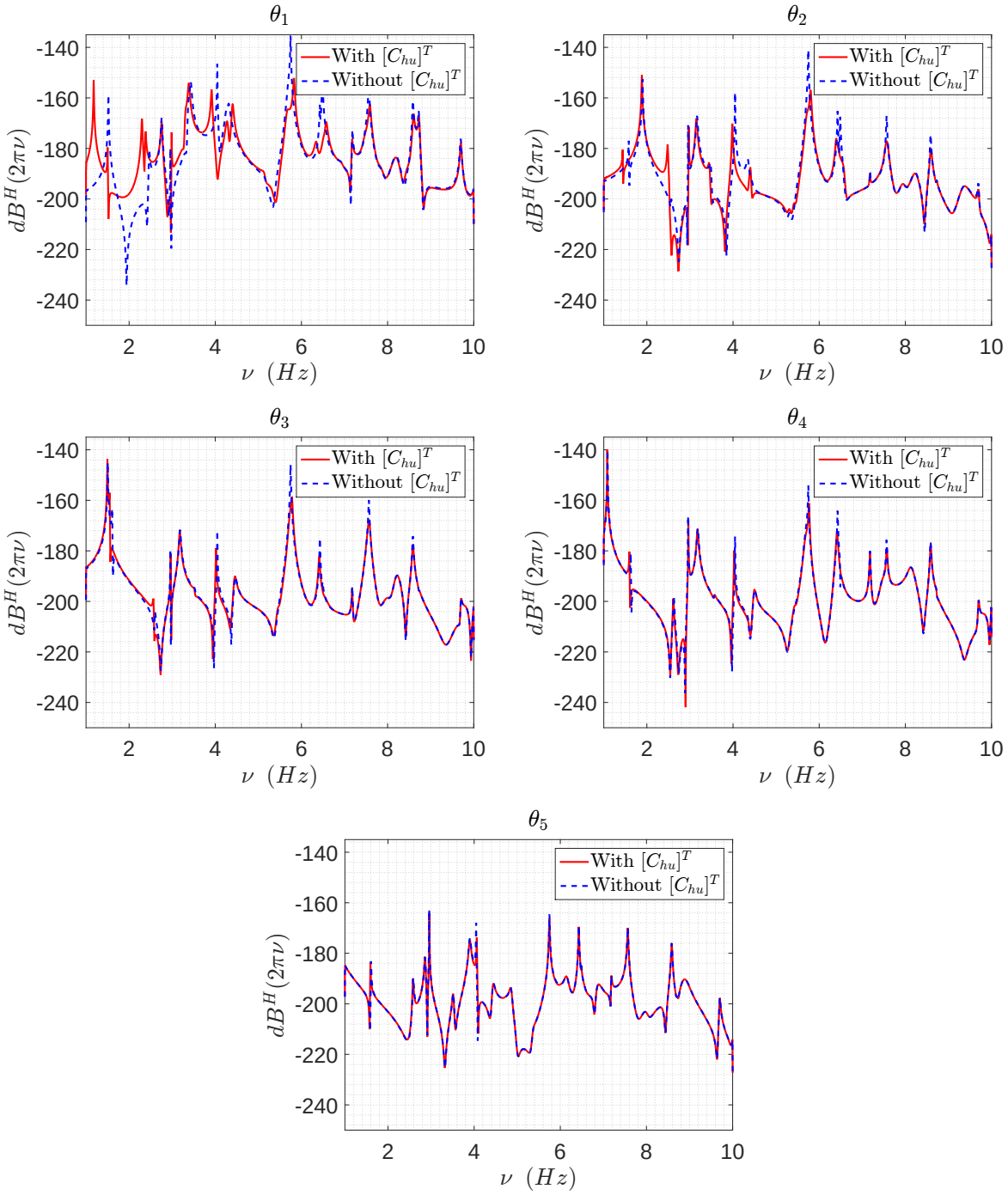

Figure 5.10 – Graphs of $\nu \mapsto dB^H(2\pi\nu)$ for the contact angle $\theta_1 = 143°$ (top left), for the contact angle $\theta_2 = 152°$ (top right), for the contact angle $\theta_3 = 161°$ (middle left), for the contact angle $\theta_4 = 169°$ (middle right), and for the contact angle $\theta_5 = 177°$ (bottom).

Chapter 6

Revisiting and explaining a liquid instability experiment

Contents

6.1 Introduction

In this chapter, a computational study of a fluid-structure system is detailed, which proposes an explanation to an unusual sloshing dynamical excitation observed in an experimental investigation of a vibrating elastic tank partially filled with water, exhibited and investigated in [73, 3]. The experiments performed in [73] were first designed to quantify the effects of an internal liquid on the breathing frequencies of a circular cylindrical thin-walled shell. During these experiments, an *unexpected behavior* was observed when the structure were subjected to a high-frequency excitation of small amplitude. The unusual results obtained in this first experiment were then investigated in further details by [3]. Indeed, it was observed that *a totally unexpected coupling between low-frequency liquid free-surface oscillation and high-frequency shell-wall vibration could occur for a wide range of parameter* (cited from [3]). This result is all the more unexpected as the frequency separation between the first eigenfrequencies of the sloshing modes and the

first structural modes is of order 100. A discussion on these results is proposed in these papers, which suggests that this unexpected behavior would be based on *several unusual characteristics that are not explained readily on the basis of existing theory* (cited from [3]). These authors concluded that the source of such coupling could possibly come from a nonlinear coupling between the liquid and the structure for which the source of nonlinearities would not be precisely known. A first attempt for explaining this unexpected phenomenon has been carried out by [43] using an analytical approach with a linear theory for the structure and a nonlinear one for the free surface of the liquid. These authors conclude that exact quantitative comparisons of theory and experiments may required a more complicated system. In this thesis, an alternative is proposed for explaining the observed phenomenon using a nonlinear structure (geometrical nonlinearities) and a linear compressible liquid (acoustic fluid) with sloshing and capillarity effects using a large-scale computational model. The observed experimental results are simulated and the mechanisms of this unexpected free-surface response is detailed, which constitutes the novelty of this work. The observed experimental results are simulated and the mechanisms of

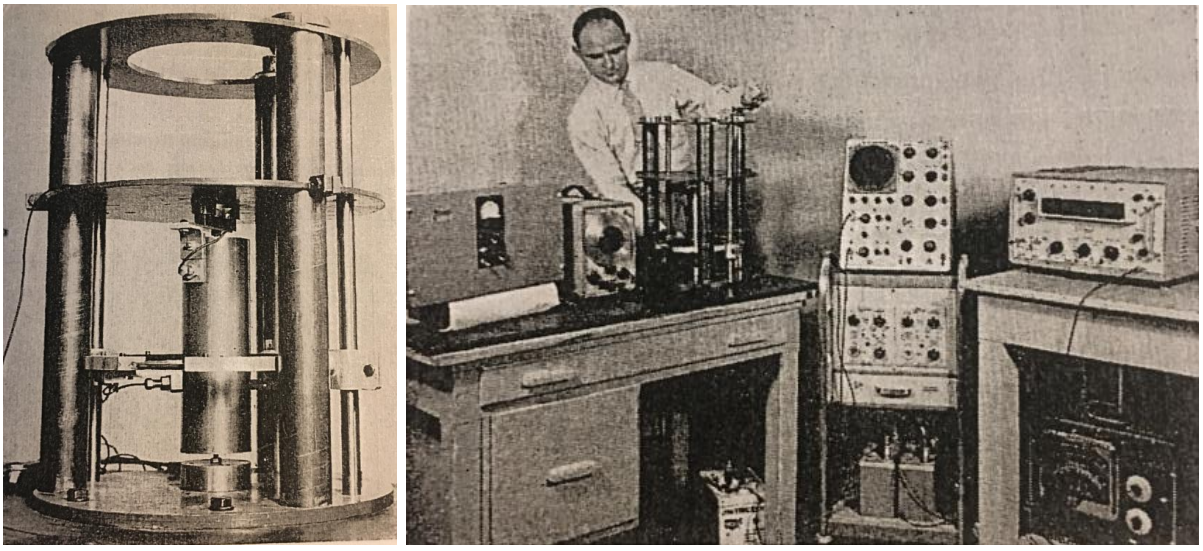

Figure 6.1 – Images of the experimental setup used in [3].

this unexpected free-surface response are detailed. This chapter largely reuses the developments presented in [12, 4, 6, 7, 9, 10, 11] for which the notations have been adapted.

6.2 Computationally reproducing the experimental conditions. Hypotheses and validations.

6.2.1 Finite element modelization of the experimental apparatus

The fluid-structure system is the one described in [73, 3] for which the retained dimensions are those given in [3]. The structure is a steel tank constituted of a thin circular cylinder closed at both ends by circular plates. Its isotropic material properties are given by $E = 2.05 \times 10^{11}\, N.m^{-2}$, $\nu = 0.29$, $\rho_S = 7{,}800\, Kg.m^{-3}$, and damping coefficient $\tau_S = 10^{-6}$. This tank is partially filled with 30% water with sound velocity $c_0 = 1{,}480\, m.s^{-1}$, mass density $\rho_0 = 1{,}014\, kg.m^{-3}$, and damping coefficient $\tau = 10^{-5}$. Since capillary effects are taken into account in the computational model, the characteristics of contact angles and capillary tension coefficient

have been investigated in the literature. The surface tension coefficient for a water-steel contact is $\sigma_\Gamma = 0.0078\, N.m^{-1}$ and the contact angle considered in this work is $\theta = 83°$ (which allows for precomputing equilibrium position of the free surface of the liquid using the software Surface Evolver [32]). Let $R_e = 3.7833 \times 10^{-2}\, m$ and $R_i = 2.76047 \times 10^{-2}\, m$ be the external and the internal radii of the steel cylinder. The thickness of the end plates and the thickness of the cylindrical shell are $h_d = 2.54 \times 10^{-2}\, m$ and $e = 2.286 \times 10^{-4}\, m$. Finally, the total height of the tank and the fluid depth are $h = 0.23876\, m$ and $h_f = 0.3\, h$. The geometry of the computational model is described in Figure 6.2 (left). The origin O of the Cartesian coordinates system $(O, \mathbf{e}_1, \mathbf{e}_2, \mathbf{e}_3)$ is located at the center of the bottom of the cylindrical tank. Axis $\mathbf{e}_3$ coincides with the revolution axis of the system. A particular attention is paid to the modeling of the boundary conditions of the experimental setup. Thus, the structural node located at the bottom center of the tank is locked along its directions $\mathbf{e}_1$, $\mathbf{e}_2$, and $\mathbf{e}_3$. The node located at the top center of the tank is locked along its directions $\mathbf{e}_1$ and $\mathbf{e}_2$. The rotation of the bottom plate is locked with one dof on the edge of the plate. The boundary conditions decribed hereinabove (represented by $\circ$ symbol) are displayed in Figure 6.2 (right figure). Moreover, the experimental pin-ended and cantilever boundary conditions described in [73, 3] are set in order to study the breathing vibrations of the cylinder. In the present numerical simulation, the model has been calibrated by optimizing the thickness of the bottom and top plates such that the numerical eigenfrequencies of the structure coincides with the experimental ones. The optimization must take into account the fact that the plates have to stay rigid compared to the cylinder wall. This is why the optimal thickness of these plates has been set as $h_d = 2.54 \times 10^{-3}\, m$.

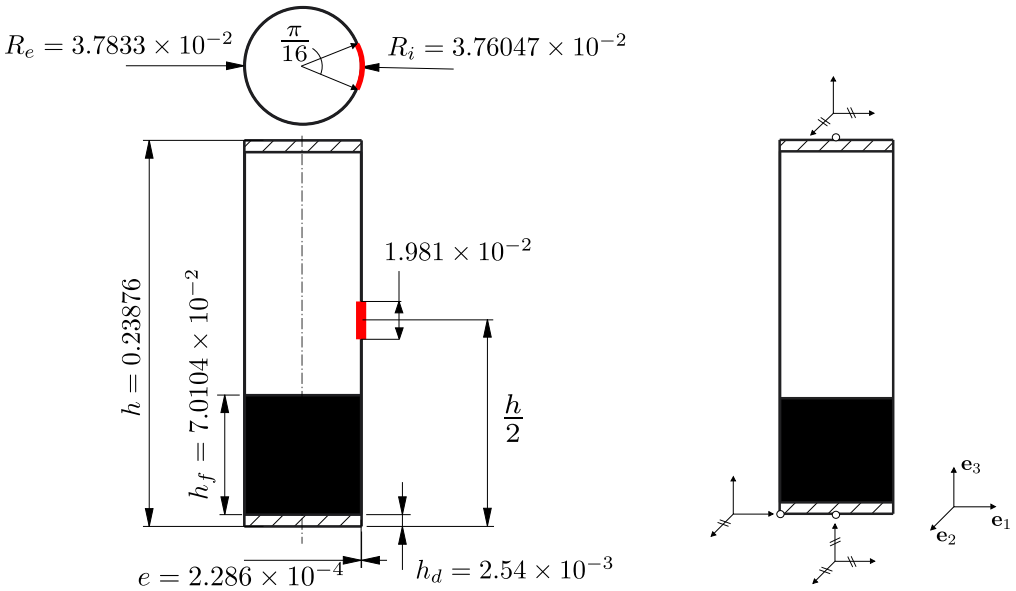

Figure 6.2 – Dimensions of the fluid-structure system (left) and representation of the numerical boundary conditions applied on the system (right).

The finite element model of the fluid-structure system is constructed using 3D-solid tetrahedral finite elements with 10 nodes for the structure and for the acoustic fluid. The free surface of the liquid is meshed using 2D finite elements with 6 nodes and the triple line is meshed using 1D finite elements with 3 nodes. Table 6.1 sums up the characteristics of the finite element mesh, with quadratic interpolation functions.

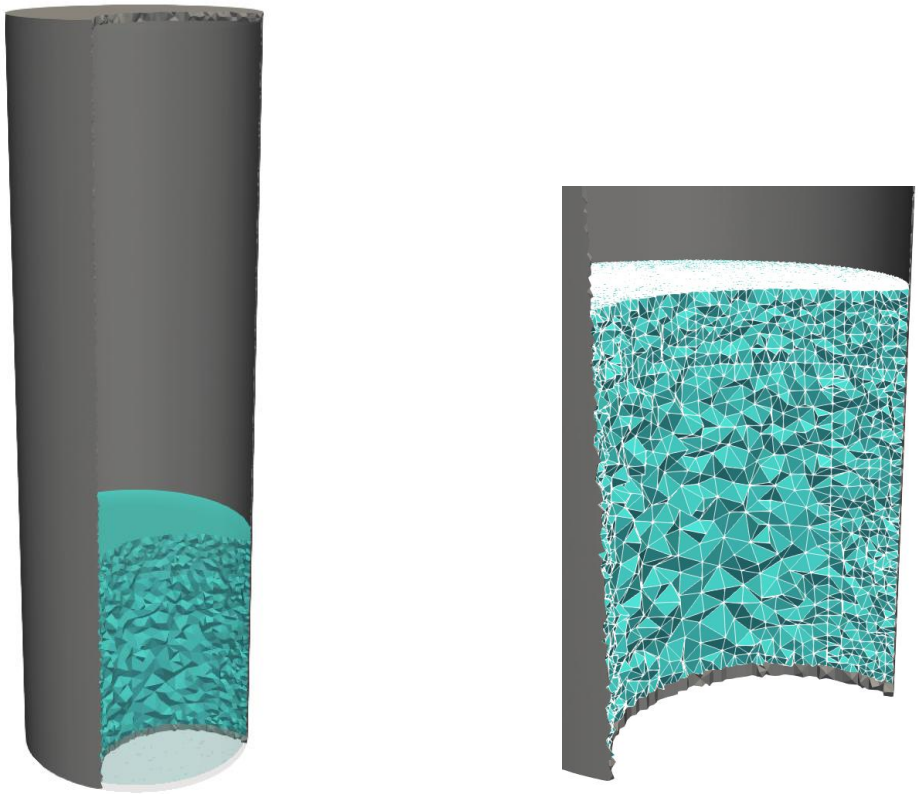

Figure 6.3 – View of the finite element mesh of the fluid-structure system (left figure). Detailed view of the finite elements meshes of the liquid and of its free surface (right figure).

	Nodes	**Dof**	**Elements**
Fluid	431 354	431 354	296 459
Free surface	11 566	11 566	5 684
Structure	660 385	1 981 155	334 784

Table 6.1 – Table of the finite element mesh properties.

6.2.2 Simulating the experimental setup with the computational model

Due to the limited data available in the experimental publications, the validation of the numerical model of the experimental device is performed by comparing the experimental and numerical elastic natural frequencies of the empty structure (data available in [3]) and by comparing the experimental and numerical influences of the internal liquid on the structural eigenfrequencies and their associated modal shapes. The computational reduced-order basis is calculated by solving the generalized eigenvalue problems presented in Section 2.5.

In this Section, some elastic, acoustic, and sloshing-capillarity eigenmodes are represented with their respective eigenfrequencies denoted by $\nu_i^a = \sqrt{\lambda_i^a}/2\pi$, for $i = 1, \ldots, N_a$ with $a \in \{p, h, u\}$.

6.2.2.1 Acoustic eigenmodes

Figure 6.4 displays some acoustic eigenmodes of the liquid with their respective eigenfrequencies. It should be noted that the fundamental frequency of the internal liquid is $\nu_1^p = 5\,194\,Hz$.

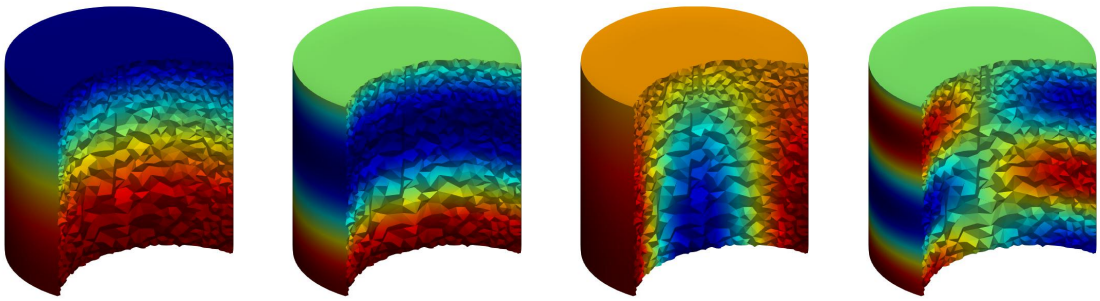

$\nu_1^p = 5\,194\,Hz$ $\nu_4^p = 15\,581\,Hz$ $\nu_9^p = 24\,240\,Hz$ $\nu_{15}^p = 28\,327\,Hz$

Figure 6.4 – Example of acoustic modes of the liquid

6.2.2.2 Sloshing eigenmodes

Figure 6.5 (upper figure) displays some sloshing modes of the liquid free surface taking into acount the capillarity effects. It is shown that the fundamental frequency of the free surface is $\nu_1^h = 3.44\,Hz$, that is of order 10^3 smaller than the fundamental frequency of the internal liquid. Moreover, one can see that the modal density of the sloshing phenomena is significant since $\nu_{107}^h = 19.67\,Hz$. The acoustic part of the sloshing eigenmodes in the liquid are displayed in Figure 6.5 (lower figure), for which we can see that the pressure exponentially decreases with respect to the depth of the liquid, as it was expected.

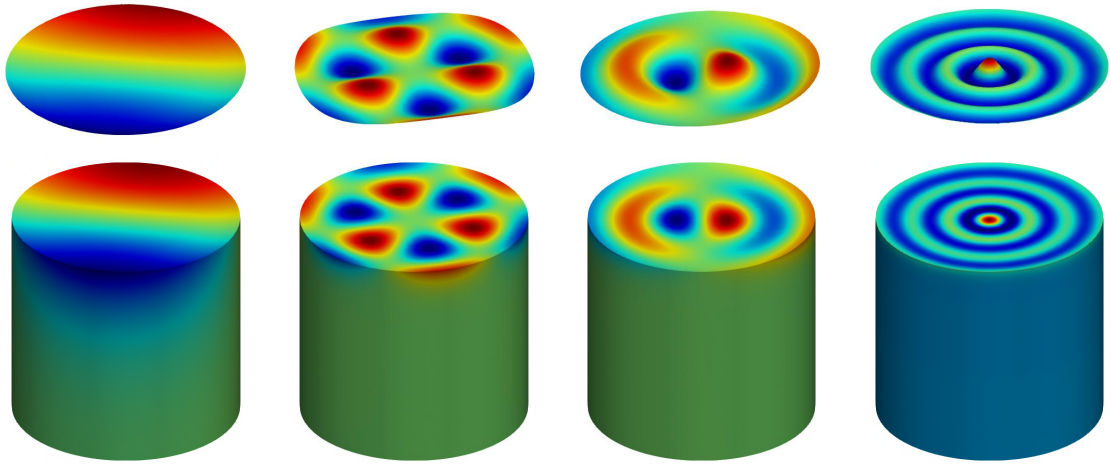

$\nu_1^h = 3.44\,Hz$ $\nu_{20}^h = 8.28\,Hz$ $\nu_{25}^h = 8.71\,Hz$ $\nu_{107}^h = 19.67\,Hz$

Figure 6.5 – Example of 4 sloshing eigenmodes of the free surface (top) and the corresponding pressure in the acoustic liquid (bottom).

6.2.2.3 Elastic eigenmodes

The geometry of the structure has preliminarily been updated in order to match, for the best, the experimentally measured eigenfrequencies. Figure 6.6 quantifies this updating and displays the graph of the elastic eigenfrequencies of the empty cylinder (which will be called *dry eigenfrequencies* in the following) with respect to the longitudinal and circumferential wave numbers m and n. The updated computed dry eigenfrequencies are displayed in blue solid line and the experimental ones [73] in red triangles. It should be noted that all computations have been performed

on the 3D computational model and that the longitudinal and circumferential wave numbers of the elastic eigenmodes have been identified from examining the 3D plots of the eigenmodes. One

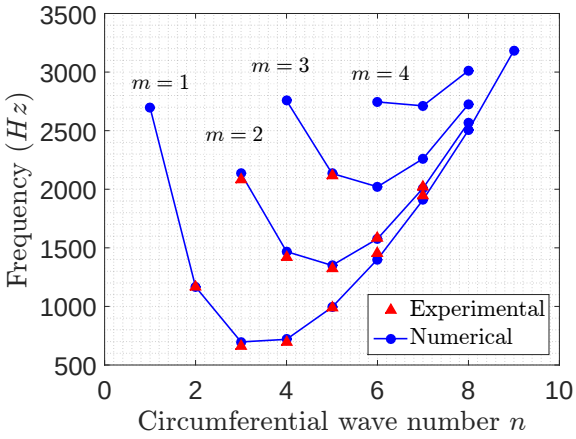

Figure 6.6 – Graph of the elastic dry eigenfrequencies calculated with the updated computational model (blue solid line) compared to the experimental dry eigenfrequencies (red triangles).

can see that the updated computational model correctly fits the experimental eigenfrequencies. Figure 6.7 displays four elastic dry eigenmodes (*i.e.* without taking into account the influence of the internal liquid) of the structure respectively of rank 6, 12, 22, and 44 for which the associated longitudinal wave numbers are $m = 1$, $m = 1$, $m = 2$, and $m = 3$, and the associated circumferential wave numbers are $n = 4$, $n = 5$, $n = 7$, and $n = 4$. Figure 6.8 displays the corresponding four elastic *wet eigenmodes* of the structure (*i.e.* taking into account the influence of the internal liquide through the added mass effect) partially filled with 30% water. It is shown that the presence of the liquid locally modifies the modal shape of the elastic eigenmodes in the spatial area where the liquid is in contact with the cylinder shell. In addition, a decrease of the elastic eigenfrequencies is observed, which is confirmed by the experimental results.

6.2.3 Dynamical excitation of the system

The dynamical excitation is a time-dependent force for which its Fourier transform is a constant in the frequency band of excitation $\mathbb{B}_e = [\nu_{min}\,,\,\nu_{max}]\,Hz$, with $\nu_{min} = 500\,Hz$ and $\nu_{max} = 2{,}500\,Hz$. The nonlinear responses is computed in the time domain. The Fourier transform of the time response allows for obtaining the response in the frequency domain. The external load vector, which is denoted by $\mathbf{F}_u$, is written as

$$\mathbf{F}_u = \alpha\, g(t)\, \mathbf{F} \quad , \tag{6.1}$$

in which α is the intensity coefficient taken as $\alpha = 4$, $g(t)$ is the time function of the dynamical excitation, and $\mathbf{F}$ is the normalized vector representing the spatial distribution of the external time load. The excitation is located on a small rectangular patch that is radially oriented (see the red patch in Figure 6.2 left). In Eq. (6.1), the time signal $g(t)$ is the one defined by Eq. (5.8). Therefore, the Fourier transform of $g(t)$ is written as

$$\widehat{g}(2\pi\nu) = \mathbb{1}_{\mathbb{B}_e \cup \underline{\mathbb{B}}_e}(\nu) \quad , \tag{6.2}$$

$\nu^u_6 = 993\,Hz$ $\nu^u_{12} = 1\,402\,Hz$ $\nu^u_{22} = 2\,008\,Hz$ $\nu^u_{44} = 2\,757\,Hz$

Figure 6.7 – Example of 4 "dry" elastic eigenmodes modes.

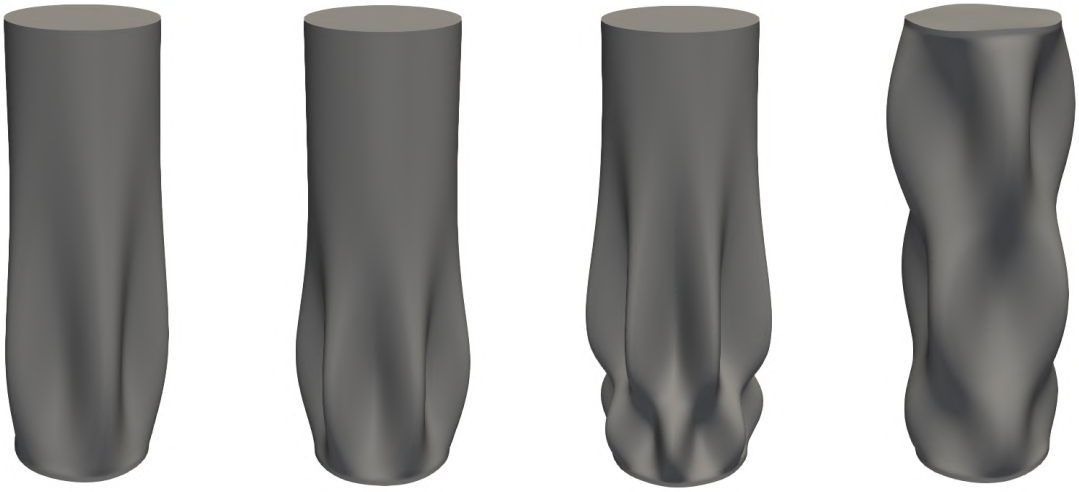

$\nu^u_6 = 683\,Hz$ $\nu^u_{10} = 875\,Hz$ $\nu^u_{30} = 1\,792\,Hz$ $\nu^u_{40} = 2\,133\,Hz$

Figure 6.8 – Example of the 4 corresponding "wet" elastic eigenmodes of the structure (*i.e.* with added mass effect).

which is 1 if $\nu \in \mathbb{B}_e$ and 0 if $\nu \in \mathbb{R}^+ \backslash \mathbb{B}_e$. The main computational difficulty is to well capture the sloshing of the free surface that is a low-frequency phenomenon. In addition, the low damping of the surface sloshing (resulting from indirect damping by coupling with the dissipative liquid and with the dissipative structure) induces a very long time for returning to the equilibrium position, yielding a significant computational cost. The computation is carried out on a truncated time domain $[t_{ini},\, t_{ini} + T]$ with a long time duration T for which $t_{ini} = -1.28\,s$ and $T = 21\,s$. The sampling frequency and the number of time steps are chosen as $\nu_e = 25\,000\,Hz$ and $N_t = 524\,288$. Once the time response has been computed, a Fourier transform is performed to analyze the frequency response of the system in the frequency band of analysis $\mathbb{B}_a = [0,\, 6\,000]\,Hz$.

6.2.4 Eigenfrequency characterization of the system

Physically there are sloshing modes in the frequency band of excitation Be but their contributions in this band $\mathbb{B}_e$ are negligible. Consequently, only the sloshing modes whose eigenfrequencies are below $500\,Hz$ are kept for constructing the ROM. Note that the sloshing eigenfrequencies increase at a very slow rate since $\nu^h_{500} = 57.78\,Hz$. The first acoustic mode has an eigenfrequency $\nu^p_1 = 5{,}194\,Hz$ greater than the upper bound $2\,500\,Hz$ of $\mathbb{B}_e$. Note that only the first acoustic eigenfrequency belongs to $\mathbb{B}_a$ since the second acoustic eigenfrequency is $\nu^p_2 = 12\,504\,Hz$. Consequently, only the structural modes occur in the frequency band of the excitation. The eigenfrequency characterization of the fluid–structure system is summarized in Figure 6.9. It should be noted that, in the reduced-order model, all the elastic modes have been taken into account in the frequency band: the structural modes $n = 0$ and all the modes $n \geq 1$ for which their eigenfrequencies have a multiplicity greater that one (due to geometrical symmetries). The rank of the first $n = 0$ dry elastic mode is 89 and its associated eigenfrequency is $4\,509\,Hz$. The rank of the corresponding wet elastic mode (with the added mass effects) is 32 and its associated eigenfrequency is $1\,852\,Hz$ (important shift due to the added mass). Thus, it can be seen that this first $n = 0$ elastic mode belongs to the frequency band of excitation. There is no other $n = 0$ wet elastic eigenmode whose rank is less than or equal to 100.

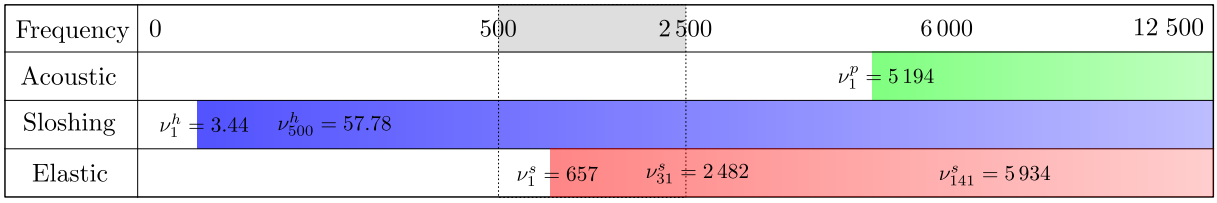

Figure 6.9 – Table of the modal characterization of the fluid-structure system.

6.2.5 Quantities of interest for analyzing the results in the time and frequency domains

6.2.5.1 Observation points

The dynamical response of the fluid-structure system is analyzed for different observation points of the finite element mesh. These observations points are chosen to be of best interest for the dynamical study of the system. Two nodes, denoted $\mathbf{x}^p_1$ and $\mathbf{x}^p_2$, are chosen for the observation of the pressure in the acoustic liquid. A node, common to both the structure and the free surface is chosen on the triple line, which allows for seeing the correspondence between the displacement of the structure and the elevation of the free surface. This common node is denoted as $\mathbf{x}^h_1$ on the free surface, and as $\mathbf{x}^u$ on the structure. Finally, another observation point $\mathbf{x}^h_2$ is also chosen as the point located at the center of the free surface. For the sake of clarity, the coordinates of these observation points are summarized in Table 6.2. In the following, some notations are introduced to lighten the writing. The quantities $P_{\mathbf{x}^p_i}$ and $H_{\mathbf{x}^h_i}$ denote the pressure and the elevation of the free surface at the observation point $\mathbf{x}^p_i$ and $\mathbf{x}^h_i$ for $i = 1, 2$. The notation $U_{x^u_j}$ denotes the component j, $j = \{1, 2, 3\}$, of the structural displacement at the observation point $\mathbf{x}^u$.

Location	Name	x_1-coordinate	x_2-coordinate	x_3-coordinate
Liquid	$\mathbf{x}_1^p$	0.0187	0	0.0076
	$\mathbf{x}_2^p$	0.0187	0	0.0708
Free surface	$\mathbf{x}_1^h$	-0.0144	-0.0347	0.1248
	$\mathbf{x}_2^h$	0	0	0.1245
Structure	$\mathbf{x}^u$	-0.0144	-0.0347	0.1248

Table 6.2 – Coordinates of the observation points for the fluid, the structure and the free surface

6.2.5.2 Defining the quantities of interest

The results are observed on the observation points defined in the Section 6.2.5.1. The quantities of interest are therefore explicited on these observation points and are defined in order to quantify the influence of the geometrical nonlinearities on the resonances levels of the system. In order to quantify the influence of the geometrical nonlinearities on the system, so-called *linear computations* are performed, which consists in solving the numerical problem defined by Eq. (2.76) without taking into account the nonlinear restoring forces (*i.e.* considering $\boldsymbol{\mathcal{F}}_{\mathrm{NL}} = \mathbf{0}$). In the following, the superscripts L and NL denote respectively the quantities calculated for the linear system and for the nonlinear system.

- For the structural displacement, the quantity of interest, dB^U, calculated with both the linear and the nonlinear ROM, is defined as the displacement seen at the point $\mathbf{x}^u$ (see Table 6.2 for its coordinates) and is written as

$$dB_k^{U^{\mathrm{L/NL}}}(2\pi\nu) = 20\log_{10}(\,|\widehat{U}_{x_k^u}^{\mathrm{L/NL}}(2\pi\nu)|\,) \quad , \quad k = 1,2,3 \quad , \tag{6.3}$$

  where subscript k denotes the structural displacement along axis $\mathbf{e}_k$ seen at the observation point $\mathbf{x}^u$.

- For the pressure in the acoustic liquid, the quantity of interest, dB^P, calculated with both the linear and the nonlinear ROM, is defined as the pressure seen at the two observation points $\mathbf{x}_k^p$, $k = 1,2$ (see Table 6.2 for their coordinates) and written as

$$dB_k^{P^{\mathrm{L/NL}}}(2\pi\nu) = 20\log_{10}(\,|\widehat{P}_{\mathbf{x}_k^p}^{\mathrm{L/NL}}(2\pi\nu)|\,) \quad , \tag{6.4}$$

- For the sloshing of the free surface, the quantity of interest dB^H, calculated with both the linear and the nonlinear ROM, is defined as the normal elevation seen at the observation points of coordinates $\mathbf{x}_k^h$, $k = 1,2$ (see Table 6.2 for their coordinates) and written as

$$dB_k^{H^{\mathrm{L/NL}}}(2\pi\nu) = 20\log_{10}(\,|\widehat{H}_{\mathbf{x}_k^h}^{\mathrm{L/NL}},(2\pi\nu)|\,) \quad , \tag{6.5}$$

6.2.6 Convergence of the reduced-order model with respect to the modal truncation

The nonlinear reduced-order model presented in Section 2.5 is constructed using the eigenmodes calculated in Section 6.2.2. A convergence analysis of the nonlinear response is performed with respect to the order of the nonlinear reduced-order model. Since the reference solution cannot be computed for such large finite element system given our computational resources, it is assumed that the convergence is reached when the dynamical response is no longer sensitive to parameters

N_p, N_h or N_u. We choose to normalize the convergence function with respect to a high number of eigenmodes $\overline{N}_p = 200$, $\overline{N}_h = 2{,}250$, and $\overline{N}_u = 100$. Let thus introduce the convergence functions

$$\mathrm{Conv}_U(N_p, N_h, N_u) = \left\{ \frac{\displaystyle\int_{\mathbb{B}_a} \left\| \, dB^{U^{\mathrm{NL}}}(2\pi\nu; N_p, N_h, N_u) \, \right\|^2 d\nu}{\displaystyle\int_{\mathbb{B}_a} \left\| \, dB^{U^{\mathrm{NL}}}(2\pi\nu; \overline{N}_p, \overline{N}_h, \overline{N}_u) \, \right\|^2 d\nu} \right\}^{\frac{1}{2}} , \tag{6.6}$$

$$\mathrm{Conv}_{P_k}(N_p, N_h, N_u) = \left\{ \frac{\displaystyle\int_{\mathbb{B}_a} dB_k^{P^{\mathrm{NL}}}(2\pi\nu; N_p, N_h, N_u)^2 \, d\nu}{\displaystyle\int_{\mathbb{B}_a} dB_k^{P^{\mathrm{NL}}}(2\pi\nu; \overline{N}_p, \overline{N}_h, \overline{N}_u)^2 \, d\nu} \right\}^{\frac{1}{2}} , \tag{6.7}$$

$$\mathrm{Conv}_{H_k}(N_p, N_h, N_u) = \left\{ \frac{\displaystyle\int_{\mathbb{B}_a} dB_k^{H^{\mathrm{NL}}}(2\pi\nu; N_p, N_h, N_u)^2 \, d\nu}{\displaystyle\int_{\mathbb{B}_a} dB_k^{H^{\mathrm{NL}}}(2\pi\nu; \overline{N}_p, \overline{N}_h, \overline{N}_u)^2 \, d\nu} \right\}^{\frac{1}{2}} . \tag{6.8}$$

These convergence analyses are displayed in Figure 6.10, first with respect to N_p (left figure), then with respect to N_h (right figure), and finally with respect to N_u (bottom figure).

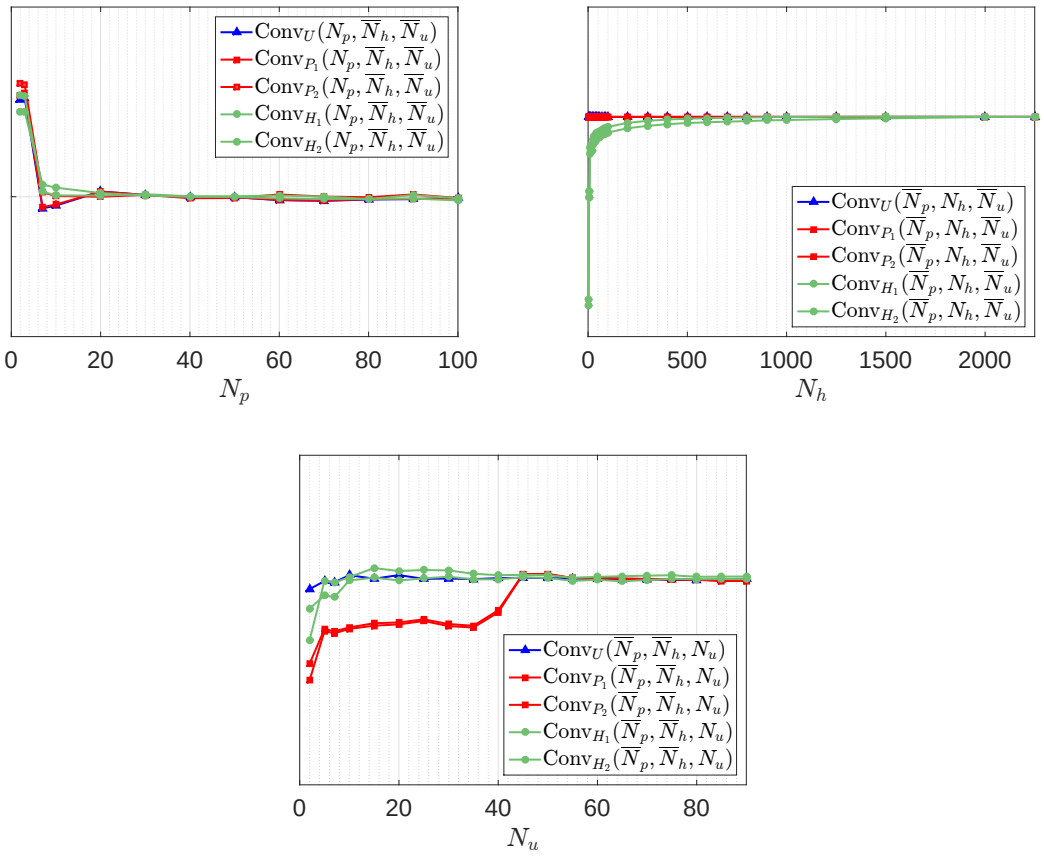

Figure 6.10 – Graph of the convergence of the solutions obtained in terms of **P**, **H**, and **U** at the observation points with respect to N_p (left), to N_h (right), and to N_u (bottom).

It is shown that the convergence analysis yields an optimal size of the ROM of $N_u = 60$, $N_p = 40$, and $N_h = 1\,500$. It should be noted that the large number of sloshing eigenmodes required for the convergence of the solution is due to the high modal density of the sloshing phenomenon.

6.3 Explaining the experimental unexpected sloshing phenomenon by the simulations

6.3.1 Dynamical responses of the fluid-structure system

In this section the results issued from the linear and nonlinear simulations are presented. The linear dynamical responses are displayed in blue solid line and the nonlinear dynamical responses are displayed in red solid line in the following analysis. Figure 6.11 displays the graphs of $\nu \mapsto dB_k^{P^{\mathrm{L/NL}}}(2\pi\nu)$ for $k = 1, 2$. First, one can see that numerous resonances arise outside the excitation frequency band $\mathbb{B}_e$ due to the structural nonlinearities. The contributions of most of the elastic modes located above $2\,500\,Hz$ appear in both nonlinear responses. On the other hand, below $500\,Hz$ and for these two pressure observation points, the sloshing modes are not detected due to the exponential decreasing of the sloshing-induced pressure with the depth. In addition, for the nonlinear responses, the resonance peaks located inside $\mathbb{B}_e$ are largely spread out with respect to the ones obtained by the linear responses. This is the case, for example, for the resonance located at $2\,089\,Hz$. For $k = 1, 2, 3$, Figure 6.12 displays the graph

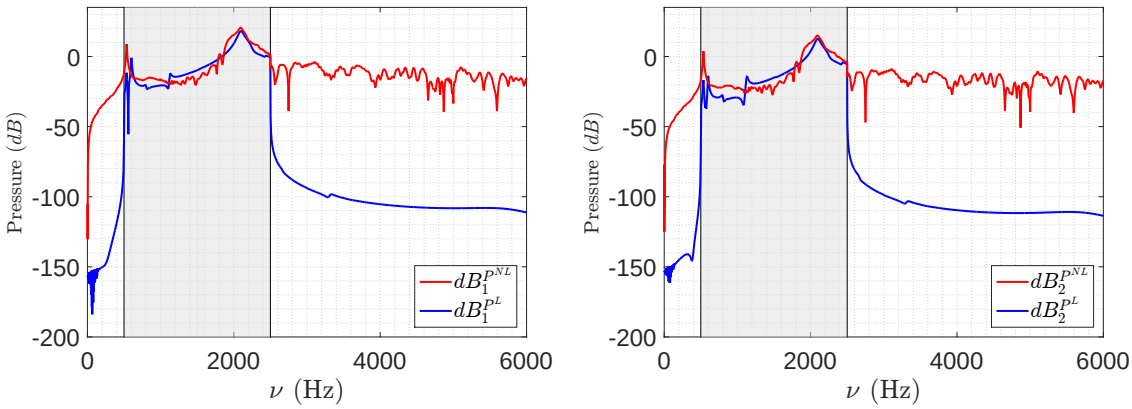

Figure 6.11 – Nonlinear analysis of the pressure in the internal liquid: graphs of $\nu \mapsto dB_1^{P^{\mathrm{L/NL}}}(2\pi\nu)$ (left figure) and $\nu \mapsto dB_2^{P^{\mathrm{L/NL}}}(2\pi\nu)$ (right figure).

of $\nu \mapsto dB_k^{U^{\mathrm{L/NL}}}(2\pi\nu)$. One can see that some sloshing modes below $500\,Hz$ contribute to the structural displacements. The structural nonlinearities strongly modify the frequency responses in excitation band $\mathbb{B}_e$: the resonance peaks are not only spread out, as for the acoustic pressures, but they are also less isolated and less acute. This is due to the fact that the energy of the responses in the frequency band $\mathbb{B}_e$ is partially transferred outside this band, yielding an apparent damping by this transfer of mechanical energy. The dynamical behavior of the structure is thus significantly damped as it can be seen that the resonances levels inside $\mathbb{B}_e$ are strongly reduced by a factor up to 100. Note that the frequency spreading effect is again observed for the resonance located at $872\,Hz$. Figure 6.13 displays the graphs of $\nu \mapsto dB_k^{H^{\mathrm{L/NL}}}(2\pi\nu)$ for $i = 1, 2$. The unexpected response in frequency band $[0, 150]\,Hz$ (below the excitation band $\mathbb{B}_e$) is observed.

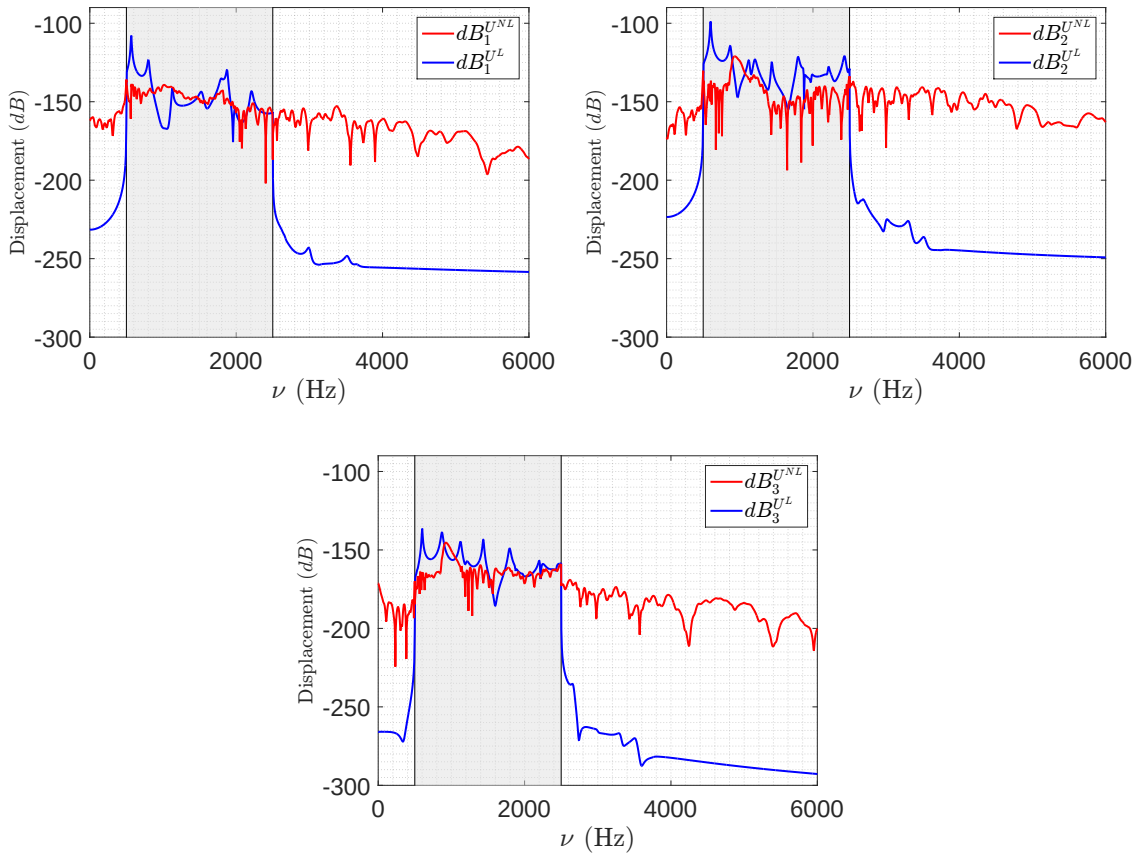

Figure 6.12 – Nonlinear analysis of the displacement of the structure: graphs of $\nu \mapsto dB_1^{U^{\mathrm{L/NL}}}(2\pi\nu)$ (left figure), $\nu \mapsto dB_2^{U^{\mathrm{L/NL}}}(2\pi\nu)$ (right figure), and $\nu \mapsto dB_3^{U^{\mathrm{L/NL}}}(2\pi\nu)$ (lower figure).

The first sloshing modes are excited by the energy transferred in this band $[0, 150]\,Hz$ due to the structural nonlinearities. Let us note that, for the same reasons as the ones given for the structural displacements, an apparent damping by a factor up to 100 occurs in excitation band $\mathbb{B}_e$. When zooming in the sub-frequency band $[0, 150]\,Hz$, as displayed in Figure 6.14, one can see that numerous isolated sloshing resonances of high amplitude appear. It is essential to underline that there is a high-amplitude low-frequency free-surface motion while no external excitation exists in this very low-frequency band. The experimental results presented in [73, 3], concerning the unexpected free-surface elevation of liquid in a vibrating cylindrical shell, have been reproduced in the present work that clearly exhibits the same unexpected phenomena. The understanding of such complex mechanisms requires to quantify the influence of the different coupling operators involved in the dynamical behavior of the free surface. These investigations have been performed by computationally quantifying the influence of the coupling operator $[C_{hu}]$ in this fluid-structure system. As shown in Chapter 5, the influence of $[C_{hu}]^T$ is directly related to the local curvature of the free surface and to the capillary contact angle at the triple line. As a consequence, the dynamical response of the free surface is weakly sensitive to the coupling operator $[C_{hu}]$. Therefore, it can be concluded that the energy issued from the structural nonlinearities follows a path going from the structure to the free surface via the acoustic internal liquid. The complete analysis of this phenomenon is presented in [12] and detailed in Section 6.3.2.

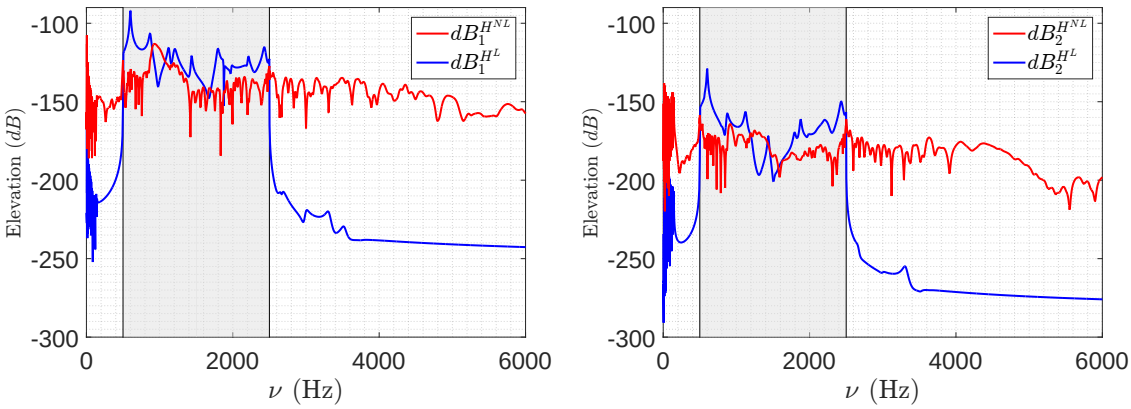

Figure 6.13 – Nonlinear analysis of the free surface elevation: graphs of $\nu \mapsto dB_1^{H^{\mathrm{L/NL}}}(2\pi\nu)$ (left figure) and $\nu \mapsto dB_2^{H^{\mathrm{L/NL}}}(2\pi\nu)$ (right figure).

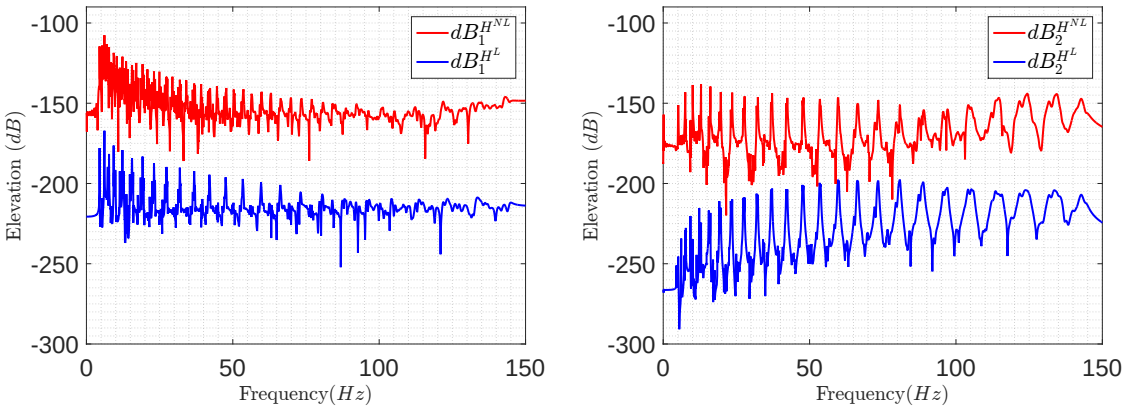

Figure 6.14 – Nonlinear analysis of the free surface elevation: graphs of $\nu \mapsto dB_1^{H^{\mathrm{L/NL}}}(2\pi\nu)$ (left figure) and $\nu \mapsto dB_2^{H^{\mathrm{L/NL}}}(2\pi\nu)$ (right figure) displayed over the frequency band $[0, 150]\,Hz$.

6.3.2 Indirect coupling mechanism

Considering the numerical results presented in Section 6.3.1, it appears that the high-amplitude motion of the free surface in the very-low frequency band (outside the frequency band of excitation) can be explained by the the couplings illustrated in Figure 6.15 and detailed hereinafter. The geometrical nonlinearities of the structure induce a transfer of the vibrational energy from the high-frequency band of excitation in the very low- and low-frequency band (outside the frequency band of excitation). As the first acoustic modes of the liquid is greater than the upper bound of the high-frequency band of excitation, the acoustic fluid has a quasistatic behavior in the low-frequency band. Therefore, the energy transferred by the structure in the very low-frequency band is transmitted through the acoustic liquid to the first very low-frequency sloshing modes. This means that the observed phenomenon appears to be an *indirect* transfer of energy from the structure to the free surface through the acoustic liquid and is due to the presence of the geometrical nonlinearity of the elastic tank.

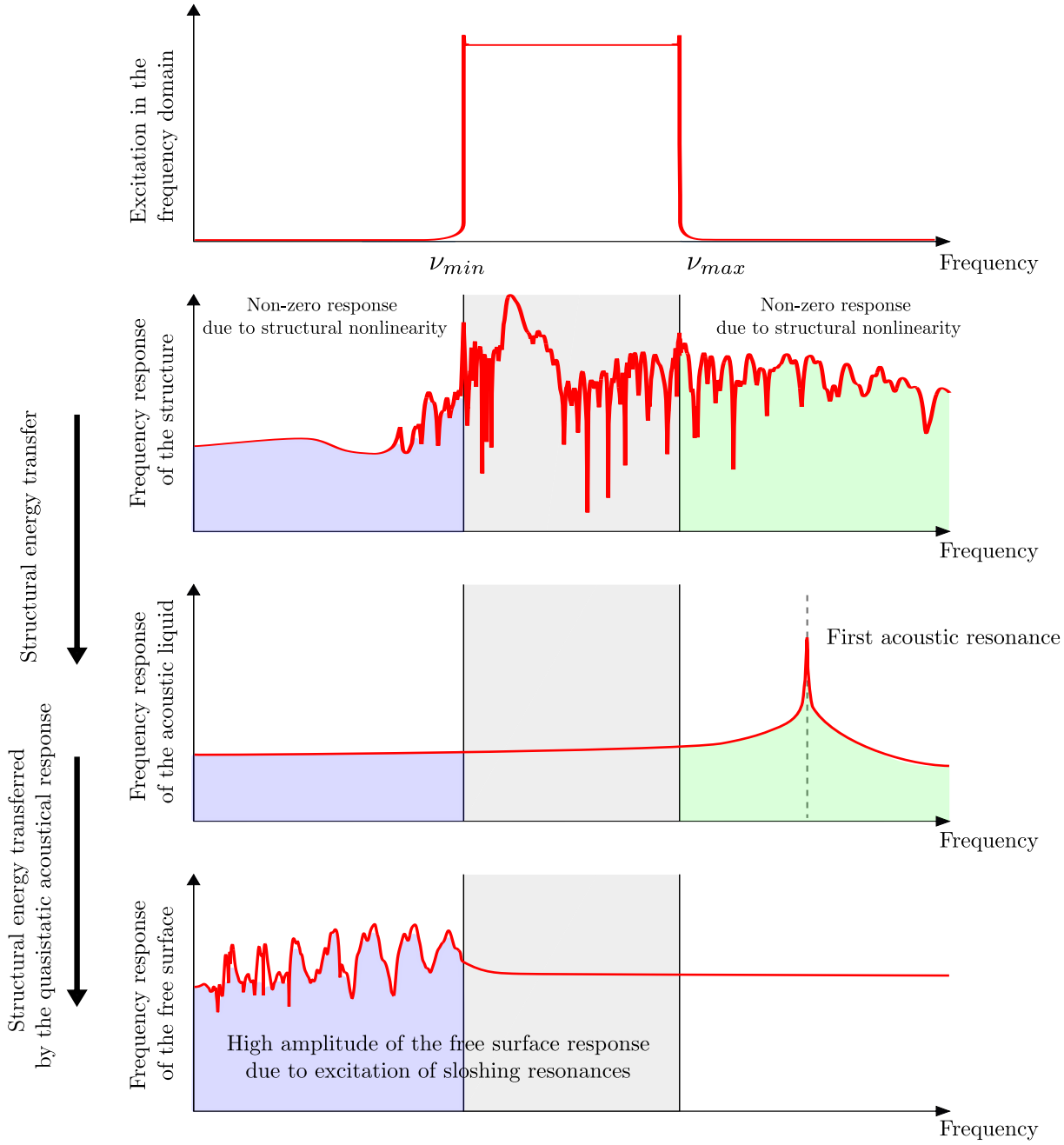

Figure 6.15 – Scheme of the energy transfers between the nonlinear structure, the linear acoustic liquid, and the linear free surface, which explain the excitation of the first sloshing modes in the very-low frequency band (outside the frequency band of the external excitations).

Chapter 7

Uncertainty quantification for coupled fluid-structure systems

Contents

7.1 Introduction

7.1.1 General introduction

The objective of the chapter is to implement in the computational model defined by Eqs. (2.63) to (2.65) a probabilistic model of uncertainties for the structural stiffness forces in order to analyze the robustness of the responses of the nonlinear dynamical system to these uncertainties. In this work, we are interested in the structural modeling errors inducing model uncertainties. Consequently, we use the nonparametric probabilistic approach [99, 102] that has the capability to take into account this type of uncertainties. In order to facilitate the reading of this chapter, we give a brief recall of the useful tools on which the nonparametric probabilistic approach of uncertainties is based.

7.1.2 Brief recall on the nonparametric probabilistic approach of uncertainties

In the nonparametric probabilistic approach of uncertainties, the uncertainties are taken in account by substituting deterministic matrices of the ROM by random matrices yielding a stochastic reduced-order model (SROM). The probability distributions and the generators of independent realizations of random matrices that are used are constructed using the ensembles of random matrices introduced in [99, 102].

(i) - Ensemble SG_0^+ *and its generator*

An element of ensemble SG_0^+ is the random matrix $[\mathbb{G}_0]$ whose probability density function is defined by

$$p_{[\mathbb{G}_0]}([G]) = \mathbb{1}_{\mathbb{M}_m^+}([G])\ c_0(\det[G])^{c_1} \exp\{-c_2\,\mathrm{Tr}([G])\} \quad , \tag{7.1}$$

in which c_0 the positive constant of normalization, where $c_1 = (m+1)(1-\delta^2)/(2\delta^2)$, and where $c_2 = (m+1)/(2\delta^2)$ depend on dimension m and on a hyperparameter $\delta \in [0\,,\,\delta_{\max}[$. Such a random matrix $[\mathbb{G}_0]$ admits the following algebraic representation that can be used as a generator of independent realizations,

$$[\mathbb{G}_0] = [\mathbb{L}]^T\,[\mathbb{L}] \quad , \tag{7.2}$$

in which $[\mathbb{L}]$ is an upper triangular $(m \times m)$ random matrix such that:

- random variables $\{[\mathbb{L}]_{jj'}, j \leq j'\}$ are independent.
- For $j < j'$, the real-valued random variable $[\mathbb{L}]_{jj'}$ is written as $[\mathbb{L}]_{jj'} = \sigma_m\, A_{jj'}$ in which $\sigma_m = \delta(m+1)^{-1/2}$ and where $A_{jj'}$ is a real-valued Gaussian random variable with zero mean and variance equal to 1.
- For $j = j'$, the positive-valued random variable $[\mathbb{L}]_{jj}$ is written as $[\mathbb{L}]_{jj} = \sigma_m\sqrt{2B_j}$, in which B_j is a positive-valued Gamma random variable with probability density function $\Gamma(a_j, 1)$, in which $a_j = \frac{m+1}{2\delta^2} + \frac{1-j}{2}$.

(ii) - Ensemble SE_0^+ *of random matrices*

Let $[A]$ be a deterministic positive-definite matrix representing the given mean value. SE_0^+ is the ensemble of positive-definite random matrices such that any positive-definite random matrix $[\mathbb{A}_0]$ in SE_0^+ satisfies

$$E\{[\mathbb{A}_0]\} = [A] \quad , \quad E\{\mathrm{Log}(\det([\mathbb{A}_0]))\} = \nu_{[\mathbb{A}_0]} \quad , \quad \nu_{[\mathbb{A}_0]} < +\infty \quad . \tag{7.3}$$

Random matrix $[\mathbb{A}]$ can then be written as

$$[\mathbb{A}_0] = [L_A]^T\,[\mathbb{G}_0]\,[L_A] \quad , \quad [\mathbb{G}_0] \in \mathrm{SG}_0^+ \quad , \tag{7.4}$$

in which $[A] = [L_A]^T\,[L_A]$ is the Cholesky factorization of $[A]$. The positive parameter δ is the hyperparameter of the probability distribution of random matrix $[\mathbb{G}_0]$, which is such that

$$\delta = \left\{ \frac{1}{m} E\{ \| \,[\mathbb{G}_0] - [I_m]\, \|_F^2 \} \right\}^{\frac{1}{2}} \quad , \tag{7.5}$$

and which allows the dispersion of matrix $[\mathbb{G}_0]$ to be controlled. The hyperparameter δ must be such that $0 \leq \delta \leq \delta_{\max} = (m+1)^{\frac{1}{2}}(m+5)^{-\frac{1}{2}}$.

(iii) - Ensemble $\mathrm{SE}_\varepsilon^+$ *of random matrices*

For fixed $\varepsilon > 0$, any random matrix $[\mathbb{A}]$ in $\mathrm{SE}_\varepsilon^+$ is a random matrix with values in $\mathbb{M}_n^+$, which is written as

$$[\mathbb{A}] - [A_\ell] = \frac{1}{1+\varepsilon}[\mathbb{A}_0] > 0 \quad \text{a.s.} \quad \text{with} \quad [\mathbb{A}_0] \in \mathrm{SE}_0^+ \,, \tag{7.6}$$

where $[A_\ell] \in \mathbb{M}_m^+$ is the positive-definite lower bound that is presently defined by

$$[A_\ell] = c_\varepsilon\,[A] \quad \text{with} \quad c_\varepsilon = \frac{\varepsilon}{1+\varepsilon}\,. \tag{7.7}$$

Consequently, $E\{[\mathbb{A}]\} = [A]$. If $\varepsilon = 0$, then ensemble $\mathrm{SE}_\varepsilon^+$ coincides with SE_0^+. For $\varepsilon > 0$, this ensemble allows for introducing a positive-definite lower bound $[A_\ell]$ that is arbitrarily constructed for the case where it is known that a lower bound exists but for which there are no available information for identifying it. That is the case considered here and ε will be chosen as 10^{-6} in the application. The generator of independent realization of $[\mathbb{A}]$ in $\mathrm{SE}_\varepsilon^+$ is then deduced from the one presented for SG_0^+.

7.2 Nonparametric stochastic computational model

This section is devoted to the construction of the stochastic nonlinear reduced-order computational model for the fluid-structure system using the nonparametric probabilistic approach (for details, see [102, 14, 13]).

7.2.1 Hypotheses for the stochastic nonlinear reduced-order model

The considered computational fluid-structure system is the one presented in Chapter 6 for which the deterministic coupling mechanism has been analyzed. We use the nonlinear reduced-order computational model presented in Section 2.5. The uncertainty quantification for this system will make it possible to quantify the uncertainties propagated in the fluid-structure system by the different coupling mechanisms. The main source of uncertainty is due to the elastic structure for which geometrical nonlinearities are taken into account. For such a slender and thin-wall structure, the model uncertainties on the stiffness can be significant. Especially when geometrical nonlinearities are taken into account due to the sensitivity of the quadratic and cubic terms in the nonlinear restoring forces. This is why, in the following, we are interested in constructing a stochastic reduced-order model (SROM) in which the linear and nonlinear stiffness forces are uncertain and for which the nonparametric probabilistic approach is used.

7.2.2 Stochastic nonlinear reduced-order computational model

The stochastic nonlinear reduced-order computational model is written as

$$\begin{bmatrix} \mathbb{P}(t) \\ \mathbb{H}(t) \\ \mathbb{U}(t) \end{bmatrix} = \begin{bmatrix} [\Phi_p] & [\Phi_{ph}] & 0 \\ 0 & [\Phi_h] & 0 \\ 0 & 0 & [\Phi_u] \end{bmatrix} \begin{bmatrix} \mathbb{Q}^p(t) \\ \mathbb{Q}^h(t) \\ \mathbb{Q}^u(t) \end{bmatrix} = [\Psi]\,\mathbb{Q}(t) \quad , \tag{7.8}$$

in which, for all time t, the random vector $\mathbb{Q}(t)$ is solution of the following stochastic nonlinear differential equation

$$[\mathcal{M}_{\text{FSI}}]\,\ddot{\mathbb{Q}}(t) + [\mathcal{D}_{\text{FSI}}]\,\dot{\mathbb{Q}}(t) + [\mathbb{K}_{\text{FSI}}]\,\mathbb{Q}(t) + \mathbb{F}_{\text{NL}}(\mathbb{Q}(t)) = \boldsymbol{\mathcal{F}}(t) \quad . \tag{7.9}$$

In Eq. (7.9) $[\mathbb{K}_{\text{FSI}}]$ and $\mathbb{F}_{\text{NL}}(\mathbb{Q})$ denote respectively the $(N_{phu} \times N_{phu})$ random linear stiffness matrix and the $\mathbb{R}^{N_{phu}}$ random vector of nonlinear restoring forces. The random linear fluid-structure stiffness matrix $[\mathbb{K}_{\text{FSI}}]$ can be expressed by blocks (see Appendix A) as

$$[\mathbb{K}_{\text{FSI}}] = \begin{bmatrix} [\mathcal{K}_{11}] & [\mathcal{K}_{12}] & [0] \\ [\mathcal{K}_{21}] & [\mathcal{K}_{22}] & [\mathcal{K}_{23}] \\ [\mathcal{K}_{31}] & [\mathcal{K}_{32}] & [\mathbb{K}_{33}] \end{bmatrix} \quad , \tag{7.10}$$

in which $[\mathbb{K}_{33}] \in \text{SE}_\varepsilon^+$ is the random counterpart of matrix $[\mathcal{K}_{33}]$. The random vector $\mathbb{F}_{\text{NL}}$ is expressed as a function of the random quadratic and cubic stiffness tensors, $\mathbb{K}^{(2)}$ and $\mathbb{K}^{(3)}$, such that

$$\{\mathbb{F}_{\text{NL}}(\mathbb{Q})\}_\alpha = \mathbb{K}^{(2)}_{\alpha\beta\gamma}\,\mathbb{Q}^u_\beta\,\mathbb{Q}^u_\gamma + \mathbb{K}^{(3)}_{\alpha\beta\gamma\delta}\,\mathbb{Q}^u_\beta\,\mathbb{Q}^u_\gamma\,\mathbb{Q}^u_\delta \quad . \tag{7.11}$$

The construction of the random variables $[\mathbb{K}_{33}]$, $\mathbb{K}^{(2)}$, and $\mathbb{K}^{(3)}$ is detailed in Section 7.2.2.1.

7.2.2.1 Probabilistic modeling of random stiffness matrices

The random variables $[\mathbb{K}_{33}]$, $\mathbb{K}^{(2)}$, and $\mathbb{K}^{(3)}$ are statistically dependent. The construction of these random variables is detailed in [78] and is summarized below. Let introduce the following deterministic $(N_{\mathcal{K}} \times N_{\mathcal{K}})$ matrix, with $N_{\mathcal{K}} = N_u(1 + N_u)$

$$[\mathcal{K}] = \begin{bmatrix} [\mathcal{K}_{33}] & [\widehat{\mathcal{K}}^{(2)}] \\ [\widehat{\mathcal{K}}^{(2)}]^T & 2[\mathcal{K}^{(3)}] \end{bmatrix} \quad , \tag{7.12}$$

in which $[\widehat{\mathcal{K}}^{(2)}]$ and $[\mathcal{K}^{(3)}]$ denote respectively the matrices issued from the following reshaping:

$$[\widehat{\mathcal{K}}^{(2)}]_{\alpha B} = \widehat{\mathcal{K}}^{(2)}_{\alpha\beta\gamma}, \quad \text{with} \;\; B = (\beta - 1)N_u + \gamma \,, \tag{7.13}$$

$$[\mathcal{K}^{(3)}]_{AB} = \mathcal{K}^{(3)}_{\alpha\beta\gamma\delta}, \;\; \text{with} \;\; A = (\alpha - 1)N_u + \beta \;\; \text{and} \;\; B = (\gamma - 1)N_u + \delta \,. \tag{7.14}$$

It is shown in [78] that matrix $[\mathcal{K}]$ is positive definite and can consequently be written as $[\mathcal{K}] = [L_{\mathcal{K}}]^T\,[L_{\mathcal{K}}]$. Thus, the nonparametric probabilistic approach can be applied in the geometrically nonlinear context on matrix $[\mathcal{K}]$, which ensures the statistical dependency of each linear and nonlinear stiffness matrices of the fluid-structure problem. The construction of matrix $[\mathbb{K}]$, random counterpart of $[\mathcal{K}]$, is chosen in ensemble SE_ε^+. However, from a numerical point of view, $\text{SE}_\varepsilon^+ \sim \text{SE}_0^+$ for $\varepsilon = 10^{-6}$. In order to simplify the following algebraic developments, we construct $[\mathbb{K}]$ in SE_0^+.

$$[\mathbb{K}] = [L_{\mathcal{K}}]^T\,[\mathbb{G}_0(\delta)]\,[L_{\mathcal{K}}] \quad . \tag{7.15}$$

in which the random germ $[\mathbb{G}_0(\delta)]$ belongs in the ensemble SG_0^+. The expressions of random variables $[\mathbb{K}_{33}]$, $\widehat{\mathbb{K}}^{(2)}$, and $\mathbb{K}^{(3)}$ are deduced from an extraction of $[\mathbb{K}]$. The random variable $\mathbb{K}^{(2)}$ is then reconstructed from $\widehat{\mathbb{K}}^{(2)}$ similarly to Eq. (2.82). However, it has been shown in [36] that some difficulties can be encountered with this construction, due to the dimension $(N_{\mathcal{K}} \times N_{\mathcal{K}})$ of random matrix $[\mathbb{K}]$. The modification of the stochastic model for $[\mathbb{K}]$, proposed in [36] is used.

The main idea of this formulation is to use another factorization of matrix $[\mathcal{K}]$ by introducing a matrix of size $(\widetilde{N}_{\mathcal{K}} \times N_{\mathcal{K}})$ with $\widetilde{N}_{\mathcal{K}} \ll N_{\mathcal{K}}$. This factorization is calculated by introducing the eigenvalue problem

$$[\mathcal{K}]\,[\Phi_{\mathcal{K}}] = [\Phi_{\mathcal{K}}]\,[\Lambda_{\mathcal{K}}] \quad , \tag{7.16}$$

in which the entries of the diagonal matrix $[\Lambda_{\mathcal{K}}]$ are the eigenvalues λ_α, and where the associated columns of $[\Phi_{\mathcal{K}}]$ are the eigenvectors $\boldsymbol{\varphi}^\alpha_{\mathcal{K}}$. Matrix $[\mathcal{K}]$ can then be approximated by the $(N_{\mathcal{K}} \times N_{\mathcal{K}})$ matrix $[\widetilde{\mathcal{K}}]$ such that

$$[\widetilde{\mathcal{K}}] = [\widetilde{L}]^T\,[\widetilde{L}] \quad , \tag{7.17}$$

in which $[\widetilde{L}]$ is the full $(\widetilde{N}_{\mathcal{K}} \times N_{\mathcal{K}})$ matrix defined by

$$[\widetilde{L}] = [\Lambda^{\widetilde{N}_{\mathcal{K}}}_{\mathcal{K}}]^{\frac{1}{2}}\,[\Phi^{\widetilde{N}_{\mathcal{K}}}_{\mathcal{K}}]^T \quad , \tag{7.18}$$

where $[\Lambda^{\widetilde{N}_{\mathcal{K}}}_{\mathcal{K}}]$ is the $(\widetilde{N}_{\mathcal{K}} \times \widetilde{N}_{\mathcal{K}})$ diagonal eigenvalue matrix such that $[\Lambda^{\widetilde{N}_{\mathcal{K}}}_{\mathcal{K}}]_{\alpha\alpha} = \lambda_\alpha$ sorted by decreasing order $(\lambda_1 \geq \lambda_2 \geq \ldots \geq \lambda_{\widetilde{N}_{\mathcal{K}}})$, and where $[\Phi^{\widetilde{N}_{\mathcal{K}}}_{\mathcal{K}}]$ is the matrix containing the $\widetilde{N}_{\mathcal{K}}$ eigenvectors $\{\boldsymbol{\varphi}^\alpha_{\mathcal{K}}\}_{\alpha=1,\ldots,\widetilde{N}_{\mathcal{K}}}$ associated with eigenvalues λ_α. In order to find the optimal value of $\widetilde{N}_{\mathcal{K}}$, the error fuction $\widetilde{N}_{\mathcal{K}} \mapsto \mathrm{Conv}_{\mathcal{K}}(\widetilde{N}_{\mathcal{K}})$is introduced such that

$$\mathrm{Conv}_{\mathcal{K}}(\widetilde{N}_{\mathcal{K}}) = \sqrt{\frac{\|\,[\widetilde{\mathcal{K}}] - [\mathcal{K}]\,\|^2_F}{\|\,[\mathcal{K}]\,\|^2_F}} \tag{7.19}$$

in which $||\,[\mathcal{K}]\,||_F$ denotes the Frobenius norm of matrix $[\mathcal{K}]$. The order $\widetilde{N}_{\mathcal{K}}$ of the truncature is determined for a given relative error $\varepsilon_{\mathcal{K}}$ such that $\mathrm{Conv}_{\mathcal{K}}(\widetilde{N}_{\mathcal{K}}) \leq \varepsilon_{\mathcal{K}}$. The random matrix $[\mathbb{K}]$ is then replaced by the random matrix $[\widetilde{\mathbb{K}}]$ such that

$$[\widetilde{\mathbb{K}}] = [\widetilde{L}]^T\,[\widetilde{\mathbb{G}}_0(\delta)]\,[\widetilde{L}] + ([\mathcal{K}] - [\widetilde{\mathcal{K}}]) \quad . \tag{7.20}$$

in which $[\widetilde{\mathbb{G}}_0(\delta)]$ is the $(\widetilde{N}_{\mathcal{K}} \times \widetilde{N}_{\mathcal{K}})$ random matrix that belongs to SG^+_0. It should be noted that Eq. (7.20) ensures that matrix $[\widetilde{\mathbb{K}}]$ is almost surely positive-definite.

7.3 Uncertainty sensitivity analysis on the dynamical responses of the fluid-structure system

This section is devoted to the analysis of the uncertainty propagation in the computational fluid-structure system. The stochastic nonlinear reduced model introduced in Section 7.2 allows for taking into account the nonparametric uncertainties in the modeling of the coupled fluid-structure system. The uncertainty sensitivity of the model is analyzed for each part of the system, namely the structure, the internal liquid, and the free surface. In the following sections, we are interested in quantifying the influence of the hyperparameter δ on the 95% confidence interval of the system dynamical responses seen at the observation points. The stochastic solver is based on the Monte-Carlo numerical method for generating the N_r realizations of the random responses. A convergence analysis with respect to N_r is performed in order to ensure the convergence of the confidence region computed for each quantity of interest. The results are presented for both the linear and nonlinear stochastic ROM. For the linear and nonlinear computations, the quantities of interest used in this uncertainty sensitivity analysis are similar to the ones used in Section 6.2.5. The observation points are the ones defined in Table 6.2. The quantities of interest

$dB_1^{P^{\mathrm{L/NL}}}(2\pi\nu)$ and $dB_k^{H^{\mathrm{L/NL}}}(2\pi\nu)$, $(k = 1, 2)$, are related to the pressure in the liquid and to the free-surface elevation (see Eqs. (6.4) and (6.5)). However, the quantity of interest related to the structural displacement is

$$dB^{U^{\mathrm{L/NL}}} = 20\log_{10}\left(\left\|\widehat{\mathbb{U}}_{\mathbf{x}^u}^{\mathrm{L/NL}}(2\pi\nu)\right\|_{\mathbb{C}^3}\right) \quad . \tag{7.21}$$

For each quantity of interest, a confidence region with 95% confidence is estimated. The nominal dynamical response of the quantity of interest, which corresponds to the deterministic computation of the fluid-structure system, is superimposed with the confidence region of the stochastic responses. The numerical parameters used for the computations are similar to the ones described in Section 6.2.3: $\mathbb{B}_e = [500, 2\,500]\,Hz$, $N_t = 65\,536$, $T = 2.63\,s$, $\alpha = 1 \times 10^{-2}$, and $N_r = 256$ (obtained from the convergence analysis). The short time duration T induces a low frequency resolution for the very-low frequency resonances but is necessary to ensure the feasability of the computations (in terms of computational time).

7.3.1 Sensitivity of the structural responses to uncertainties

The sensitivity of the structural responses to uncertainties is shown in Figures 7.1 to 7.3 which display the linear and the nonlinear nominal frequency responses $dB^{U^{\mathrm{L}}}$ and $dB^{U^{\mathrm{NL}}}$, and the associated confidence region, for three values of hyperparameter $\delta \in \{0.05, 0.15, 0.30\}$. It can be seen that uncertainty tends to spread in the high- and low- frequency domains due to energy transfer induced by the geometrical nonlinearities of the structure. The results show a significant, if not a great, sensitivity of the displacements of the structure to structural uncertainties.

7.3.2 Sensitivity of the acoustic liquid to structural uncertainties

The sensitivity of the acoustic liquid to structural uncertainties is presented in Figures 7.4 to 7.6. One can see that the uncertainty propagation in the acoustic liquid is very important both in the linear and in the nonlinear cases. The results of the linear simulations show that the width of the confidence region is significant for a low dispersion rate $\delta = 0.05$, but also that the nominal dynamic response of the system in the frequency band of excitation $\mathbb{B}_e$ tends to exit this confidence region when δ increases. The same phenomenon is visible on nonlinear responses.

7.3.3 Sensitivity of the free-surface sloshing to structural uncertainties

The sensitivity of the free-surface sloshing to structural uncertainties is presented in Figures 7.7 to 7.12 for the observation points $\mathbf{x}_1^h$ and $\mathbf{x}_2^h$. The first observation point $\mathbf{x}_1^h$, located on the triple line, is less sensitive to uncertainties (both in the linear and in the nonlinear computations) than the point $\mathbf{x}_2^h$ located at the center of the free surface. These results suggest that the dynamical sloshing responses of the free surface show an increasing uncertainty sensitivity as one moves furhter from the shell wall. The influence of uncertainties on the indirect coupling mechanism (detailed in Section 6.3) is then analyzed. Figures 7.13 to 7.18 display the frequency responses of points $\mathbf{x}_1^h$ and $\mathbf{x}_2^h$ in the frequency band $[0\,,\,130]\,Hz$. It can be seen that the sloshing resonances, excited by the indirect transfer of energy from the structural nonlinearities, are robust to structural uncertainties.

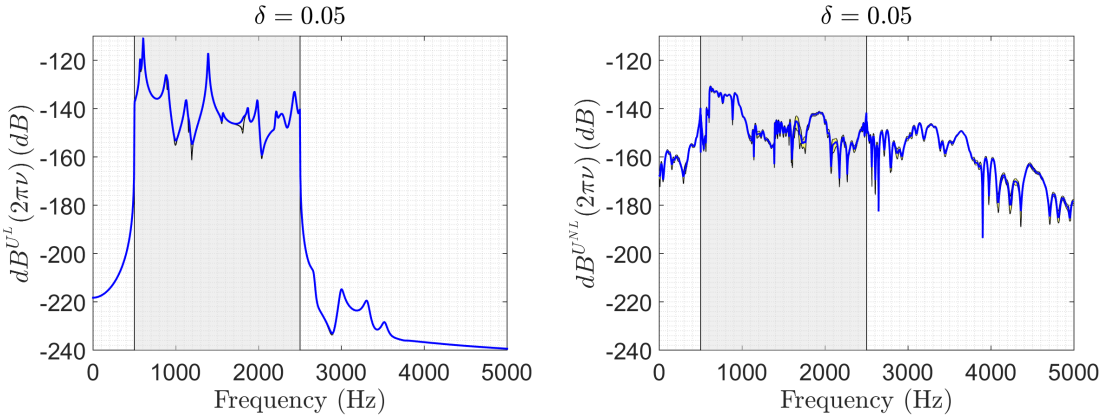

Figure 7.1 – Nominal dynamical responses and confidence regions at 95% of the linear (left figure) and nonlinear (right figure) structural displacement at the observation point $\mathbf{x}^u$ for $\delta = 0.05$.

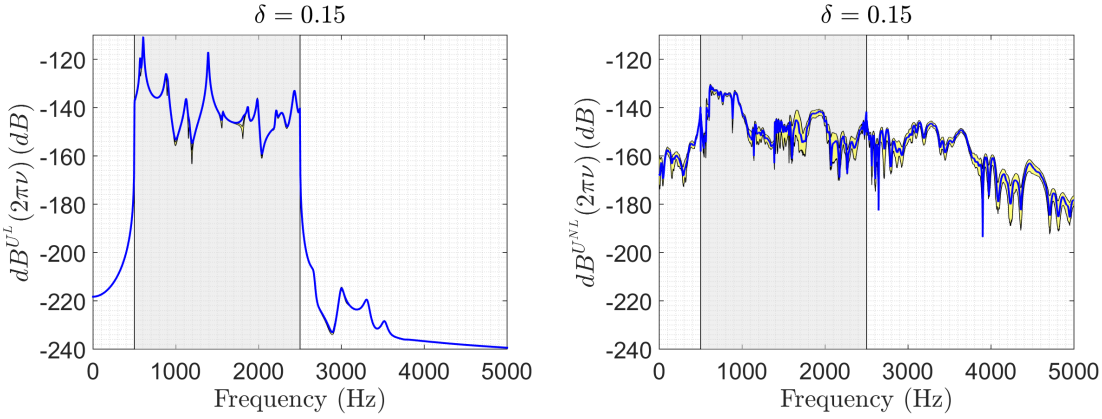

Figure 7.2 – Nominal dynamical responses and confidence regions at 95% of the linear (left figure) and nonlinear (right figure) structural displacement at the observation point $\mathbf{x}^u$ for $\delta = 0.15$.

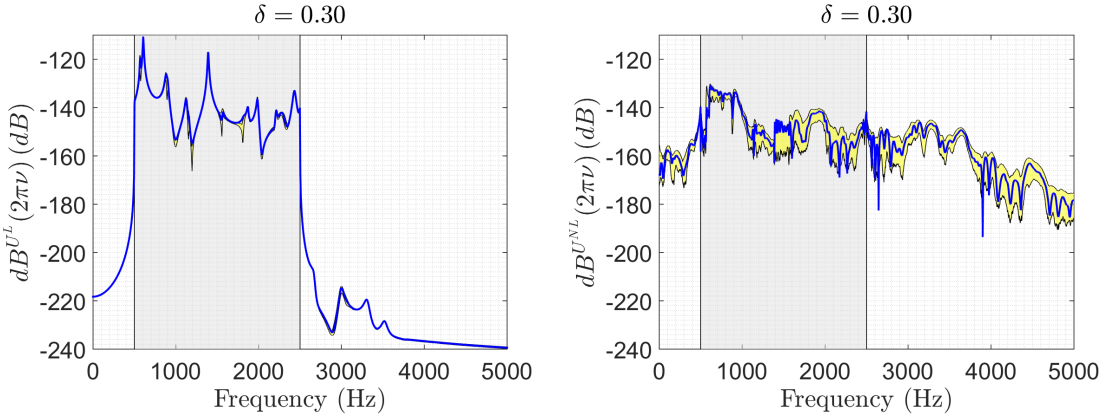

Figure 7.3 – Nominal dynamical responses and confidence regions at 95% of the linear (left figure) and nonlinear (right figure) structural displacement at the observation point $\mathbf{x}^u$ for $\delta = 0.30$.

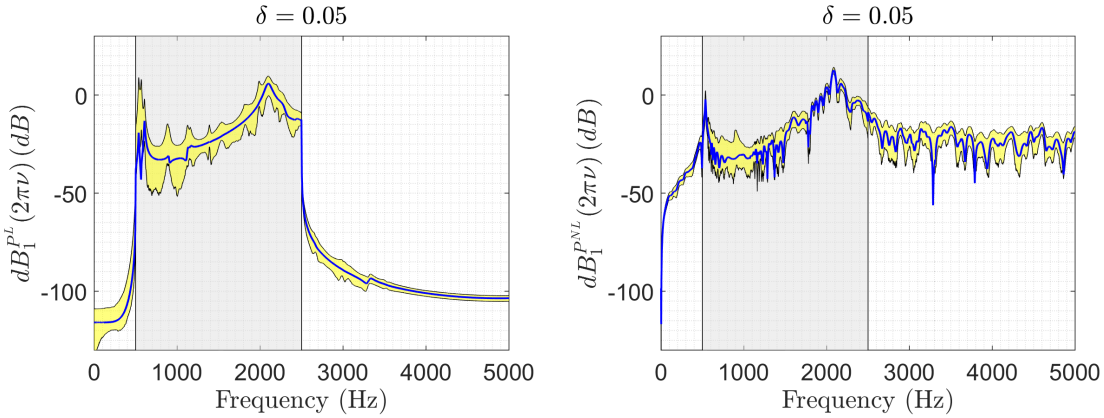

Figure 7.4 – Nominal dynamical responses and confidence regions at 95% of the linear (left figure) and nonlinear (right figure) acoustic pressure at the observation point $\mathbf{x}_1^p$ for $\delta = 0.05$.

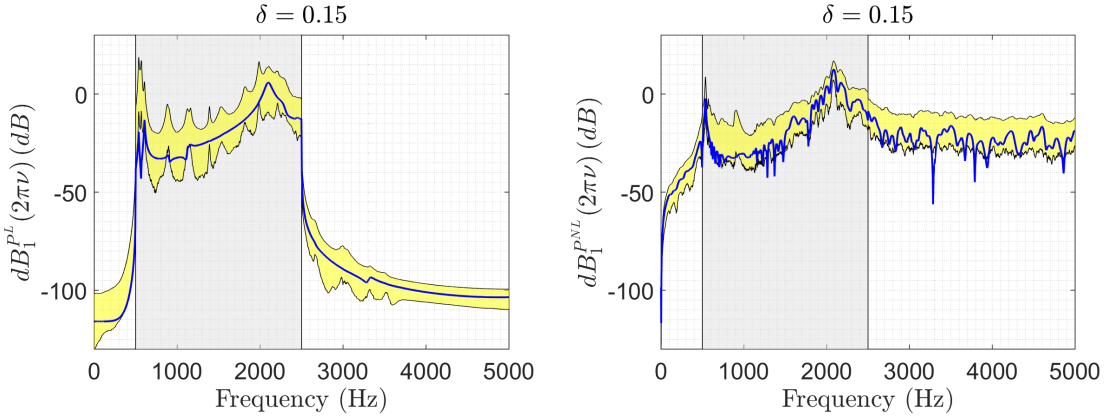

Figure 7.5 – Nominal dynamical responses and confidence regions at 95% of the linear (left figure) and nonlinear (right figure) acoustic pressure at the observation point $\mathbf{x}_1^p$ for $\delta = 0.15$.

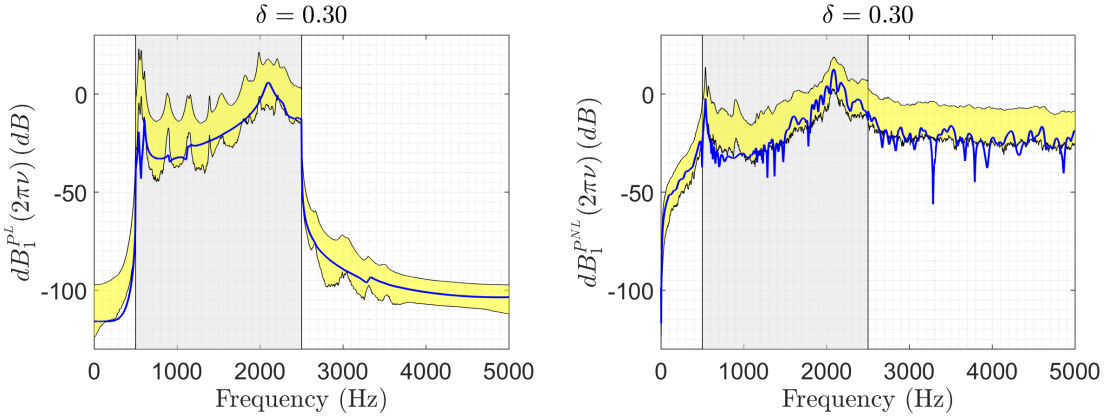

Figure 7.6 – Nominal dynamical responses and confidence regions at 95% of the linear (left figure) and nonlinear (right figure) acoustic pressure at the observation point $\mathbf{x}_1^p$ for $\delta = 0.30$.

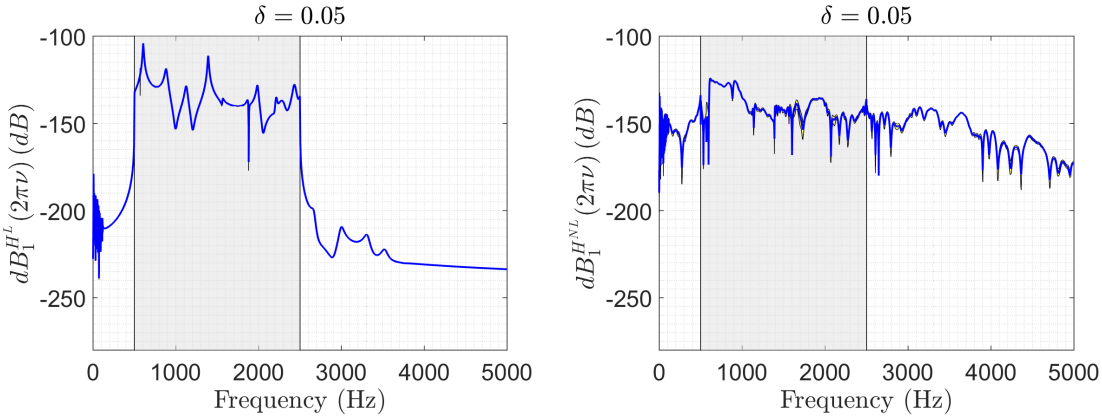

Figure 7.7 – Nominal dynamical responses and confidence regions at 95% of the linear (left figure) and nonlinear (right figure) free-surface elevation at the observation point $\mathbf{x}_1^h$ for $\delta = 0.05$.

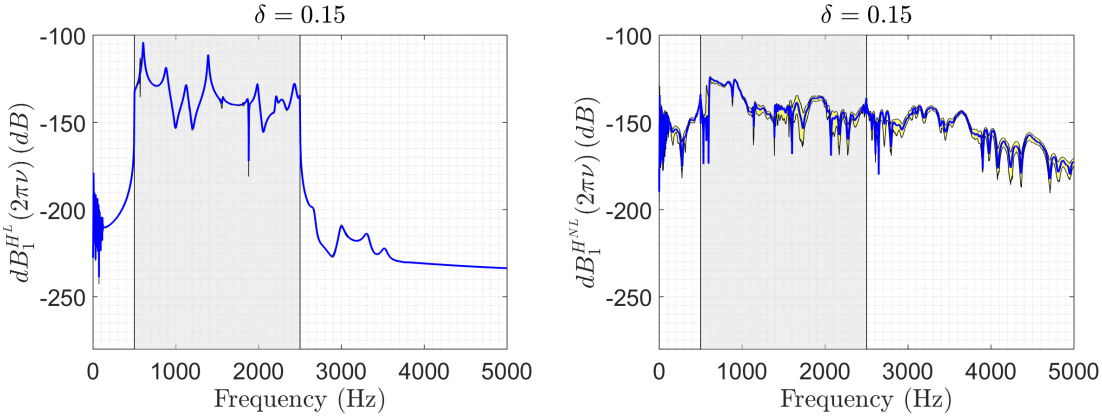

Figure 7.8 – Nominal dynamical responses and confidence regions at 95% of the linear (left figure) and nonlinear (right figure) free-surface elevation at the observation point $\mathbf{x}_1^h$ for $\delta = 0.15$.

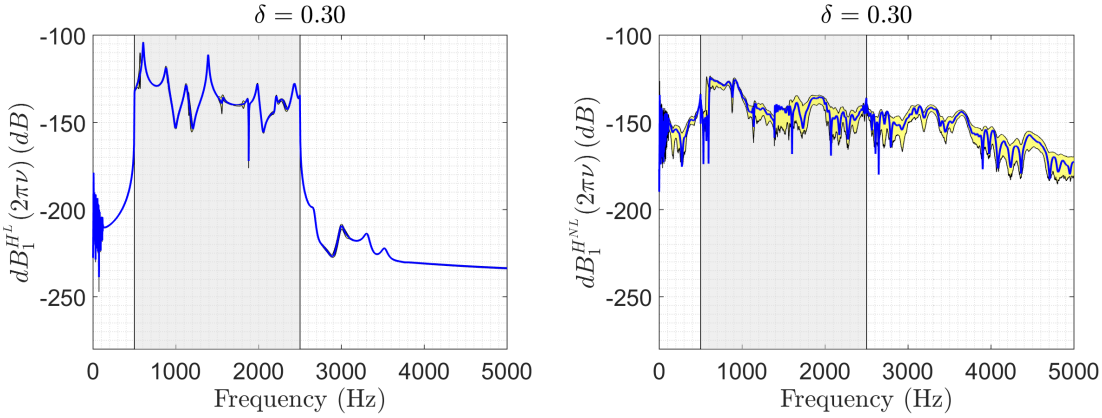

Figure 7.9 – Nominal dynamical responses and confidence regions at 95% of the linear (left figure) and nonlinear (right figure) free-surface elevation at the observation point $\mathbf{x}_1^h$ for $\delta = 0.30$.

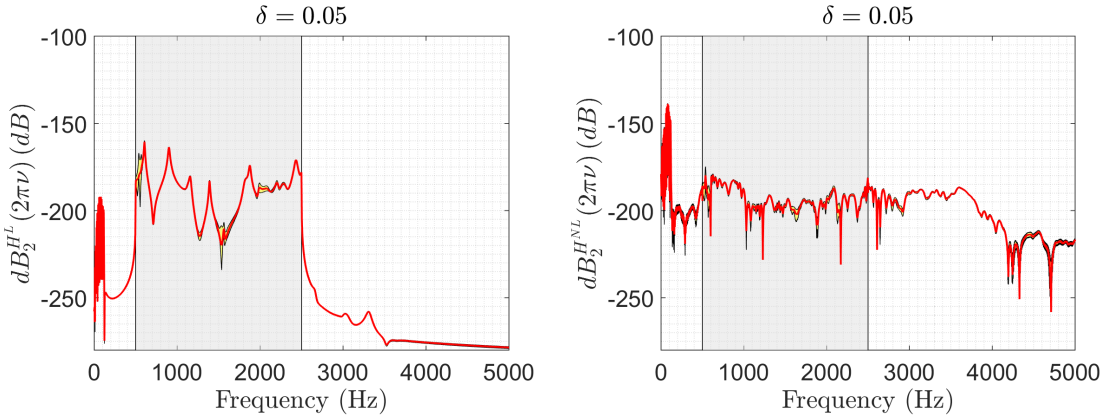

Figure 7.10 – Nominal dynamical responses and confidence regions at 95% of the linear (left figure) and nonlinear (right figure) free-surface elevation at the observation point $\mathbf{x}_1^h$ for $\delta = 0.05$.

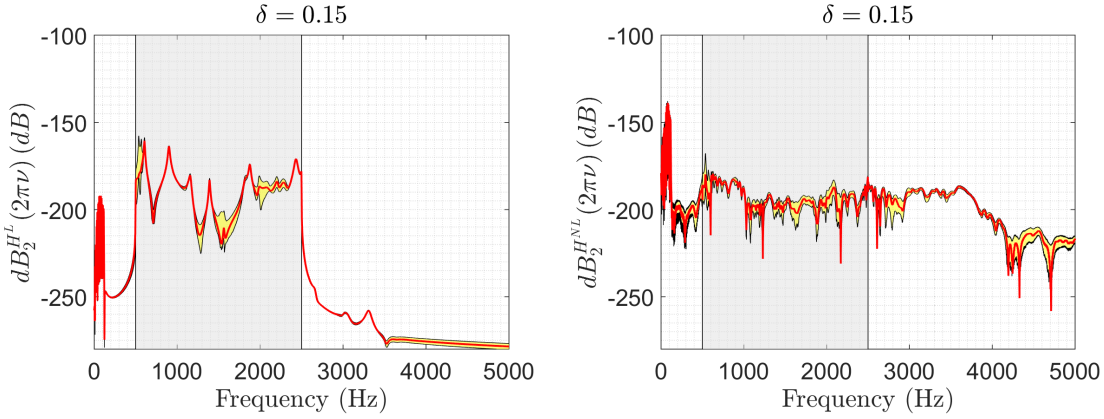

Figure 7.11 – Nominal dynamical responses and confidence regions at 95% of the linear (left figure) and nonlinear (right figure) free-surface elevation at the observation point $\mathbf{x}_1^h$ for $\delta = 0.15$.

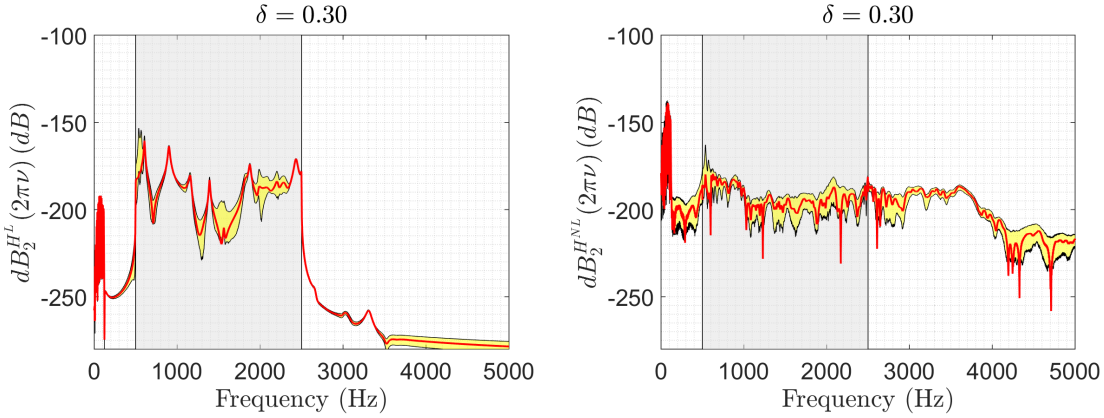

Figure 7.12 – Nominal dynamical responses and confidence regions at 95% of the linear (left figure) and nonlinear (right figure) free-surface elevation at the observation point $\mathbf{x}_1^h$ for $\delta = 0.30$.

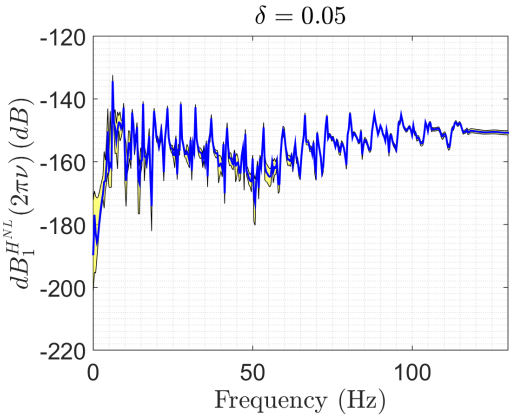

Figure 7.13 – Nominal nonlinear dynamical responses and confidence regions at 95% of the free-surface normal elevation at the observation point $\mathbf{x}_1^h$ for $\delta = 0.05$, displayed over $[0, 130]\,Hz$.

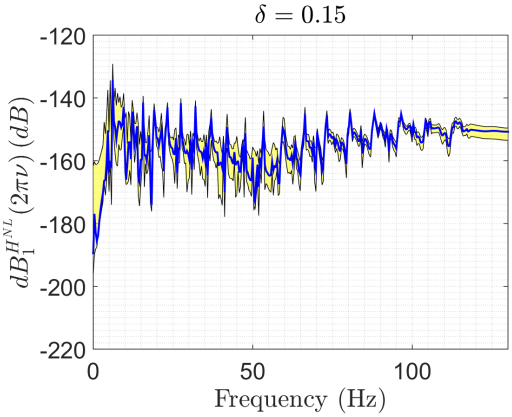

Figure 7.14 – Nominal nonlinear dynamical responses and confidence regions at 95% of the free-surface normal elevation at the observation point $\mathbf{x}_1^h$ for $\delta = 0.15$, displayed over $[0, 130]\,Hz$.

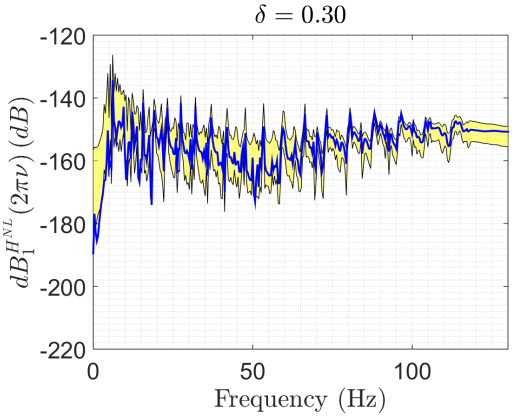

Figure 7.15 – Nominal nonlinear dynamical responses and confidence regions at 95% of the free-surface normal elevation at the observation point $\mathbf{x}_1^h$ for $\delta = 0.30$, displayed over $[0, 130]\,Hz$.

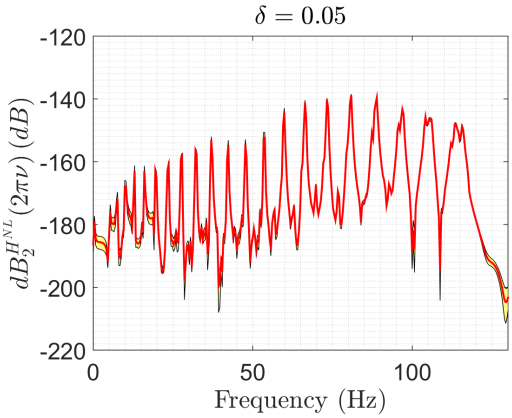

Figure 7.16 – Nominal nonlinear dynamical responses and confidence regions at 95% of the free-surface normal elevation at the observation point $\mathbf{x}_1^h$ for $\delta = 0.05$, displayed over $[0, 130]\,Hz$.

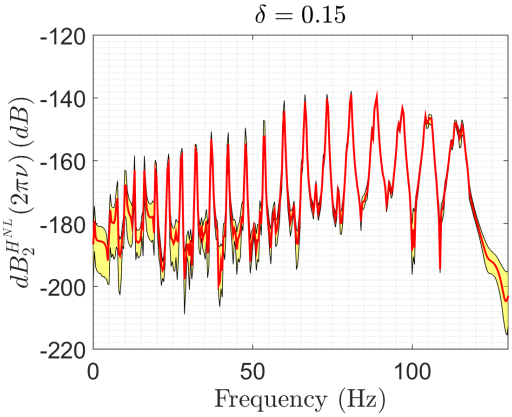

Figure 7.17 – Nominal nonlinear dynamical responses and confidence regions at 95% of the free-surface normal elevation at the observation point $\mathbf{x}_1^h$ for $\delta = 0.15$, displayed over $[0, 130]\,Hz$.

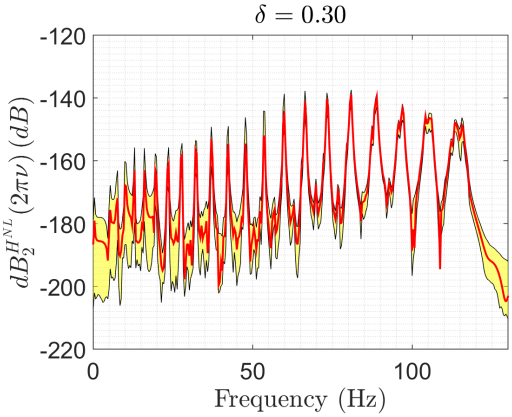

Figure 7.18 – Nominal nonlinear dynamical responses and confidence regions at 95% of the free-surface normal elevation at the observation point $\mathbf{x}_1^h$ for $\delta = 0.30$, displayed over $[0, 130]\,Hz$.

7.4 Statistical inverse problem

This section is devoted to solving the statistical inverse problem for identifying the hyperparameter δ of the probabilistic model of the elastic forces. For the identification, the experimental target has been generated by simulations and will be called simulated data. The statistical inverse problem is formulated as an optimization problem for which the cost function corresponds to a least-square formulation.

7.4.1 Generating the simulated data

The simulated data are constituted of N_r^{exp} independent realizations computed using the stochastic reduced-order computational model introduced in Section 7.2. These simulated frequency response functions are observed on the *experimental* points shown in Figure 7.19. These ob-

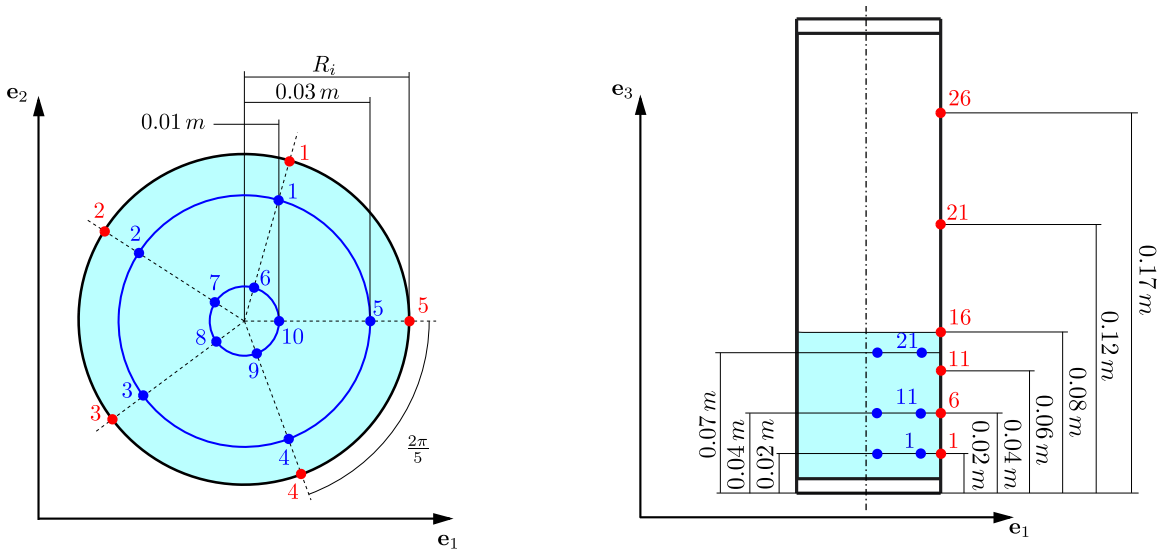

Figure 7.19 – Position of the observation points for the stochastic problem.

servation points have been chosen in order to potentially reproduce experimental apparatus conditions. For this reason, the inverse identification of hyperparameter δ does not take into account the data on the free-surface sloshing. There are $n_p^{\text{obs}} = 30$ observations for the acoustic pressure (blue dots on Figure 7.19) and $n_u^{\text{obs}} = 30$ observations for structural displacement (red dots on Figure 7.19). For the structural displacement of the elastic structure, the corresponding quantities of interest are defined by

$$dB_i^{U,\text{exp}}(2\pi\nu) = 20\log_{10}\left(\left\|\widehat{\mathbb{U}}_{\mathbf{x}_i^u}^{\text{NL,exp}}(2\pi\nu)\right\|_{\mathbb{C}^3}\right) \quad , \tag{7.22}$$

at the 30 observation points $\mathbf{x}_i^u$, $i = 1, \ldots, n_u^{\text{obs}}$, defined in Figure 7.19. The quantities of interest related to the acoustic liquid are defined by

$$dB_i^{P,\text{exp}}(2\pi\nu) = 20\log_{10}(\,|\widehat{\mathbb{P}}_{\mathbf{x}_i^p}^{\text{NL,exp}}(2\pi\nu)|\,) \quad , \tag{7.23}$$

for the 30 observation points $\mathbf{x}_i^p$, $i = 1, \ldots, n_p^{\text{obs}}$, in the internal liquid, displayed in Figure 7.19.

7.4.2 Definition of the cost function

For estimating the optimal value of hyperparameter δ using the simulated data, the cost function is defined in the framework of the least-square method. This method consists in calculating the optimal value δ^{opt} of δ, solving

$$\delta^{\text{opt}} = \arg\min \mathscr{J}(\delta) \quad , \tag{7.24}$$

in which $\mathscr{J}(\delta)$ is written as

$$\mathscr{J}(\delta) = \mathscr{J}_1(\delta) + \mathscr{J}_2(\delta) \quad . \tag{7.25}$$

The cost function $\mathscr{J}_1(\delta)$ is calculated for each subset of the fluid-structure system as

$$\mathscr{J}_1(\delta) = \mathscr{J}_1^U(\delta) + \mathscr{J}_1^P(\delta) \quad . \tag{7.26}$$

In Eq. (7.26), the cost function for each part of the system is calculated, for $x \in \{U, P\}$, by

$$\mathscr{J}_1^X(\delta) = \frac{\displaystyle\int_{\mathbb{B}_a} \sum_{k=1}^{n_{\text{obs}}^X} \Big(E\{\, dB_k^X(2\pi\nu;\delta)\,\} - E\{\, dB_k^{X,\text{exp}}(2\pi\nu)\,\} \Big)^2 \, d\nu}{\displaystyle\int_{\mathbb{B}_a} \sum_{k=1}^{n_{\text{obs}}^X} \Big(E\{\, dB_k^{X,\text{exp}}(2\pi\nu)\,\} \Big)^2 \, d\nu} \tag{7.27}$$

The cost function $\mathscr{J}_2(\delta)$ is calculated for each part of the fluid-structure system as

$$\mathscr{J}_2(\delta) = \mathscr{J}_2^U(\delta) + \mathscr{J}_2^P(\delta) \quad . \tag{7.28}$$

In Eq. (7.28), the cost function for each part of the system is calculated, for $X \in \{U, P\}$, by

$$\mathscr{J}_2^X(\delta) = \frac{\displaystyle\int_{\mathbb{B}_a} \big(\Delta^X(2\pi\nu,\delta) - \Delta^{X,\text{exp}}(2\pi\nu) \big)^2 \, d\omega}{\displaystyle\int_{\mathbb{B}_a} \Delta^{X,\text{exp}}(2\pi\nu) \, d\omega} \quad , \tag{7.29}$$

In Eq. (7.29), the quantity $\Delta^X(2\pi\nu,\delta)$ is written as

$$\Delta^X(2\pi\nu,\delta) = \left(\frac{E\left\{ \displaystyle\sum_{k=1}^{n_{\text{obs}}^X} dB_k^X(2\pi\nu,\delta)^2 \right\} - \displaystyle\sum_{k=1}^{n_{\text{obs}}^X} E\left\{ dB_k^X(2\pi\nu,\delta) \right\}^2}{\displaystyle\sum_{k=1}^{n_{\text{obs}}^X} E\left\{ dB_k^X(2\pi\nu,\delta) \right\}^2} \right)^{\frac{1}{2}} \quad , \tag{7.30}$$

and the quantity $\Delta^{X,\text{exp}}(2\pi\nu)$ is defined by Eq. (7.30) in which dB^X is replaced by $dB^{X,\text{exp}}$.

7.4.3 Identification of the optimal hyperparameter δ^{opt}

The methodology for constructing the cost function $\mathscr{J}(\delta)$ for estimating an optimal hyperparameter δ^{opt} of the stochastic computational model with respect to a reference simulated data set has been presented in the previous sections. A numerical illustration is presented hereinafter in which the optimal parameter δ^{opt} is evaluated using the inverse problem methodology, and is

compared to the dispersion parameter $\delta^{\text{exp}} = 0.3$ used for generating the simulated data as function of N_r^{exp}. Figure 7.20 displays the graphs of 6 cost functions $\mathscr{J}(\delta)$ evaluated for 6 different values $N_r^{\text{exp}} \in \{5, 10, 20, 60, 120, 200\}$. It can be seen in Figure 7.20 that the estimated optimal hyperparameter δ^{opt} converges to $\delta^{\text{exp}} = 0.3$ with respect to N_r^{exp}. The results show that the identification of the optimal hyperparameter δ^{opt} strongly depends on the initial number N_r^{exp} of the simulated data.

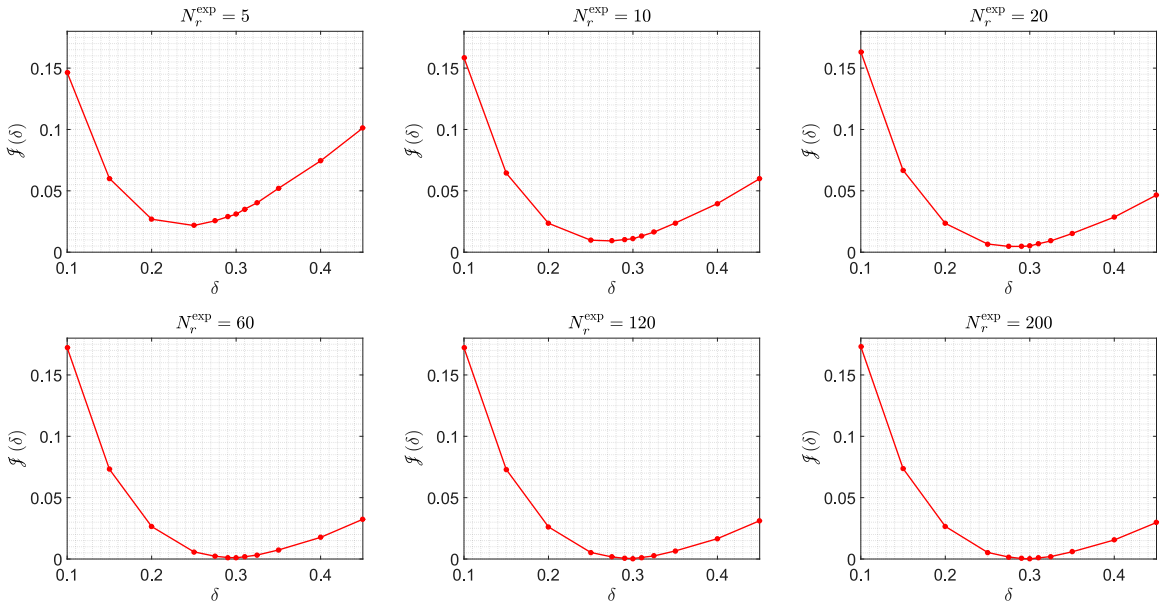

Figure 7.20 – Graphs of $\delta \mapsto \mathscr{J}(\delta)$ displaying the cost function $\mathscr{J}(\delta)$ with respect to the hyperparameter δ for 6 values of $N_r^{\text{exp}} \in \{5, 10, 20, 60, 120, 200\}$.

Conclusion and Perspectives

General conclusion

In this thesis, it has been proposed to analyze the behavior of several geometrically nonlinear coupled fluid-structure systems taking into account the effects of sloshing and capillarity. A nonlinear computational reduced-order model has been constructed allowing for defining the modal characterization of the complex systems, for separating the frequency scales in the model, and for considerably reducing the computational costs induced by the dynamical simulations of such systems. This nonlinear reduced-order model has also allowed for implementing the non-parmetric probabilistic approach for model uncertainties and their quantification such coupled fluid-structure systems.

After presenting the theoretical context of the study as well as the computational model used for the dynamical simulations, several numerical applications have been proposed in order to analyze different aspects related to such highly coupled fluid-structure systems. It was first proposed to analyze the computational cost induced by the simulation of the system dynamical behavior, and particularly induced by the construction of the projection basis of the reduced-order model. This construction requires to solve three generalized eigenvalue problems that happen to be very expensive in the case of large-scale coupled fluid-structure systems. The proposed method for circumventing the non-feasibility of calculations on our mid-power computers is based on two algorithms. The first algorithm is called "double projection" and allows us, by introducing an intermediate reduction of the numerical model, to solve the generalized eigenvalue problem related to the structure with added mass effect (due to the internal liquid), and to solve the generalized eigenvalue problem related to the free-surface sloshing taking into account the effect of the free-surface sloshing motion on the acoustic pressure in the liquid. The second algorithm is a subspace iteration method allowing for solving the generalized eigenvalue problem related to the internal acoustic liquid, which becomes very expensive when the matrices related to the liquid are weakly sparse.

A numerical application is then proposed, in which the quantification of the influence of the coupling operator on the triple line (called triple line operator) between the free surface of the liquid and the elastic structure is investigated (see [87] for the mathematical developments). Indeed, this operator, recently introduced in the theoretical formulation used for the coupled fluid-structure problem, allows for taking into account the coupling effects at the triple line level when considering a deformable structure. The quantification of its influence has been performed by analyzing a fluid-structure coupled system designed to promote the energy transfer induced by the triple line coupling. This system has been studied for different free surface configurations with respect to different contact angles. It has been shown that this triple line operator is of great importance when criteria of high curvature and low contact angle are combined. This operator

modifies the dynamical responses of the fluid-structure system and allows for batter taking into account the dynamical couplings that may occur between the different parts of the system.

The third computational analysis proposed is the analysis and the explanation of a phenomenon of high-amplitude response of the internal liquid free-surface at very-low frequencies in a cylindrical tank submitted to high-frequency excitation. We recall that an experimental campaign conducted in 1962 revealed an *unexpected* phenomenon of high-amplitude vibration of the free surface of the internal liquid during the high-frequency excitation of the cylinder. Indeed, this phenomenon was all the more unexpected as the magnitude difference between the resonance frequencies of the free surface of the liquid and the resonance frequencies of the structure is about 100. The work presented in this thesis has provided an explanation of this *unexpected* experimental phenomenon through a numerical simulation of a coupled fluid-structure system taking into account the geometrical nonlinearities of the structure. The computational results show the same very low-frequency excitation of the free surface induced by an energy transfer, due to the geometrical nonlinearities of the structure, from the tank to the free surface by an *indirect coupling*. This indirect coupling consists in a quasistatic energy transfer between the fluid and its free surface.

Finally, an analysis of the model uncertainties and their propagation has been performed. The nonlinear stochastic reduced-order model has been constructed using the nonparametric probabilistic approach of model uncertainties allowing for considering the modeling errors in the stiffness matrix of the structure. A sensitivity analysis has been carried out by comparing the influence of the uncertainty dispersion hyperparameter of the probabilistic model on the dynamical responses of the system. The results show a significant, if not a great, sensitivity of the displacement of the structure, of the acoustic pressure in the liquid, and of the free-surface elevation to uncertainties in both linear and geometrically nonlinear simulations. Note that the dynamical sloshing responses of the free surface show an increasing uncertainty sensitivity as one moves further from the shell wall. Indeed, the points on the free surface, which are the most distant from the structure, show a higher level of sensitivity to uncertainty than those on the triple line. However, a robustness (with respect to uncertainties) of the very-low frequency sloshing resonances has been noticed. In addition, a methodology for the inverse identification of the hyperparameter of the stochastic model of uncertainties, applied to a coupled fluid-structure system, has been detailed. This methodology has been illustrated by a numerical application for which, due to the absence of experimental data, the target dataset has been computationally simulated.

Perspectives

- Concerning the triple line operator, additional works could be performed, which would consist in analyzing other fluid-structure systems with respect to the influence of the contact angle coupling condition for deformable structures. Several features could be explored such as micro-gravity environments in which high curvature conditions are due to the predominance of capillarity effects.

- In the framework on uncertainty quantification, a first perspective would be to quantify the influence of model uncertainties on the coupling operators in the fluid-structure system. In this work, the proposed model has presented the uncertainty propagation of the model uncertainties involved by the structural stiffness to the whole system. An interesting devel-

opment would thus be to model the coupling operators, such as the triple line operator,using the nonparametric probabilistic approach of model uncertainties. Such nonparametric approach applied to triple operator could be justified by the existence of modeling errors around the triple line, for example, contact angle values or surface roughness properties.

- Another perspective would consist in simultaneously using the nonparametric probabilistic approach of model uncertainties based on the random matrix theory, and the nonparametric probabilistic approach recently proposed [103], based on the use of stochastic ROBs. Due to the block construction of the reduced-order basis, such hybridization would allow for controling the uncertainty level on each subset of the fluid-structure system.

Appendix A

Reduced-order matrices of fluid-structure interactions

In this appendix, the full expressions of the reduced-order matrices of the fluid-structure system, introduced in Section 2.5, are detailed. The fluid-structure redcued-order matrix $[\mathcal{M}_{\text{FSI}}]$, which is defined in Eq. (2.77), can be written by blocks as

$$[\mathcal{M}_{\text{FSI}}] = \begin{bmatrix} [\mathcal{M}_{11}] & [\mathcal{M}_{12}] & [\mathcal{M}_{13}] \\ [\mathcal{M}_{21}] & [\mathcal{M}_{22}] & [\mathcal{M}_{23}] \\ [0] & [0] & [\mathcal{M}_{33}] \end{bmatrix} \quad , \tag{A.1}$$

in which the sub-matrices are written as

$$[\mathcal{M}_{11}] = [\Phi_p]^T [M_p] [\Phi_p] \quad , \tag{A.2}$$

$$[\mathcal{M}_{12}] = [\Phi_p]^T [M_p] [\Phi_{ph}] - [\Phi_p]^T [C_{p\eta}]^T [\Phi_h] \quad , \tag{A.3}$$

$$[\mathcal{M}_{13}] = -[\Phi_p]^T [C_{pu}]^T [\Phi_u] \quad , \tag{A.4}$$

$$[\mathcal{M}_{21}] = [\Phi_{ph}]^T [M_p] [\Phi_p] \quad , \tag{A.5}$$

$$[\mathcal{M}_{22}] = [\Phi_{ph}]^T [M_p] [\Phi_{ph}] - [\Phi_{ph}]^T [C_{p\eta}]^T [\Phi_h] \quad , \tag{A.6}$$

$$[\mathcal{M}_{23}] = -[\Phi_{ph}]^T [C_{pu}]^T [\Phi_u] \quad , \tag{A.7}$$

$$[\mathcal{M}_{33}] = [\Phi_u]^T [M_u] [\Phi_u] \quad . \tag{A.8}$$

The fluid-structure reduced-order matrix $[\mathcal{D}_{\text{FSI}}]$, which is defined in Eq. (2.78), can be written by blocks as

$$[\mathcal{D}_{FSI}] = \begin{bmatrix} [\mathcal{D}_{11}] & [\mathcal{D}_{12}] & [0] \\ [\mathcal{D}_{21}] & [\mathcal{D}_{22}] & [0] \\ [0] & [0] & [\mathcal{D}_{33}] \end{bmatrix} \quad , \tag{A.9}$$

in which the sub-matrices are written as

$$[\mathcal{D}_{11}] = [\Phi_p]^T [D_p] [\Phi_p] \quad , \tag{A.10}$$

$$[\mathcal{D}_{12}] = [\Phi_p]^T [D_p] [\Phi_{ph}] \quad , \tag{A.11}$$

$$[\mathcal{D}_{21}] = [\Phi_{ph}]^T [D_p] [\Phi_p] \quad , \tag{A.12}$$

$$[\mathcal{D}_{22}] = [\Phi_{ph}]^T [D_p] [\Phi_{ph}] \quad , \tag{A.13}$$

$$[\mathcal{D}_{33}] = [\Phi_u]^T [D_u] [\Phi_u] \quad . \tag{A.14}$$

The fluid-structure reduced-order matrix $[\mathcal{K}_{\text{FSI}}]$, which is defined in Eq. (2.79), can be written by blocks as

$$[\mathcal{K}_{FSI}] = \begin{bmatrix} [\mathcal{K}_{11}] & [\mathcal{K}_{12}] & [0] \\ [\mathcal{K}_{21}] & [\mathcal{K}_{22}] & [\mathcal{K}_{23}] \\ [\mathcal{K}_{31}] & [\mathcal{K}_{32}] & [\mathcal{K}_{33}] \end{bmatrix} \quad , \tag{A.15}$$

in which the sub-matrices are written as

$$[\mathcal{K}_{11}] = [\Phi_p]^T [K_p] [\Phi_p] \quad , \tag{A.16}$$

$$[\mathcal{K}_{12}] = [\Phi_p]^T [K_p] [\Phi_{ph}] \quad , \tag{A.17}$$

$$[\mathcal{K}_{21}] = [\Phi_{ph}]^T [K_p] [\Phi_p] + [\Phi_h]^T [C_{ph}] [\Phi_p] \quad , \tag{A.18}$$

$$[\mathcal{K}_{22}] = [\Phi_{ph}]^T [K] [\Phi_{ph}] + [\Phi_h]^T [C_{ph}] [\Phi_{ph}] + [\Phi_h]^T [K_{gc}] [\Phi_h] \quad , \tag{A.19}$$

$$[\mathcal{K}_{23}] = [\Phi_h]^T [C_{hu}] [\Phi_u] \quad , \tag{A.20}$$

$$[\mathcal{K}_{31}] = [\Phi_u]^T [C_{pu}] [\Phi_p] \quad , \tag{A.21}$$

$$[\mathcal{K}_{32}] = [\Phi_u]^T [C_{pu}] [\Phi_{ph}] + [\Phi_u]^T [C_{hu}]^T [\Phi_h] \quad , \tag{A.22}$$

$$[\mathcal{K}_{33}] = [\Phi_u]^T [K_u] [\Phi_u] \quad . \tag{A.23}$$

Appendix B

Construction of the matrices of the computational model by the finite element method

The finite element discretization of the operators of the coupled fluid-structure system introduced in Section 2.4 is based on the Ritz-Galerkin approximation (see Eq. (2.51)). This method requires to choose an appropriate set of vector basis (e_j) for correctly approximating the dynamical behavior of the fluid-structure interaction problem. In the present case, the finite element is chosen, involving isoparametric solid finite elements for the volumes, surface finite elements for the coupling interfaces, and uni-dimensional finite elements for the triple line.

The spatial discretization of the domain is performed by defining a finite element mesh of each subset of the system. This means that the mesh of the complete system is generated and then the interface meshes are doubled to obtain a mesh for each sub-part of the system, for the liquid, for the free surface and for the structure. This ensures that unknowns of the problem are defined in their entire sub-domain and allows for maintaining mesh compatibility at the interfaces. The complete finite element mesh is composed of $N_E = N_{E_p} + N_{E_h} + N_{E_u}$ elements denoted by $(E_i)_{i=1,\dots n_e}$, where N_{E_p} (resp. N_{E_h}, N_{E_u}) denotes the number of elements of the internal fluid (resp. the number of element of the free surface, and the number of elements of the structure). The quantities denoted by superscript E refer to elementary quantities related to the considered element. A classical formulation for the discretization is the isoparametric finite element method which consists in defining the elementary interpolation functions in a given reference element and expressing them in the physical space by defining a bijection between the reference and the physical elements. The introduction of a finite element approximation $(\mathbf{P}, \mathbf{H}, \mathbf{U})$ for unknown fields $(p, h, \mathbf{u})$ leads to the decomposition of the multi-linear forms defined in Section 2.4 into an assembly of elementary quantities on each subdomain. For example, the mass operator of the internal liquid defined in Eq. (2.52) can be approximated as

$$\delta\mathbf{P}^T \left[M_p\right] \mathbf{P} \approx \mathop{\mathbb{A}}_{i=1}^{N_{E_p}} \delta\mathbf{P}_{E_i}^T \left[M_p\right]_{E_i} \mathbf{P}_{E_i} \quad , \tag{B.1}$$

where $\mathbf{P}_{E_i}$ denotes the vector of the elementary discretization of pressure $\mathbf{P}$ and where $[M_p]_{E_i}$ denotes the elementary fluid mass matrix associated with element $E_{i_{(i=1,\dots,n_E)}}$. In Eq. (B.1) the operator $\mathbb{A}$ denotes the finite element assembling operator.

B.1 Finite element discretization of the three-dimensional operators

B.1.1 Isoparametric formulation

Let E be an isoparametric finite element whose nodes coordinates are expressed in the global basis $(\mathbf{e}_1, \mathbf{e}_2, \mathbf{e}_3)$. Let E^r be the corresponding reference element with local basis $(\mathbf{e}_1^r, \mathbf{e}_2^r, \mathbf{e}_3^r)$. The volume domains occupied by finite element domain E and E^r are denoted by Ω_E and Ω_{E^r} respectively. The transformation denoted as T associates one point m of the reference domain with coordinates $\boldsymbol{\xi} = (\xi_1, \xi_2, \xi_3)$, to one point M of the physical domain, with coordinates $\mathbf{x} = (x_1, x_2, x_3)$ (see Figure B.1). This bijection can be expressed as

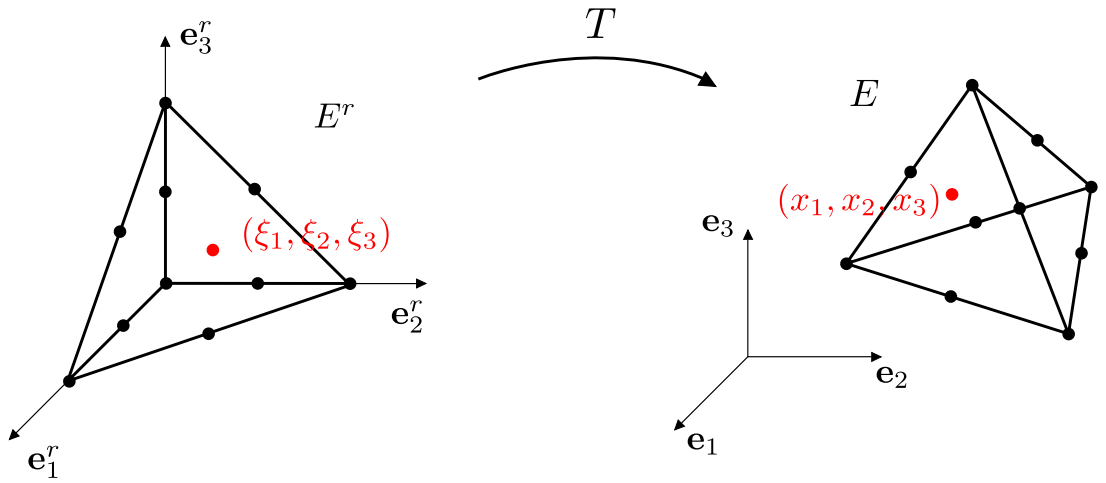

Figure B.1 – Bijective transformation between the isoparametric reference 3D finite element E^r and the 3D physical finite element E.

$$x_1(\boldsymbol{\xi}) = \sum_{i=1}^{n} N_i(\boldsymbol{\xi})\, X_1^{(i)} \quad , \quad x_2(\boldsymbol{\xi}) = \sum_{i=1}^{n} N_i(\boldsymbol{\xi})\, X_2^{(i)} \quad , \quad x_3(\boldsymbol{\xi}) = \sum_{i=1}^{n} N_i(\boldsymbol{\xi})\, X_3^{(i)} \quad , \tag{B.2}$$

in which n is the number of nodes of a given finite element E, $X_1^{(i)}$, $X_2^{(i)}$, and $X_3^{(i)}$ are the coordinates of the i^{th} node of the reference finite element, and $N_i(\boldsymbol{\xi})$ are the shape functions or interpolation functions that depend on the type of interpolation.

Let $[J(\boldsymbol{\xi})]$ be the (3×3) real matrix that represents the Jacobian matrix of the transformation T such that

$$[J(\boldsymbol{\xi})]_{ij} = \frac{\partial x_j}{\partial \xi_i} \, . \tag{B.3}$$

We then introduce the following properties that will be useful in the following. Let $f(\mathbf{x})$ be a given scalar field. We are interested in evaluating some integrals that a defined on the volume domain of a given physical finite element into the volume domain of corresponding reference finite element. The gradient of function $f(\mathbf{x})$ with respect to $\mathbf{x}$ is written as

$$\nabla_{\mathbf{x}} f = [J(\boldsymbol{\xi})]^{-1} \nabla_{\boldsymbol{\xi}} f \quad . \tag{B.4}$$

Since the finite elements are isoparametric, we can also write

$$f(\mathbf{x}) = \sum_{i=1}^{n} N_i(\boldsymbol{\xi})\, F_i \quad , \tag{B.5}$$

in which F_i is the value of function $f(\mathbf{x})$ at the nodes of finite element E.

Integral transformation
The integration over a physical finite element E can be expressed over the reference element E^r such that

$$\int_{\Omega_E} f(\mathbf{x})\, d\mathbf{x} = \int_{\Omega_{E^r}} f(\boldsymbol{\xi})\, \det([J(\boldsymbol{\xi})])\, d\boldsymbol{\xi} \,, \tag{B.6}$$

$$\int_{\Omega_E} \nabla_{\mathbf{x}} f(\mathbf{x})\, d\mathbf{x} = \int_{\Omega_{E^r}} [J(\boldsymbol{\xi})]^{-1}\, \nabla_{\boldsymbol{\xi}} f(\boldsymbol{\xi})\, \det([J(\boldsymbol{\xi})])\, d\boldsymbol{\xi} \quad , \tag{B.7}$$

in which $\nabla_{\boldsymbol{\xi}} f(\boldsymbol{\xi})$ is easily evaluated.

B.1.2 Interpolation of the unknown fields

The pressure $p(\mathbf{x})$ and the free-surface elevation $h(\mathbf{x})$ can be interpolated on a given element E such that

$$p(\mathbf{x}) = [N(\boldsymbol{\xi})]\, \mathbf{P}_E \quad , \quad h(\mathbf{x}) = [N(\boldsymbol{\xi})]\, \mathbf{H}_E \quad , \tag{B.8}$$

where $\mathbf{P}_E$ and $\mathbf{H}_E$ are the $\mathbb{R}^n$-vectors of the nodal values of pressure and free-surface elevation of finite element E, and where $[N(\boldsymbol{\xi})]$ is the $(1 \times n)$ interpolation matrix such that

$$[N(\boldsymbol{\xi})] = [N_1(\boldsymbol{\xi}) \quad N_2(\boldsymbol{\xi}) \quad \dots \quad N_n(\boldsymbol{\xi})] \quad , \tag{B.9}$$

The elementary vector field $\mathbf{u}^E(\mathbf{x}) = (u_1^E(\mathbf{x}), u_2^E(\mathbf{x}), u_3^E(\mathbf{x}))^T$ can be written as

$$\mathbf{u}^E(\mathbf{x}) = [\mathcal{N}(\boldsymbol{\xi})]\, \mathbf{U}_E \quad , \tag{B.10}$$

in which the $(3 \times 3n)$ interpolation matrix $[\mathcal{N}(\boldsymbol{\xi})]$ is defined by

$$[\mathcal{N}(\boldsymbol{\xi})] = \begin{bmatrix} N_1(\boldsymbol{\xi}) & 0 & 0 & \dots & N_n(\boldsymbol{\xi}) & 0 & 0 \\ 0 & N_1(\boldsymbol{\xi}) & 0 & \dots & 0 & N_n(\boldsymbol{\xi}) & 0 \\ 0 & 0 & N_1(\boldsymbol{\xi}) & \dots & 0 & 0 & N_n(\boldsymbol{\xi}) \end{bmatrix} \quad , \tag{B.11}$$

and where the $\mathbb{R}^{3n}$ vector $\mathbf{U}_E$ is written as

$$\mathbf{U}_E^T = (U_1^{(1)}, U_2^{(1)}, U_3^{(1)}, \dots, U_1^{(n)}, U_2^{(n)}, U_3^{(n)}) \quad , \tag{B.12}$$

where $U_j^{(k)}$ denotes the component number j of the displacement at node number k of the finite element.

Similarly to Eq. (B.5), the gradient of the unknown pressure p in the finite element E is written as

$$\nabla_{\mathbf{x}} p(\mathbf{x}) = \left[\frac{\partial p}{\partial x_1} \quad \frac{\partial p}{\partial x_2} \quad \frac{\partial p}{\partial x_3} \right]^T = [B(\boldsymbol{\xi})]\, \mathbf{P}_E \quad , \tag{B.13}$$

in which $[B(\boldsymbol{\xi})]$ is a $(3 \times n)$ matrix such that

$$[B(\boldsymbol{\xi})] = [J(\boldsymbol{\xi})]^{-1} \begin{bmatrix} \dfrac{\partial N_1(\boldsymbol{\xi})}{\partial \xi_1} & \dfrac{\partial N_2(\boldsymbol{\xi})}{\partial \xi_1} & \cdots & \dfrac{\partial N_n(\boldsymbol{\xi})}{\partial \xi_1} \\ \dfrac{\partial N_1(\boldsymbol{\xi})}{\partial \xi_2} & \dfrac{\partial N_2(\boldsymbol{\xi})}{\partial \xi_2} & \cdots & \frac{\partial N_n(\boldsymbol{\xi})}{\partial \xi_2} \\ \dfrac{\partial N_1(\boldsymbol{\xi})}{\partial \xi_3} & \dfrac{\partial N_2(\boldsymbol{\xi})}{\partial \xi_3} & \cdots & \dfrac{\partial N_n(\boldsymbol{\xi})}{\partial \xi_3} \end{bmatrix} \quad . \tag{B.14}$$

In the following, the Voigt notation is introduced. The second Piola-Kirchhoff tress tensor and the Green-Lagrange strain tensor are represented by

$$\{S\} = (S_{11}, S_{22}, S_{33}, 2S_{23}, 2S_{13}, 2S_{12}) \quad , \quad \{E\} = (E_{11}, E_{22}, E_{33}, E_{23}, E_{13}, E_{12}) \tag{B.15}$$

The constitutive equations defined by Eq. (2.14) can then be written as

$$\{S\} = [C]\,\{E\} \quad , \tag{B.16}$$

in which $[C]$ is the (6×6) matrix defined by

$$[C] = \begin{bmatrix} \lambda + 2\mu & \lambda & \lambda & 0 & 0 & 0 \\ \lambda & \lambda + 2\mu & \lambda & 0 & 0 & 0 \\ \lambda & \lambda & \lambda + 2\mu & 0 & 0 & 0 \\ 0 & 0 & 0 & \mu & 0 & 0 \\ 0 & 0 & 0 & 0 & \mu & 0 \\ 0 & 0 & 0 & 0 & 0 & \mu \end{bmatrix} \quad , \tag{B.17}$$

in which λ and μ are the Lamé coefficients. In particular, the linearized strain tensor is written as

$$\{\varepsilon\} = [\mathcal{B}(\boldsymbol{\xi})]\,\mathbf{U}_E \quad , \tag{B.18}$$

in which $[\mathcal{B}(\boldsymbol{\xi})]$ is the $(6 \times 3n)$ interpolation matrix whose entries contains the partial derivatives of the interpolation functions following the voigt notation.

B.1.3 Finite element discretization of the 3D operators

The computational evaluation of integrals over the reference elementary volume Ω_E^r is performed by using a Gauss quadrature [113, 44, 25, 111]. Generally, we have

$$\int_{\Omega_E^r} f(\boldsymbol{\xi})\, d\boldsymbol{\xi} \approx \sum_{g=1}^{n_g} f(\boldsymbol{\xi}_g)\, \omega_g \;, \tag{B.19}$$

in which n_g denotes the number of Gauss integration points, $\boldsymbol{\xi}_g$ denotes the coordinates of the integration points in the reference finite element, and ω_g denotes the corresponding weight of each Gauss point. Below, the expression of the elementary finite element matrices corresponding to 3D finite elements are given.

The elementary "fluid" and "structural" mass matrices are written as

$$[M_p]_E = \frac{1}{\rho_0 c_0^2} \sum_{g=1}^{n_g} [N(\boldsymbol{\xi}_g)]^T\, [N(\boldsymbol{\xi}_g)]\, \det\left([J(\boldsymbol{\xi}_g)]\right)\, \omega_g \quad , \tag{B.20}$$

$$[M_u]_E = \rho_S \sum_{g=1}^{n_g} [\mathcal{N}(\boldsymbol{\xi}_g)]^T \, [\mathcal{N}(\boldsymbol{\xi}_g)] \, \det\left([J(\boldsymbol{\xi}_g)]\right) \, \omega_g \quad , \tag{B.21}$$

The elementary "fluid" and "structural" stiffness matrices are written as

$$[K_p]_E = \frac{1}{\rho_0} \sum_{g=1}^{n_g} [B(\boldsymbol{\xi}_g)]^T \, [B(\boldsymbol{\xi}_g)] \, \det\left([J(\boldsymbol{\xi}_g)]\right) \, \omega_g \quad , \tag{B.22}$$

$$[K_u]_E = \sum_{g=1}^{n_g} \left[\mathcal{B}(\boldsymbol{\xi}_g)\right]^T \, [C] \, \left[\mathcal{B}(\boldsymbol{\xi}_g)\right] \, \det\left([J(\boldsymbol{\xi}_g)]\right) \, \omega_g \quad . \tag{B.23}$$

The assembling of the elementary matrices is then carried out taking into account the prescribed boundary conditions.

B.2 Finite element discretization of two-dimensional operators

B.2.1 Isoparametric formulation

The finite element meshes are ssumed to be compatible and interfaces are constituted of some faces of the 3D finite elements. This 2D restriction defines a two-dimensional physical isoparametric finite element $\bar{E}$ for which the normal n^p is characterized in the global coordinate system $(\mathbf{e}_1, \mathbf{e}_2, \mathbf{e}_3)$. A local coordinate system $(\bar{\mathbf{e}}_1, \bar{\mathbf{e}}_2)$ is then introduced for finite element $\bar{E}$. Let then $\bar{E}^r$ be the corresponding reference element with local basis $(\bar{\mathbf{e}}_1, \bar{\mathbf{e}}_2)$. The bijective transformation $\bar{T}$ between $\bar{E}$ and $\bar{E}^r$ associates the coordinates $(\bar{x}_1, \bar{x}_2)$ of a point located in the physical finite element $\bar{E}$ with its corresponding counterpart of coordinates $(\bar{\xi}_1, \bar{\xi}_2)$ in the reference finite element such that

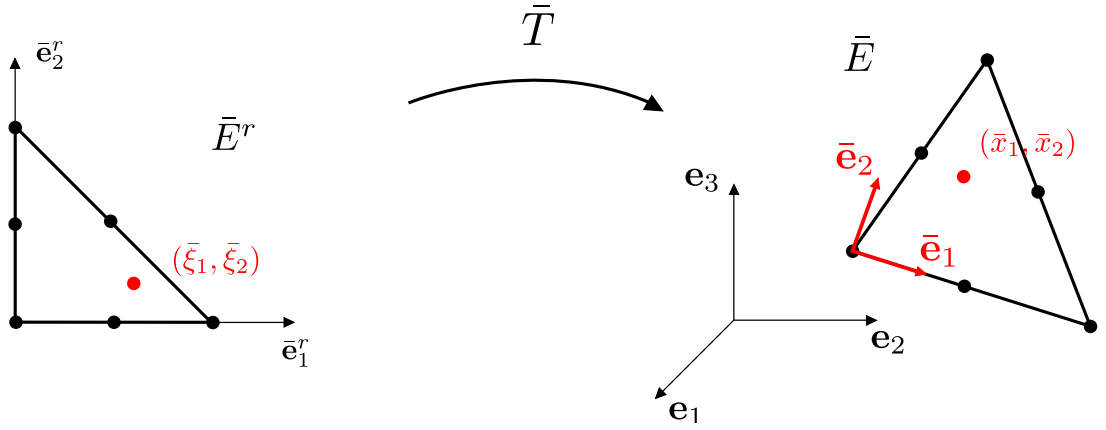

Figure B.2 – Bijective transformation between the isoparametric reference 2D finite element $\bar{E}^r$ and the local coordinate system $(\bar{\mathbf{e}}_1, \bar{\mathbf{e}}_2)$ of the 2D physical finite element $\bar{E}$.

$$\bar{x}_1(\bar{\boldsymbol{\xi}}) = \sum_{i=1}^{\bar{n}} \bar{N}_i(\bar{\boldsymbol{\xi}}) \, \bar{X}_1^{(i)} \quad , \quad \bar{x}_2(\bar{\boldsymbol{\xi}}) = \sum_{i=1}^{\bar{n}} \bar{N}_i(\bar{\boldsymbol{\xi}}) \, \bar{X}_2^{(i)} \quad , \tag{B.24}$$

in which $\bar{n}$ is the number of nodes of a given 2D finite element, $\bar{X}_1^{(i)}$ and $\bar{X}_2^{(i)}$ are the coordinates of the i^{th} node of this given 2D element in its local system of coordinates, and $\bar{N}_i(\bar{\boldsymbol{\xi}})$ are the 2D

shape function. Let $[\bar{J}(\bar{\boldsymbol{\xi}})]$ be the (2×2) real matrix that represents the Jacobian matrix of the transformation such that

$$[\bar{J}(\bar{\boldsymbol{\xi}}]_{ij} = \frac{\partial \bar{x}_i}{\partial \bar{\xi}_j} \, . \tag{B.25}$$

B.2.2 Interpolation of the unknown fields

The pressure $p(\mathbf{x})$ and the free-surface elevation $h(\mathbf{x})$ can be interpolated on a given 2D finite element $\bar{E}$ such that

$$p(\mathbf{x}) = [\bar{N}(\bar{\boldsymbol{\xi}})] \, \mathbf{P}_{\bar{E}} \quad , \quad h(\mathbf{x}) = [\bar{N}(\bar{\boldsymbol{\xi}})] \, \mathbf{H}_{\bar{E}} \quad , \tag{B.26}$$

in which $\mathbf{P}_{\bar{E}}$ and $\mathbf{H}_{\bar{E}}$ are the $\mathbb{R}^{\bar{n}}$-vectors of the nodal values of pressure and free-surface elevation on 2D finite element $\bar{E}$, and where $[\bar{N}(\bar{\boldsymbol{\xi}})]$ is the $(1 \times \bar{n})$ interpolation matrix such that

$$[\bar{N}(\bar{\boldsymbol{\xi}})] = [\bar{N}_1(\bar{\boldsymbol{\xi}}) \quad \bar{N}_2(\bar{\boldsymbol{\xi}}) \quad \dots \quad \bar{N}_n(\bar{\boldsymbol{\xi}})] \quad . \tag{B.27}$$

The vector field $\mathbf{u}(\mathbf{x})$ can be expressed on the local 2D finite element as

$$\mathbf{u}(\mathbf{x}) = [\bar{\mathcal{N}}(\bar{\boldsymbol{\xi}})] \, \mathbf{U}_{\bar{E}} \quad , \tag{B.28}$$

in which the $(3 \times 3\bar{n})$ interpolation matrix $[\bar{\mathcal{N}}(\bar{\boldsymbol{\xi}})]$ is defined by

$$[\bar{\mathcal{N}}(\bar{\boldsymbol{\xi}})] = \begin{bmatrix} \bar{N}_1(\bar{\boldsymbol{\xi}}) & 0 & 0 & \dots & \bar{N}_{\bar{n}}(\bar{\boldsymbol{\xi}}) & 0 & 0 \\ 0 & \bar{N}_1(\bar{\boldsymbol{\xi}}) & 0 & \dots & 0 & \bar{N}_{\bar{n}}(\bar{\boldsymbol{\xi}}) & 0 \\ 0 & 0 & \bar{N}_1(\bar{\boldsymbol{\xi}}) & \dots & 0 & 0 & \bar{N}_{\bar{n}}(\bar{\boldsymbol{\xi}}) \end{bmatrix} \quad , \tag{B.29}$$

and where the $\mathbb{R}^{3\bar{n}}$ vector $\mathbf{U}_{\bar{E}}$ is written as

$$\mathbf{U}_{\bar{E}}^T = (U_1^{(1)}, U_2^{(1)}, U_3^{(1)}, \dots, U_1^{(\bar{n})}, U_2^{(\bar{n})}, U_3^{(\bar{n})}) \quad . \tag{B.30}$$

The surface gradient that appears in the operator $\mathscr{K}_c^s(h, \delta h)$ can be expressed as a classical gradient in the local surface coordinates system of a given 2D finite element. This gradient is discretized as

$$\nabla_\Gamma \, h_{\bar{E}}(\bar{\mathbf{x}}) = \begin{bmatrix} \dfrac{\partial h_{\bar{E}}(\bar{\mathbf{x}})}{\partial \bar{x}_1} & \dfrac{\partial h_{\bar{E}}(\bar{\mathbf{x}})}{\partial \bar{x}_2} \end{bmatrix}^T = [\bar{B}(\bar{\boldsymbol{\xi}})] \, \mathbf{H}_{\bar{E}} \quad , \tag{B.31}$$

in which $[\bar{B}(\bar{\boldsymbol{\xi}})]$ is the $(2 \times \bar{n})$ interpolation matrix such that

$$[\bar{B}(\bar{\boldsymbol{\xi}})] = [\bar{J}(\bar{\boldsymbol{\xi}})]^{-1} \begin{bmatrix} \dfrac{\partial \bar{N}_1(\bar{\boldsymbol{\xi}})}{\partial \xi_1} & \dfrac{\partial \bar{N}_2(\bar{\boldsymbol{\xi}})}{\partial \xi_1} & \dots & \dfrac{\partial \bar{N}_n(\bar{\boldsymbol{\xi}})}{\partial \xi_1} \\ \dfrac{\partial \bar{N}_1(\bar{\boldsymbol{\xi}})}{\partial \xi_2} & \dfrac{\partial \bar{N}_2(\bar{\boldsymbol{\xi}})}{\partial \xi_2} & \dots & \dfrac{\partial \bar{N}_n(\bar{\boldsymbol{\xi}})}{\partial \xi_2} \end{bmatrix} \quad . \tag{B.32}$$

B.2.3 Finite element discretization of the 2D operators

Similarly to Section B.1.3, the evaluation of the integrals on a given 2D element are approximated using the Gauss quadrature method. In the case of 2D integrals, the number of gauss integration points in denoted $\bar{n}_g$, their coordinates $\bar{\boldsymbol{\xi}}_g$, and the associated Gauss weight $\bar{\omega}_g$. Below, the expression of the elementary finite element matrices corresponding to 2D finite elements are given. The free surface gravity stiffness matrix, the free surface capillarity stiffness matrix, the fluid-structure coupling matrix, and the fluid-free-surface coupling matrix are given by

$$[K_g]_E = \rho_0 \sum_{g=1}^{\bar{n}_g} [\bar{N}(\bar{\boldsymbol{\xi}}_g)]^T \, (\mathbf{n}_{\bar{E}_i}^p \cdot \mathbf{g}_{\bar{E}_i}) \, [\bar{N}(\bar{\boldsymbol{\xi}}_g)] \, \det\left([\bar{J}(\bar{\boldsymbol{\xi}}_g)]\right) \, \bar{\omega}_g \quad , \tag{B.33}$$

$$[K_c^s]_E = -\sum_{g=1}^{\bar{n}_g} \sigma_\Gamma \left(\frac{1}{\left(R_1^{E_i}\right)^2} + \frac{1}{\left(R_2^{E_i}\right)^2} \right) [\bar{N}(\bar{\boldsymbol{\xi}}_g)]^T [\bar{N}(\bar{\boldsymbol{\xi}}_g)] \det\left([\bar{J}(\bar{\boldsymbol{\xi}}_g)]\right) \bar{\omega}_g \ldots + \sum_{g=1}^{\bar{n}_g} \sigma_\Gamma [\bar{B}(\bar{\boldsymbol{\xi}}_g)]^T [\bar{B}(\bar{\boldsymbol{\xi}}_g)] \det\left([\bar{J}(\bar{\boldsymbol{\xi}}_g)]\right) \bar{\omega}_g \quad , \tag{B.34}$$

$$[C_{ph}]_E = -\sum_{g=1}^{\bar{n}_g} [\bar{N}(\bar{\boldsymbol{\xi}}_g)]^T [\bar{N}(\bar{\boldsymbol{\xi}}_g)] \det\left([\bar{J}(\bar{\boldsymbol{\xi}}_g)]\right) \bar{\omega}_g \quad , \tag{B.35}$$

$$[C_{pu}]_E = -\sum_{g=1}^{\bar{n}_g} \left([\bar{\mathcal{N}}(\bar{\boldsymbol{\xi}}_g)]^T \mathbf{n}^p_{\bar{E}_i}\right) [\bar{N}(\bar{\boldsymbol{\xi}}_g)] \det\left([\bar{J}(\bar{\boldsymbol{\xi}}_g)]\right) \bar{\omega}_g \quad , \tag{B.36}$$

It should be noted that, the quantities $\mathbf{n}^p_{\bar{E}_i}$, $\mathbf{g}_{\bar{E}_i}$, $R_1^{E_i}$, and $R_2^{E_i}$ that represents the external unit normal to the fluid, the gravitational intensity vector, and the two principal curvature radii are calculated, *a priori*, for each finite element of the free-surface mesh by a pre-computation described in Appendix C.

B.3 Finite element discretization of one-dimensional operators

B.3.1 Isoparametric formulation

The triple line defines a uni-dimensional domain whose mesh is constituted of uni-dimensional finite elements $\bar{\bar{E}}$ and results from the intersection of two surface meshes that are compatible. The unitary tangent $\bar{\bar{e}}$ is expressed in the global coordinate system $(\mathbf{e}_1, \mathbf{e}_2, \mathbf{e}_3)$ but also defines a local coordinate system. Let $\bar{\bar{E}}^r$ be the corresponding reference finite element with local basis $\bar{\bar{e}}^r$. The bijective transformation $\bar{\bar{T}}$ between $\bar{\bar{E}}$ and $\bar{\bar{E}}^r$ associates the coordinates $(\bar{\bar{x}})$ of a point located in the physical finite element $\bar{\bar{E}}$ with its corresponding counterpart of coordinates $(\bar{\bar{\xi}})$ in the reference finite element $\bar{\bar{E}}^r$ such that

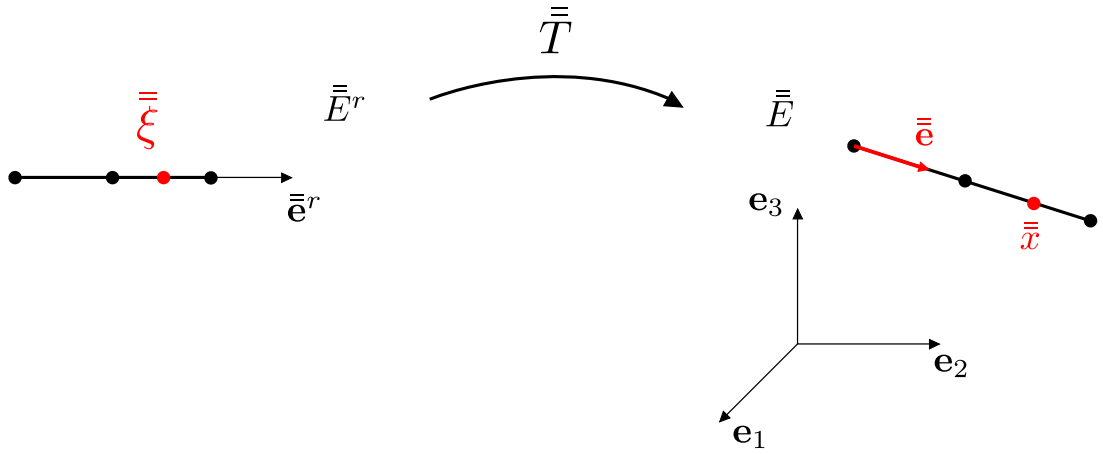

Figure B.3 – Bijective transformation between the isoparametric reference 1D finite element $\bar{\bar{E}}^r$ and the local coordinate system $(\bar{\bar{\mathbf{e}}})$ of the 1D physical finite element $\bar{\bar{E}}$.

$$\bar{\bar{x}}(\bar{\bar{\xi}}) = \sum_{i=1}^{\bar{\bar{n}}} \bar{\bar{N}}_i(\bar{\bar{\xi}})\, \bar{\bar{X}}^{(i)} \, . \tag{B.37}$$

In which $\bar{\bar{n}}$ is the number of nodes of a given 1D finite element, $\bar{\bar{X}}^{(i)}$ is the coordinates of the i^{th} node of this given 1D finite element in its local system of coordinates, and $\bar{\bar{N}}_i(\bar{\bar{\xi}})$ are the 1D shape functions. The Jacobian of the transformation $\bar{\bar{T}}$ is expressed as:

$$\bar{\bar{J}}(\bar{\bar{\xi}}) = \frac{\partial \bar{\bar{x}}}{\partial \bar{\bar{\xi}}} \,. \tag{B.38}$$

B.3.2 Interpolation of the unknown fields

The free-surface elevation $h(\mathbf{X})$ can be interpolated on a given local 1D finite element $\bar{\bar{E}}$ as

$$h(\mathbf{X}) = [\bar{\bar{N}}(\bar{\bar{\xi}})]\, \mathbf{H}_{\bar{\bar{E}}} \quad , \tag{B.39}$$

where $\mathbf{H}_{\bar{\bar{E}}}$ is the $\mathbb{R}^{\bar{\bar{n}}}$-vector of the nodal values of the free-surface elevation of the 1D finite element $\bar{\bar{E}}$ and where $[\bar{\bar{N}}(\bar{\bar{\xi}})]$ is the $(1 \times \bar{\bar{n}})$ interpolation matrix defined such that

$$[\bar{\bar{N}}(\bar{\bar{\xi}})] = [\bar{\bar{N}}_1(\bar{\bar{\xi}}) \quad \bar{\bar{N}}_2(\bar{\bar{\xi}}) \quad \dots \quad \bar{\bar{N}}_{\bar{\bar{n}}}(\bar{\bar{\xi}})] \,. \tag{B.40}$$

The vector field $\mathbf{u}(\mathbf{X})$ can be interpolated on the local 1D element as

$$\mathbf{u}^{\bar{\bar{E}}}(\mathbf{X}) = [\bar{\bar{\mathcal{N}}}(\bar{\bar{\xi}})]\, \mathbf{U}_{\bar{\bar{E}}} \quad , \tag{B.41}$$

in which the $(3 \times 3\bar{\bar{n}})$ interpolation matrix $[\bar{\bar{\mathcal{N}}}(\bar{\bar{\xi}})]$ is defined by

$$[\bar{\bar{\mathcal{N}}}(\bar{\bar{\xi}})] = \begin{bmatrix} \bar{\bar{N}}_1(\bar{\bar{\xi}}) & 0 & 0 & \dots & \bar{\bar{N}}_{\bar{\bar{n}}}(\bar{\bar{\xi}}) & 0 & 0 \\ 0 & \bar{\bar{N}}_1(\bar{\bar{\xi}}) & 0 & \dots & 0 & \bar{\bar{N}}_{\bar{\bar{n}}}(\bar{\bar{\xi}}) & 0 \\ 0 & 0 & \bar{\bar{N}}_1(\bar{\bar{\xi}}) & \dots & 0 & 0 & \bar{\bar{N}}_{\bar{\bar{n}}}(\bar{\bar{\xi}}) \end{bmatrix} \tag{B.42}$$

and where the $\mathbb{R}^{3\bar{\bar{n}}}$-vector $\mathbf{U}_{\bar{\bar{E}}}$ is written as

$$\mathbf{U}_{\bar{\bar{E}}}^T = (U_1^{(1)}, U_2^{(1)}, U_3^{(1)}, \dots, U_1^{(\bar{\bar{n}})}, U_2^{(\bar{\bar{n}})}, U_3^{(\bar{\bar{n}})}) \quad . \tag{B.43}$$

B.3.3 Finite element discretization of the 1D operators

Similarly to Section B.1.3, the evaluation of the integrals on a given 1D element are approximated using the Gauss quadrature method. In the case of 1D integrals, the number of gauss integration points in denoted $\bar{\bar{n}}_g$, their coordinates $\bar{\bar{\xi}}_g$, and the associated Gauss weight $\bar{\bar{\omega}}_g$. The lineic contribution of the free-surface stiffness elementary matrix is given by

$$[K_c^l]_E = -\sum_{g=1}^{\bar{\bar{n}}_g} \sigma_\Gamma \, c_h \, [\bar{\bar{N}}(\bar{\bar{\xi}}_g)]^T \, [\bar{\bar{N}}(\bar{\bar{\xi}}_g)] \det \left([\bar{\bar{J}}(\bar{\bar{\xi}}_g)] \right) \, \bar{\bar{\omega}}_g \quad . \tag{B.44}$$

A particular difficulty with the computation of the coupling matrix between the structure and the free-surface is encountered because it requires the evaluation of the gradient of the displacement field $\mathbf{u}(\mathbf{x})$ on the triple line γ. Such computation cannot be performed with classical interpolation with isoparametric finite element method. Let us introduce the following decomposition of operator $\mathscr{C}_{hu}(\mathbf{u}, \delta h)$

$$\mathscr{C}_{hu}(\mathbf{u}, \delta h) = \mathscr{C}_{hu}^{(1)}(\mathbf{u}, \delta h) + \mathscr{C}_{hu}^{(2)}(\mathbf{u}, \delta h) \quad , \tag{B.45}$$

in which

$$\mathscr{C}_{hu}^{(1)}(\mathbf{u}, \delta h) = -\sigma_\Gamma \int_\gamma d_h \, \mathbf{u} \cdot \mathbf{n}^u \, \delta h \, d\gamma \tag{B.46}$$

and

$$\mathscr{C}_{hu}^{(2)}(\mathbf{u},\delta h) = \sigma_\Gamma \int_\gamma \frac{\partial(\mathbf{u}\cdot\mathbf{n}^u)}{\partial\nu^\Sigma}\,\delta h\,d\gamma \quad . \tag{B.47}$$

The first term $\mathscr{C}_{hu}^{(1)}(\mathbf{u},\delta h)$ can be easily discretized and the corresponding elementary finite element matrix $[C_{hu}^{(1)}]_E$ is given by

$$[C_{hu}^{(1)}]_E = -\sum_{g=1}^{\bar{\bar{n}}_g} \sigma_\Gamma\, d_h\, [\bar{\bar{N}}\bar{\bar{\xi}}_g]^T\, (\mathbf{n}^u_{E_i})^T\, [\bar{\bar{\mathcal{N}}}(\bar{\bar{\xi}})]\, \det\left([\bar{\bar{J}}(\bar{\bar{\xi}}_g)]\right)\, \bar{\bar{\omega}}_g \quad . \tag{B.48}$$

The gradient of the displacement field $\mathbf{u}(\mathbf{x})$ on the triple line γ is evaluated by considering the gradient of the displacement field located in a 3D finite element whose edges contains the 1D finite element under consideration denoted γ_E. In this 3D finite element, the displacement $\mathbf{u}(\mathbf{X})$

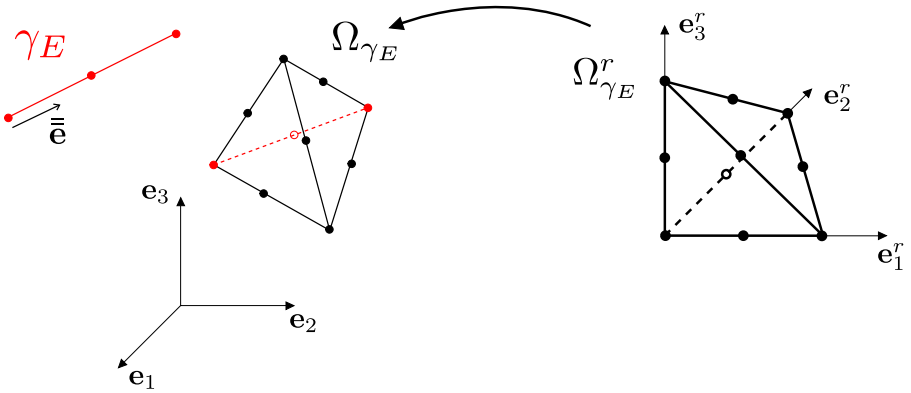

Figure B.4 – Bijective transformation between the isoparametric reference 3D finite element E^r and the 3D physical finite element Ω_{γ_E} adjacent to the 1D local finite element γ_E.

is discretized such that

$$\mathbf{u}(\mathbf{X}) = [\mathcal{N}(\boldsymbol{\xi})]\Big|_{\gamma_E}\, \mathbf{U}_E\Big|_{\gamma_E} \quad . \tag{B.49}$$

where $\mathbf{U}_E|\,\gamma_E = \mathbf{U}_{\bar{\bar{E}}}$ in this case is the nodal value of the displacement along the three dofs for the 3D element, and where $[\mathcal{N}(\boldsymbol{\xi})]$ is the $(3\times 3n)$ interpolation matrix. With this formulation, the elementary displacement gradient $\nabla_{\mathbf{x}}(\mathbf{u}(\mathbf{x})\cdot\mathbf{n}^u_{\bar{\bar{E}}})$ can now be expressed as

$$\nabla\left(\mathbf{u}(\mathbf{x})\cdot\mathbf{n}^u_{\bar{\bar{E}}}\right) = \left([J(\boldsymbol{\xi})]^{-T} \begin{Bmatrix} (\mathbf{n}^u_E)^T \dfrac{\partial[\mathcal{N}(\boldsymbol{\xi})]}{\partial\xi_1} \\ (\mathbf{n}^u_E)^T \dfrac{\partial[\mathcal{N}(\boldsymbol{\xi})]}{\partial\xi_2} \\ (\mathbf{n}^u_E)^T \dfrac{\partial[\mathcal{N}(\boldsymbol{\xi})]}{\partial\xi_3} \end{Bmatrix} \mathbf{U}_E \right)\Bigg|_{\gamma_E} = \left([J(\boldsymbol{\xi})]^{-T}\, [\widetilde{\mathcal{N}}(\boldsymbol{\xi})]\, \mathbf{U}_E \right)\Big|_{\gamma_E} \tag{B.50}$$

The second term $\mathscr{C}_{hu}^{(2)}$ is then discretized and the corresponding elementary finite element matrix $[C_{hu}^{(2)}]_E$ is expressed as

$$[C_{hu}^{(2)}]_E = \sum_{g=1}^{n_g} \sigma_\Gamma\, [\bar{\bar{N}}(\bar{\bar{\xi}}_g)]^T\, (\boldsymbol{\nu}^\Sigma_{E^r})^T \left([J(\boldsymbol{\xi}_g)]^{-T}\, [\widetilde{\mathcal{N}}(\boldsymbol{\xi}_g)] \right)\Big|_{\gamma_{E^r}} \det([\bar{\bar{J}}(\bar{\bar{\xi}}_g])\,\omega_g \quad , \tag{B.51}$$

in which the tangential vector $\boldsymbol{\nu}_{E^r}^{\Sigma}$ is *a priori* computed in the global coordinate system. It should be noted that, in order to ensure the correct intergration using the Gauss point method, it is essential to determine the corresponding coordinates $\boldsymbol{\xi}_g$ of the 1D integration points ($\bar{\bar{\xi}}_g$) in the 3D isoparametric system using a standard Newton-Raphson alogrithm.

B.4 Reduced-order finite element discretization of geometrical nonlinearities

All the linear finite element matrices, that have been computed with the finite element method, are used for computing the reduced-order basis required for the construction of the mean nonlinear reduced-order model. The construction of the linear reduced-order matrices is straight forward and is written in Eqs. (2.77) to (2.80). However, the consideration of the geometrical nonlinearities of the structure, in the context of the reduced-order model, does not require the computational evaluation of the nonlinear finite element forces. In contrast, the nonlinear reduced-order model defined in Section 2.5 introduces the operator $\boldsymbol{\mathcal{F}}_{NL}(\mathbf{Q})$ of the nonlinear internal restoring forces. These nonlinear restoring forces are constructed using Eq. (2.81) in which the quadratic $\widehat{\mathcal{K}}^{(2)}_{\alpha\beta\gamma}$ and cubic $\mathcal{K}^{(3)}_{\alpha\beta\gamma\delta}$ operators are explicitly constructed using the methodology proposed in [78]. Such reduced-order finite element modelization of the geometrical nonlinearities allows for taking into account the uncertainties in the model by using the random matrix theory [99, 100, 37, 101]. The nonlinear operators are thus explicitly constructed using the 3D finite element methodology presented in Section B.1 and using the elastic projection basis $[\Phi_u]$ such that the elementary nodeal structural displacement $\mathbf{U}_E$ (in Eq. (B.10) can be expressed in term of generalized coordinates such that

$$\mathbf{U}_E = \sum_{\alpha=1}^{N_u} (\boldsymbol{\varphi}_u^{\alpha})_E \, Q_{\alpha}^u \quad , \tag{B.52}$$

where $(\boldsymbol{\varphi}_u^{\alpha})_E$ denotes the evaluation of the projection vector basis on the degrees of freedom related to element E. Let then introduce the $(3 \times 3n)$ real matrix $[C^{(k)}(\boldsymbol{\xi})]_{k\in\{1,2,3\}}$ defined by

$$[C^{(k)}(\boldsymbol{\xi})] = \begin{bmatrix} \dfrac{\partial N_1(\boldsymbol{\xi})}{\partial \xi_k} & 0 & 0 & \dots & \dfrac{\partial N_n(\boldsymbol{\xi})}{\partial \xi_k} & 0 & 0 \\ 0 & \dfrac{\partial N_1(\boldsymbol{\xi})}{\partial \xi_k} & 0 & \dots & 0 & \dfrac{\partial N_n(\boldsymbol{\xi})}{\partial \xi_k} & 0 \\ 0 & 0 & \dfrac{\partial N_1(\boldsymbol{\xi})}{\partial \xi_k} & \dots & 0 & 0 & \dfrac{\partial N_n(\boldsymbol{\xi})}{\partial \xi_k} \end{bmatrix} . \tag{B.53}$$

Let then introduce the $(6 \times 3n)$ matrix $[A^{(\beta)}(\boldsymbol{\xi})]$ which corresponds to the interpolation matrix related to the nonlinear part of the Green-Lagrange tensor using the Voigt notation defined as

$$[A^{(\beta)}(\boldsymbol{\xi})] = \begin{bmatrix} (\boldsymbol{\varphi}_u^{\beta})_E^T \, [C^{(1)}(\boldsymbol{\xi})]^T \, [C^{(1)}(\boldsymbol{\xi})] \\ (\boldsymbol{\varphi}_u^{\beta})_E^T \, [C^{(2)}(\boldsymbol{\xi})]^T \, [C^{(2)}(\boldsymbol{\xi})] \\ (\boldsymbol{\varphi}_u^{\beta})_E^T \, [C^{(3)}(\boldsymbol{\xi})]^T \, [C^{(3)}(\boldsymbol{\xi})] \\ (\boldsymbol{\varphi}_u^{\beta})_E^T \, \left([C^{(2)}(\boldsymbol{\xi})]^T \, [C^{(3)}(\boldsymbol{\xi})] + [C^{(3)}(\boldsymbol{\xi})]^T \, [C^{(2)}(\boldsymbol{\xi})] \right) \\ (\boldsymbol{\varphi}_u^{\beta})_E^T \, \left([C^{(1)}(\boldsymbol{\xi})]^T \, [C^{(3)}(\boldsymbol{\xi})] + [C^{(3)}(\boldsymbol{\xi})]^T \, [C^{(1)}(\boldsymbol{\xi})] \right) \\ (\boldsymbol{\varphi}_u^{\beta})_E^T \, \left([C^{(1)}(\boldsymbol{\xi})]^T \, [C^{(2)}(\boldsymbol{\xi})] + [C^{(2)}(\boldsymbol{\xi})]^T \, [C^{(1)}(\boldsymbol{\xi})] \right) \end{bmatrix} . \tag{B.54}$$

The discretization of the quadratic and cubic sitffness operators can thus be expressed as

$$\widehat{\mathcal{K}}^{(2)}_{\alpha\beta\gamma} = (\boldsymbol{\varphi}^{\alpha}_{u})^{T} \underset{i=1}{\overset{N_{E_u}}{\mathrm{A}}} \sum_{g=1}^{n_g} [\mathcal{B}(\boldsymbol{\xi}_g)]^{T} \, [C] \, [A^{(\beta)}(\boldsymbol{\xi}_g)] \, (\boldsymbol{\varphi}^{\gamma}_{u})_{E_i} \det\left([J(\boldsymbol{\xi}_g)]\right) \, \omega_g \quad , \tag{B.55}$$

$$\mathcal{K}^{(3)}_{\alpha\beta\gamma\delta} = (\boldsymbol{\varphi}^{\alpha}_{u})^{T} \underset{i=1}{\overset{N_{E_u}}{\mathrm{A}}} \sum_{g=1}^{n_g} [A^{(\beta)}(\boldsymbol{\xi}_g)]^{T} \, [C] \, [A^{(\gamma)}(\boldsymbol{\xi}_g)] \, (\boldsymbol{\varphi}^{\delta}_{u})_{E_i} \det\left([J(\boldsymbol{\xi}_g)]\right) \, \omega_g \quad . \tag{B.56}$$

Appendix C

Calculation of the principal curvature radii of a surface

The calculation of the principal curvature radii R_1 and R_2 of the free surface of the internal liquid is performed in a pre-calculation. The elementary principal curvature radii $R_1^{E_i}$ and $R_2^{E_i}$, used in the finite element discretization of matrix $[K_c^s]$ defined by Eq. (B.34), are calculated using a Matlab function find in the Mathworks library [93, 98]. This function allows for computing the mean, Gaussian, and principal curvatures of a given surface in a 3D space. The results are obviously function of the surface mesh fineness. Thus, some examples of 3D surface curvature calculations are presented in the following with respect to the characteristic mesh size d^{mesh} of the finite element surface. An example of a spherical surface of radius $R = 0.5\,m$ is presented in Figure C.1 with respect to the associated characteristic mesh sizes $d_1^{mesh} = 1\,m$, $d_2^{mesh} = 0.1\,m$, and $d_3^{mesh} = 0.05\,m$. In this spherical case, the two principal curvatures are identical and one can see that the influence of the mesh is negligible.

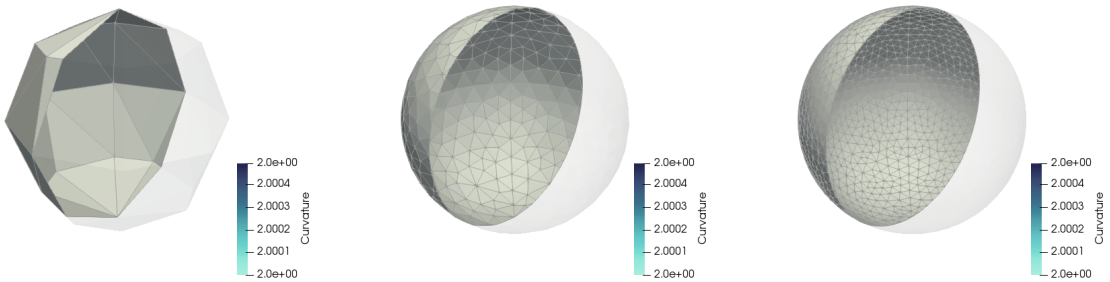

$d_1^{mesh} = 1\,m$ $d_2^{mesh} = 0.1\,m$ $d_3^{mesh} = 0.05\,m$

Figure C.1 – First and second principal cuvature radii of the spherical surface computed with respect to the mesh caracteristic sizes of the finite element surface.

However, for a more complex case presented in Figures C.2 and C.3, which respectively display the first and the second principal curvature radii of a surface presenting 3 different extrusion angles, we can see that the results strongly depend on the mesh caracteristic sizes $d_1^{mesh} = 1\,m$, $d_2^{mesh} = 0.1\,m$, and $d_3^{mesh} = 0.02\,m$. The calculations of the principal curvature radii of the free surface of the internal liquid for the various numerical applications presented in this manuscript have thus been performed by taking into account the influence of the finite element mesh size in order to ensure the good approximation of the curvatures of the surface.

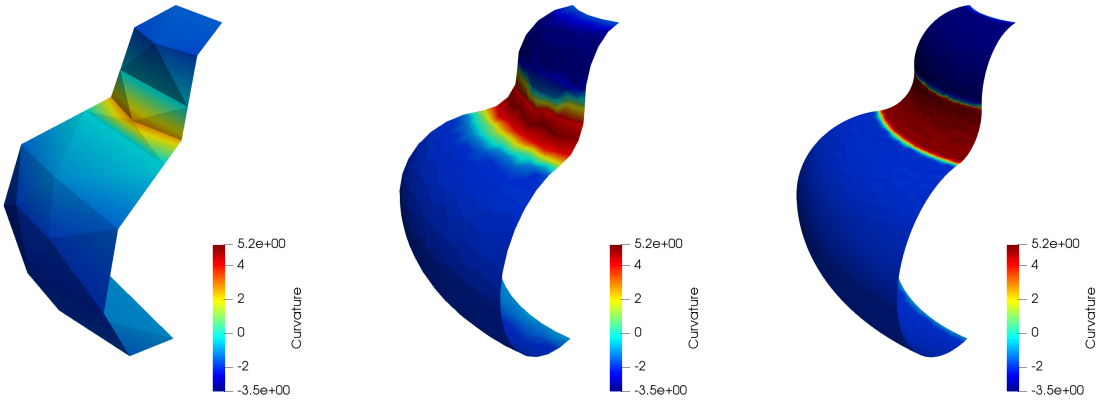

$d_1^{mesh} = 1\,m$ $d_2^{mesh} = 0.1\,m$ $d_3^{mesh} = 0.02\,m$

Figure C.2 – First principal cuvature radius of the "complex" surface computed with respect to the mesh caracteristic sizes of the finite element surface.

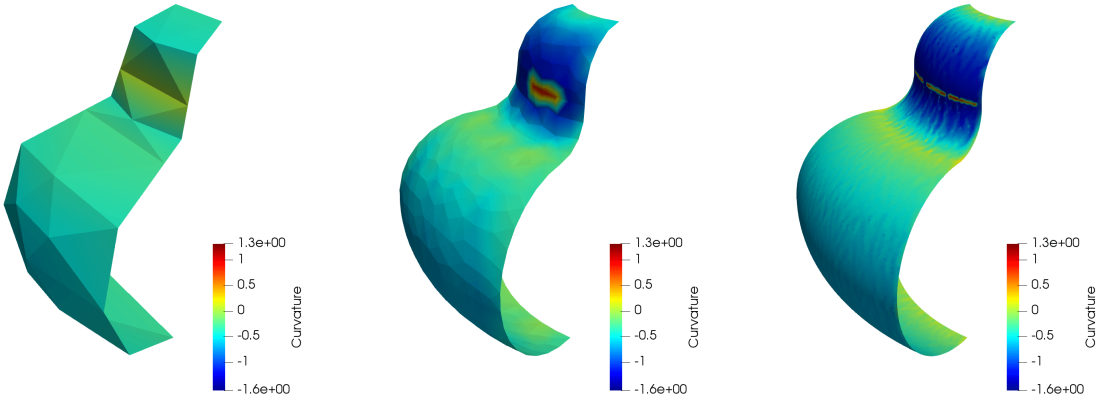

$d_1^{mesh} = 1\,m$ $d_2^{mesh} = 0.1\,m$ $d_3^{mesh} = 0.02\,m$

Figure C.3 – Second principal cuvature radius of the "complex" surface computed with respect to the mesh caracteristic sizes of the finite element surface.

Bibliography

[1] Orbital propulsion centre, lampoldshausen, germany. http://www.space-propulsion.com/index.html.

[2] H. N. Abramson. *The Dynamic Behavior of Liquids in Moving Containers, with Applications to Space Vehicle Technology*. NASA SP. Government Press, 1966.

[3] H. N. Abramson, D. D. Kana, and U. S. Lindholm. An experimental study of liquid instability in a vibrating elastic tank. *Journal of Spacecraft and Rockets*, 3(8):1183–1188, 1966.

[4] Q. Akkaoui, E. Capiez-Lernout, C. Soize, and R. Ohayon. Computational modeling of a coupled fluid-structure system with sloshing and capillarity. In *Actes du 23ème Congrès Français de Mécanique (CFM 2017)*, Lille, France, Aug 2017.

[5] Q. Akkaoui, E. Capiez-Lernout, C. Soize, and R. Ohayon. A computational strategy for solving large generalized eigenvalue problems in fluid-structure interactions. In *Proceedings of the 13th World Congress of Computational Mechanics (WCCM 2018)*, New York, United States, Jul 2018.

[6] Q. Akkaoui, E. Capiez-Lernout, C. Soize, and R. Ohayon. Geometrically nonlinear effects on a fluid-structure computational model with sloshing and capillarity. In *Proceedings of the 6th European Conference on Computational Mechanics (Solids, Structures and Coupled Problems) (ECCM 6)*, Glasgow, United Kingdom, Jun 2018.

[7] Q. Akkaoui, E. Capiez-Lernout, C. Soize, and R. Ohayon. Nonlinear dynamical analysis of a fluid-structure computational model with sloshing and capillarity. In *Proceedings of the 28th Conference on Noise and Vibration Engineering (ISMA 2018)*, pages 1–12, Leuven, Belgium, Sep 2018. KU Leuven.

[8] Q. Akkaoui, E. Capiez-Lernout, C. Soize, and R. Ohayon. Solving generalized eigenvalue problems for large scale fluid-structure computational models with mid-power computers. *Computers & Structures*, 205:45–54, 2018.

[9] Q. Akkaoui, E. Capiez-Lernout, C. Soize, and R. Ohayon. Analyse d'une expérimentation exhibant une instabilité dans un liquide avec un modèle réduit non linéaire fluide-structure. In *Actes du 14ème Colloque National en Calcul des Structures (CSMA 2019)*, pages 1–7, Giens (Var), France, May 2019.

[10] Q. Akkaoui, E. Capiez-Lernout, C. Soize, and R. Ohayon. Nonlinear dynamical analysis for coupled fluid-structure systems. In G. Kerschen, M. Brake, and L. Renson, editors, *Nonlinear Structures and Systems, Volume 1. Conference proceedings of the Society for Experimental Mechanics Series*, pages 151–153. Springer Cham, 2019.

[11] Q. Akkaoui, E. Capiez-Lernout, C. Soize, and R. Ohayon. Nonlinear reduced-order model of coupled fluid-structure system with sloshing and capillarity-revisiting and explaining an experiment. In *Proceedings of the 8th International Conference on Coupled Problems in Science and Engineering (COUPLED 2019)*, June 2019.

[12] Q. Akkaoui, E. Capiez-Lernout, C. Soize, and R. Ohayon. Revisiting the experiment of a free-surface resonance of a liquid in a vibration tank using a nonlinear fluid–structure computational model. *Journal of Fluids and Structures*, 85:149–164, 2019.

[13] Q. Akkaoui, E. Capiez-Lernout, C. Soize, and R. Ohayon. Uncertainty quantification in reduced-order model for vibrations of geometrical nonlinear structures coupled with acoustic fluids in presence of sloshing and capillarity. In *Proceedings of the 3rd International Conference on Uncertainty Quantification in Computational Sciences and Engineering (UNCECOMP2019)*, Island of Crete, Greece, Jun 2019.

[14] Q. Akkaoui, E. Capiez-Lernout, C. Soize, and R. Ohayon. Uncertainty quantification for dynamics of geometrically nonlinear structures coupled with internal acoustic fluids in presence of sloshing and capillarity. *Journal of Fluids and Structures*, submitted in october 2019.

[15] H. M. Aktulga, L. Lin, C. Haine, E. G. Ng, and C. Yang. Parallel eigenvalue calculation based on multiple shift–invert Lanczos and contour integral based spectral projection method. *Parallel Computing*, 40(7):195–212, 2014.

[16] F. Alijani and M. Amabili. Non-linear vibrations of shells: A literature review from 2003 to 2013. *International Journal of Non-Linear Mechanics*, 58:233–257, 2014.

[17] M. Amabili. *Nonlinear Vibrations and Stability of Shells and Plates*. Cambridge University Press, Cambridge, 2008.

[18] M. Amabili, R. Arziera, and A. Negri. Experimental study on large-amplitude vibrations of water-filled circular cylindrical shells. *Journal of Fluids and Structures*, 16(2):213–227, 2002.

[19] M. Amabili and M. P. Paıdoussis. Review of studies on geometrically nonlinear vibrations and dynamics of circular cylindrical shells and panels, with and without fluid-structure interaction. *Applied Mechanics Reviews*, 56(4):349–381, 2003.

[20] M. Amabili, A. Sarkar, and M. Paıdoussis. Reduced-order models for nonlinear vibrations of cylindrical shells via the proper orthogonal decomposition method. *Journal of Fluids and Structures*, 18(2):227–250, 2003.

[21] M. Amabili and C. Touzé. Reduced-order models for nonlinear vibrations of fluid-filled circular cylindrical shells: comparison of POD and asymptotic nonlinear normal modes methods. *Journal of Fluids and Structures*, 23(6):885–903, 2007.

[22] E. Anderson, Z. Bai, C. Bischof, S. Blackford, J. Demmel, J. Dongarra, J. Du Croz, A. Greenbaum, S. Hammarling, A. McKenney, and D. Sorensen. *LAPACK Users' Guide*. Society for Industrial and Applied Mathematics, Philadelphia, PA, third edition, 1999.

[23] Z. Bai, J. Demmel, J. Dongarra, A. Ruhe, and H. van der Vorst. *Templates for the solution of algebraic eigenvalue problems: a practical guide*. SIAM, 2000.

[24] F. Ballarin and G. Rozza. POD–galerkin monolithic reduced order models for parametrized fluid-structure interaction problems. *International Journal for Numerical Methods in Fluids*, 82(12):1010–1034, 2016.

[25] K. Bathe. *Finite Element Procedures*. Prentice Hall, 2006.

[26] K.-J. Bathe. The subspace iteration method–Revisited. *Computers & Structures*, 126:177–183, 2013.

[27] H. Bauer. Liquid sloshing in a cylindrical quarter tank. *AIAA Journal*, 1(11):2601–2606, 1963.

[28] T. Belytschko. Methods and programs for analysis of fluid-structure systems. *Nuclear Engineering and Design*, 42(1):41–52, 1977.

[29] T. Belytschko and W. K. Liu. Computer methods for transient fluid-structure analysis of nuclear reactors. *Nuclear Safety*, 26(1):14–31, 1985.

[30] H. Berger, J. Boujot, and R. Ohayon. On a spectral problem in vibration mechanics: computation of elastic tanks partially filled with liquids. *Journal of Mathematical Analysis and Applications*, 51(2):272–298, 1975.

[31] R. E. D. Bishop and W. Price. *Hydroelasticity of Ships*. Cambridge University Press, Cambridge, 1979.

[32] K. A. Brakke. The surface evolver. *Experimental mathematics*, 1(2):141–165, 1992.

[33] R. P. Brent and F. T. Luk. The solution of singular-value and symmetric eigenvalue problems on multiprocessor arrays. *SIAM Journal on Scientific and Statistical Computing*, 6(1):69–84, 1985.

[34] M. Bruneau, T. Scelo, and D. Socit Franaise. *Fundamentals of Acoustics*. Wiley Online Library, 2006.

[35] E. Capiez-Lernout and C. Soize. Design optimization with an uncertain vibroacoustic model. *Journal of Vibration and Acoustics*, 130(2):021001, 2008.

[36] E. Capiez-Lernout and C. Soize. An improvement of the uncertainty quantification in computational structural dynamics with nonlinear geometrical effects. *International Journal for Uncertainty Quantification*, 7(1), 2017.

[37] E. Capiez-Lernout, C. Soize, and M. Mignolet. Computational stochastic statics of an uncertain curved structure with geometrical nonlinearity in three-dimensional elasticity. *Computational Mechanics*, 49(1):87–97, 2012.

[38] S. Carra, M. Amabili, and R. Garziera. Experimental study of large amplitude vibrations of a thin plate in contact with sloshing liquids. *Journal of Fluids and Structures*, 42:88–111, 2013.

[39] F. Chatelin. *Eigenvalues of Matrices: Revised Edition*. SIAM, 2012.

[40] J. C. Chen and C. D. Babcock. Nonlinear vibration of cylindrical shells. *AIAA Journal*, 13(7):868–876, 1975.

[41] M. Chiba. Nonlinear hydroelastic vibration of a cylindrical tank with an elastic bottom, containing liquid. part I: Experiment. *Journal of Fluids and Structures*, 6(2):181–206, 1992.

[42] J. Choi, J. Demmel, I. Dhillon, J. Dongarra, S. Ostrouchov, A. Petitet, K. Stanley, D. Walker, and R. C. Whaley. ScaLAPACK: A portable linear algebra library for distributed memory computers. Design issues and performance. In *International Workshop on Applied Parallel Computing*, pages 95–106. Springer, 1995.

[43] W. Chu and D. D. Kana. A theory for nonlinear transverse vibrations of a partially filled elastic tank. *AIAA Journal*, 5(10):1828–1835, 1967.

[44] P. G. Ciarlet. The finite element method for elliptic problems. *Classics in Applied Mathematics*, 40:1–511, 2002.

[45] M. A. Crisfield, J. J. Remmers, C. V. Verhoosel, et al. *Nonlinear Finite Element Analysis of Solids and Structures*. John Wiley & Sons, New york, 2012.

[46] J.-F. Debongnie. On a purely lagrangian formulation of sloshing and fluid-induced vibrations of tanks. *Computer Methods in Applied Mechanics and Engineering*, 58(1):1–18, 1986.

[47] G. Deodatis and P. D. Spanos. 5th International Conference on Computational Stochastic Mechanics. *Special issue of the Probabilistic Engineering Mechanics*, 33(3):315–327, 2008.

[48] V. Dolean, P. Jolivet, and F. Nataf. *An Introduction to Domain Decomposition Methods: Algorithms, Theory, and Parallel Implementation*. SIAM, 2015.

[49] J. J. Dongarra and D. C. Sorensen. A fully parallel algorithm for the symmetric eigenvalue problem. *SIAM Journal on Scientific and Statistical Computing*, 8(2):s139–s154, 1987.

[50] J. J. Dongarra and D. W. Walker. Software libraries for linear algebra computations on high performance computers. *SIAM review*, 37(2):151–180, 1995.

[51] E. Dowell. Comments on the nonlinear vibrations of cylindrical shells. *Journal of Fluids and Structures*, 12:1087–1089, 1998.

[52] J.-F. Durand, C. Soize, and L. Gagliardini. Structural-acoustic modeling of automotive vehicles in presence of uncertainties and experimental identification and validation. *The Journal of the Acoustical Society of America*, 124(3):1513–1525, 2008.

[53] M. El-Kamali, J.-S. Schotté, and R. Ohayon. Computation of the equilibrium position of a liquid with surface tension inside a tank of complex geometry and extension to sloshing dynamic cases. *Computational Mechanics*, 46(1):169–184, 2010.

[54] M. El-Kamali, J.-S. Schotté, and R. Ohayon. Three-dimensional modal analysis of sloshing under surface tension. *International Journal for Numerical Methods in Fluids*, 65(1-3):87–105, 2011.

[55] R. Finn. On the equations of capillarity. *Journal of Mathematical Fluid Mechanics*, 3(2):139–151, 2001.

[56] R. Finn. The contact angle in capillarity. *Physics of Fluids*, 18(4):047102, 2006.

[57] R. Finn and G. K. Luli. On the capillary problem for compressible fluids. *Journal of Mathematical Fluid Mechanics*, 9(1):87–103, 2007.

[58] I. Flow Science. *FLOW-3D, Version 12.0.* Santa Fe, NM, 2019.

[59] R. G. Ghanem and P. D. Spanos. Spectral stochastic finite-element formulation for reliability analysis. *Journal of Engineering Mechanics*, 117(10):2351–2372, 1991.

[60] R. G. Ghanem and P. D. Spanos. *Stochastic Finite Elements: a Spectral Approach.* Springer-Verlag, Berlin, Heidelberg, 1991.

[61] G. H. Golub and C. F. Van Loan. *Matrix Computations.* SIAM, fourth edition, 2013.

[62] J. Gotze, S. Paul, and M. Sauer. An efficient Jacobi-like algorithm for parallel eigenvalue computation. *IEEE Transactions on Computers*, 42(9):1058–1065, 1993.

[63] V. Hernández, J. E. Román, and A. Tomás. Parallel Arnoldi eigensolvers with enhanced scalability via global communications rearrangement. *Parallel Computing*, 33(7):521–540, 2007.

[64] H. Imachi and T. Hoshi. Hybrid numerical solvers for massively parallel eigenvalue computations and their benchmark with electronic structure calculations. *Journal of Information Processing*, 24(1):164–172, 2016.

[65] I. C. Ipsen and Y. Saad. *The Impact of Parallel Architectures on the Solution of Eigenvalue Problems.* Yale University, Department of Computer Science, 1985.

[66] V. Kalantzis, J. Kestyn, E. Polizzi, and Y. Saad. Domain decomposition approaches for accelerating contour integration eigenvalue solvers for symmetric eigenvalue problems. *Preprint, Dept. Computer Science and Engineering, University of Minnesota*, 2016.

[67] T. Katagiri and Y. Kanada. An efficient implementation of parallel eigenvalue computation for massively parallel processing. *Parallel Computing*, 27(14):1831–1845, 2001.

[68] K. T. Kim and K. J. Bathe. The bathe subspace iteration method enriched by turning vectors. *Computers & Structures*, 186:11–21, 2017.

[69] P. Koval'chuk and V. Lakiza. Experimental study of induced oscillations with large deflections of fiberglass shells of revolution. *International Applied Mechanics*, 31(11):923–927, 1995.

[70] R. B. Lehoucq and D. C. Sorensen. Deflation techniques for an implicitly restarted Arnoldi iteration. *SIAM Journal on Matrix Analysis and Applications*, 17(4):789–821, 1996.

[71] A. W. Leissa. *Vibration of Shells.* Scientific and Technical Information Office, National Aeronautics and Space Administration, Washington, 1973.

[72] J. Lighthill. Acoustic streaming. *Journal of Sound and Vibration*, 61(3):391–418, 1978.

[73] U. S. Lindholm, D. D. Kana, and H. N. Abramson. Breathing vibrations of a circular cylindrical shell with an internal liquid. *Journal of the Aerospace Sciences*, 29(9):1052–1059, 1962.

[74] W. K. Liu and R. A. Uras. Variational approach to fluid-structure interaction with sloshing. *Nuclear Engineering and Design*, 106(1):69–85, 1988.

[75] B. R. Mace, K. Worden, and G. Manson. Uncertainty in structural dynamics. *Journal of Sound and Vibration*, 288(3):423–429, 2005.

[76] P. McIver. Sloshing frequencies for cylindrical and spherical containers filled to an arbitrary depth. *Journal of Fluid Mechanics*, 201:243–257, 1989.

[77] M. Mehta. *Random Matrices, Revised and Enlarged Second Edition.* Academic Press, New York, 1991.

[78] M. P. Mignolet and C. Soize. Stochastic reduced order models for uncertain geometrically nonlinear dynamical systems. *Computer Methods in Applied Mechanics and Engineering*, 197(45-48):3951–3963, 2008.

[79] T. Miras, J.-S. Schotté, and R. Ohayon. Energy approach for static and linearized dynamic studies of elastic structures containing incompressible liquids with capillarity: a theoretical formulation. *Computational Mechanics*, 50(6):729–741, 2012.

[80] N. N. Moiseyev and V. V. Rumiantsev. *Dynamic Stability of Bodies Containing Fluid.* Springer-Verlag, New York, 1968.

[81] H. J. Morand and R. Ohayon. *Fluid Structure Interaction.* John Wiley & Sons, New York, 1995 (French edition, Masson, Paris, 1992).

[82] R. Ohayon. Reduced models for fluid–structure interaction problems. *International Journal for Numerical Methods in Engineering*, 60(1):139–152, 2004.

[83] R. Ohayon and C. Soize. *Structural Acoustics and Vibration: Mechanical Models, Variational Formulations and Discretization.* Academic Press, San Diego, 1998.

[84] R. Ohayon and C. Soize. *Advanced Computational Vibroacoustics: Reduced-Order Models and Uncertainty Quantification.* Cambridge University Press, New York, 2014.

[85] R. Ohayon and C. Soize. Vibration of structures containing compressible liquids with surface tension and sloshing effects. Reduced-order model. *Computational Mechanics*, 55(6):1071–1078, 2015.

[86] R. Ohayon and C. Soize. Nonlinear model reduction for computational vibration analysis of structures with weak geometrical nonlinearity coupled with linear acoustic liquids in the presence of linear sloshing and capillarity. *Computers & Fluids*, 141:82 – 89, 2016.

[87] R. Ohayon, C. Soize, Q. Akkaoui, and E. Capiez-Lernout. Novel formulation for the effects of sloshing with capillarity on elastic structures in linear dynamics. *International Journal for Numerical Methods in Engineering*, submitted in 2019.

[88] B. N. Parlett. *The Symmetric Eigenvalue Problem.* SIAM, 1998.

[89] A. Pierce. *Acoustics: An Introduction to Its Physical Principles and Applications.* Acoustical Society of America, 1989.

[90] I. Rapoport and H. Abramson. *Dynamics of Elastic Containers Partially Filled with Liquid.* Applied Physics and Engineering. Springer-Verlag, Berlin and Heidelberg, 1968.

[91] P. J. Roache. Code verification by the method of manufactured solutions. *Journal of Fluids Engineering*, 124(1):4–10, 2002.

[92] D. Rodríguez and V. Theofilis. Massively parallel solution of the biglobal eigenvalue problem using dense linear algebra. *AIAA Journal*, 47(10):2449, 2009.

[93] S. Rusinkiewicz. Estimating curvatures and their derivatives on triangle meshes. In *Proceedings. 2nd International Symposium on 3D Data Processing, Visualization and Transmission, 2004. 3DPVT 2004*, pages 486–493. IEEE, 2004.

[94] Y. Saad. *Numerical Methods for Large Eigenvalue Problems: Revised Edition.* SIAM, 2011.

[95] J.-S. Schotté. *Influence de la Gravité sur les Vibrations Linéaires d'une structure Elastique Contenant un Liquide Incompressible.* PhD thesis, CNAM Paris, France, 2001.

[96] J.-S. Schotté and R. Ohayon. Linearized formulation for fluid-structure interaction: Application to the linear dynamic response of a pressurized elastic structure containing a fluid with a free surface. *Journal of Sound and Vibration*, 332(10):2396–2414, 2013.

[97] G. Schueller. On the treatment of uncertainties in structural mechanics and analysis. *Computers & structures*, 85(5-6):235–243, 2007.

[98] Y. B. Shabat and A. Fischer. Design of porous micro-structures using curvature analysis for additive-manufacturing. *Procedia CIRP*, 36:279–284, 2015.

[99] C. Soize. A nonparametric model of random uncertainties for reduced matrix models in structural dynamics. *Probabilistic Engineering Mechanics*, 15(3):277–294, 2000.

[100] C. Soize. Random matrix theory and non-parametric model of random uncertainties in vibration analysis. *Journal of Sound and Vibration*, 263(4):893–916, 2003.

[101] C. Soize. *Stochastic Models of Uncertainties in Computational Mechanics.* American Society of Civil Engineers Reston, 2012.

[102] C. Soize. *Uncertainty Quantification: An Accelerated Course with Advanced Applications in Computational Engineering.* Springer, New York, 2017.

[103] C. Soize and C. Farhat. A nonparametric probabilistic approach for quantifying uncertainties in low-dimensional and high-dimensional nonlinear models. *International Journal for Numerical Methods in Engineering*, 109(6):837–888, 2017.

[104] D. C. Sorensen. Implicit application of polynomial filters in ak-step Arnoldi method. *SIAM Journal on Matrix Analysis and Applications*, 13(1):357–385, 1992.

[105] I. M. Strand and O. M. Faltinsen. Linear sloshing in a 2d rectangular tank with a flexible sidewall. *Journal of Fluids and Structures*, 73:70–81, 2017.

[106] F. Tisseur and J. Dongarra. A parallel divide and conquer algorithm for the symmetric eigenvalue problem on distributed memory architectures. *SIAM Journal on Scientific Computing*, 20(6):2223–2236, 1999.

[107] P. Tong. *Liquid Sloshing in an Elastic Container.* PhD thesis, California Institute of Technology, 1966.

[108] R. Valid, R. Ohayon, and H. Berger. Le calcul des réservoirs élastiques partiellement remplis de liquides, pour la prévision de l'effet pogo. *Recherche Aérospatiale*, (6):367–379, 1974.

[109] R. Valid, R. Ohayon, and H. Berger. Le calcul des réservoirs élastiques partiellement remplis de liquides, pour la prévision de l'effet pogo. In *Actes du 23ème Congrès de la Fédération Internationale d'Astronautique*, Vienne, Octobre 1972.

[110] D. S. Watkins. QR-like algorithms for eigenvalue problems. *Journal of Computational and Applied Mathematics*, 123(1):67–83, 2000.

[111] P. Wriggers. *Nonlinear Finite Element Methods*. Springer-Verlag, Berlin, Heidelberg, 2008.

[112] K. Wu and H. Simon. A parallel Lanczos method for symmetric generalized eigenvalue problems. *Computing and Visualization in Science*, 2(1):37–46, 1999.

[113] O. C. Zienkiewicz and R. L. Taylor. *The Finite Element Method*. McGraw-hill, London, 1977.